**Dissertation**
**submitted to the**
**Combined Faculties for the Natural Sciences and for Mathematics**
**of the Ruperto-Carola University of Heidelberg, Germany**
**for the degree of**
**Doctor of Natural Sciences**

**presented by**

**Qurrat-ul-Ain Gulfam**

**born in Sargodha, Pakistan**

**Oral examination: February 7th, 2013**

# Creation, applications and detection of entanglement

# in

# quantum optical systems

**Referees:** PD Dr. Jörg Evers

Prof. Dr. Thomas Gasenzer

# Zusammenfassung

Die vorliegende Arbeit untersucht drei Anwendungen zum Zwecke des Studiums oder der Nutzung verschiedener Aspekte von Verschränkung. Im ersten Projekt wurde die Verschränkung zwischen zwei Atomen in einem Viel-Moden Resonator unter Berücksichtigung von Retardierungseffekten betrachtet. Unter Retardierung versteht man in diesem Zusammenhang die endlichen Zeit, die von einem Photon zur Propagation zwischen den Atomen und dem Hohlraumrand benötigt wird. Es stellt sich heraus, dass die Retardierungseffekte sowohl die atomaren Besetzungen, als auch die Dynamik der Verschränkung in hohem Maße beeinflussen. Das zweite Projekt ist eine Studie von verschränkten photonischen Zuständen mit dem Ziel, das (beugungslimitierte) Auflösungsvermögen zu erhöhen. Dazu simulierten wir optische Zentroid-Messungen mit verschiedenen Arten von nichtklassischen Zuständen, welche zu einer Verbesserung der räumlichen Auflösung führten. Durch diese numerischen Simulationen des Messsystems konnten wir die Nachweisparameter für eine mögliche experimentelle Umsetzung optimieren und untersuchten zudem Multi-Photonen-Absorption, die für Quanten-Lithographie benötigt wird. In unserem dritten Projekt nutzten wir das Streulicht von einem resonant-getriebenen, korrelierten System, um Informationen über das System selbst zu erhalten. Die vorgeschlagenen Techniken können dazu verwendet werden, um in bestimmten Richtungen $n$-Atom-Korrelationen in einem Experiment direkt durch Licht-Streuung mit signifikanter Zählrate zu messen. Darüber hinaus ist eine solche Erfassung von Korrelationen nicht auf eine bestimmte räumliche Anordnung der Atome beschränkt, sondern kann für allgemeine Geometrien verwendent werden.

# Abstract

In this work, three applications aimed at studying or exploiting various aspects of entanglement are considered. In the first project, the entanglement between two atoms inside a multi mode resonator is investigated in the presence of retardation. Retardation is associated with the finite time required by a photon to propagate between atoms and cavity boundaries. It is found that retardation affects the atomic populations as well as the entanglement dynamics to a large degree. The second project is a study of entangled states of light to obtain an enhanced resolution. We have simulated optical centroid measurements for spatial resolution enhancement with various types of non-classical input states. By numerically simulating the measurement scheme, we optimize the detection parameters for an experimental implementation and also study the multi photon absorption required for quantum lithography. The third project uses the scattered light from a resonantly driven correlated system to obtain information about the system. Techniques have been proposed using which in certain detection directions, $n$-atom correlations can be directly accessed in an experiment via light scattering with a significant count rate. Moreover, such detection of correlations is not limited to a particular spatial geometry of atoms but can be utilized for generalized geometries, too.

In connection with the work in this thesis, the following article was published.

- **Qurrat-ul-Ain Gulfam**, Zbigniew Ficek, and Jörg Evers
  *Effect of retardation on the dynamics of entanglement between atoms*
  Phys. Rev. A. **86**, 022325 (2012).

The following article has been submitted to the pre-print server and to Phys. Rev. A.

- **Qurrat-ul-Ain Gulfam** and Jörg Evers
  *Numerical optical centroid measurements*
  (`arXiv:1301.0774 [quant-ph]`)

The following articles will be submitted for publication.

- Luling Jin, **Qurrat-ul-Ain Gulfam**, Mihai Macovei and Jörg Evers
  *Direct detection of n-particle atomic correlations via light scattering*
- **Qurrat-ul-Ain Gulfam** and Jörg Evers
  *Detection of n-atom correlations via scattering in arbitrary geometries*

In order to be accepted by the department of Physics and Astronomy, University of Heidelberg as a doctoral student, a masters thesis had to be written. The following articles were published based on that pre-Ph. D. work.

- **Qurrat-ul-Ain Gulfam** and Jörg Evers
  *Measurement of distance and orientation of two atoms in arbitrary geometry*
  J. Phys. B: At. Mol. Opt. Phys. **43**, 045501 (2010).
  Figure selected for cover image of the journal
  (`http://iopscience.iop.org/0953-4075/43`)
- **Qurrat-ul-Ain Gulfam**, Rameez-ul-Islam, and Manzoor Ikram
  *Quantum teleportation of a high-dimensional entangled state*
  J. Phys. B: At. Mol. Opt. Phys. **41**, 165502 (2008).

# Contents

# Introduction

Entanglement is a purely quantum mechanical phenomenon. Two or more quantum systems are said to be entangled if their dynamics can be described only with reference to each other even if they are physically spatially separated. A change in the state of one of the entangled systems is instantly reflected in all others. Mathematically, a quantum system is said to be entangled if it cannot be factorized (is inseparable) into product states of its subsystems. Entanglement is associated with non-classical correlations among quantum systems and possesses no classical counterpart. The striking non-classical nature of entanglement reveals fundamental properties of quantum mechanics. The first criticism to quantum theory was discussed in the famous EPR paper by Albert Einstein, Boris Podolsky and Nathan Rosen in the context of an interpretation of the quantum theory [1], where by a paradox the authors argued that the description of a physical reality by a quantum mechanical wave function is incomplete. In essence, they recognized the strange predictions allowed by quantum mechanics, such as, instantaneous action at a distance. The approach was discussed, extended, and coined as 'entanglement' by Erwin Schrödinger using the famous Schrödinger's cat thought experiments in 1935 and 1936 [2,3]. He wrote, "the best possible knowledge of a whole does not necessarily include the best possible knowledge of all its *parts*, even though they may be entirely separate and therefore virtually capable of being 'best possibly known,' …". He supposed that with a separation of the entangled particles, entanglement vanished spontaneously.

Because of the paradoxical nature of the idea, the concept of entanglement was paid no heed to for a long period of next thirty years. In 1964, John S. Bell re-investigated the EPR puzzle using simpler systems. In [4], (now known as Bell's inequality) he accepted the idea of local realism adopted by EPR. Then, he gave a straight forward but groundbreaking mathematical proof showing that no theory of local hidden variables can account for all of the predictions of quantum mechanics. Bell's inequalities are shown to be violated in quantum physical systems experimentally for the first time in 1972 by [5] and later by [6–10], thus proving that some idea at the heart of local hidden variables theories has to be false. The property which usually falsifies is locality - the idea that no physical effects move faster than the speed of light. This debate continued and finally led Alain Aspect [11, 12] and many others to experimentally show that entanglement can survive over longer distances. Thus, Schrödinger's supposition was proven false.

It was only in the 1980s that the non-local correlations among the entangled quantum systems started to be made use of by the theorists and experimentalists in the fields of physics, computer science, mathematics and cryptography as a new type of a physical resource. Despite being one of the most counter intuitive features of the quantum theory, entanglement has been studied enormously due to its inevitability in a wide range of applications of quantum mechanics, for example, quantum teleportation, quantum information, quantum cryptography and many more. Quantum teleportation is a method of secure transfer of an unknown quantum state accomplished using quantum entanglement and classical communication from one particle to another distant particle, without sending the particle itself [13, 14]. Quantum information is a study of storing (and retrieving) information using a quantum mechanical system. A qubit (quantum bit, the primary unit of information) can have not only states 0 and 1, like a classical bit but also a superposition of the two values [15]. Unlike traditional cryptography, quantum cryptography exploits entanglement and is theoretically unbeatable essentially because of the impossibility to measure the quantum state of a system without disturbing the system [16, 17].

It goes without saying that in order to benefit from all the interesting applications, quantum entanglement first needs to be created. There are numerous ways to create entanglement. Particles can become entangled due to direct interactions among them and it is also possible to produce quantum entanglement among identical particles that never directly interacted. Both methods have been studied intensively during the past few decades.

The indirect interaction that results in the creation of entanglement between particles is mediated via fields. Every particle interacts with the common field that surrounds all the particles. In particular small ensembles of few particles that can be described by a few energy states – the ground state and a few excited states are considered. The few-level approximation is valid as long as it is assumed that the field interacts resonantly or near-resonantly with these levels such that all other energy states are strongly detuned and therefore, do not participate in the interaction.

In terms of quantum mechanics, the field couples the different states of matter. Vacuum is defined as the ground state of the field, that is, when no excitation quanta are present in the field. According to the uncertainty principle, the vacuum is not "empty" and contains zero-point energy [18]. Two quantum systems can exchange energy by interaction with the vacuum and thus, can become entangled. An initially excited atom can become de-excited by emitting spontaneously a virtual photon. This virtual photon can be absorbed by an identical near-by atom and consequently, this neighboring atom becomes excited. In free space, the pre-requisite for such a vacuum induced interaction to take place is that the inter atomic separation is on the order of the atomic transition wavelength [19, 20]. Therefore, the photon exchange due to the so-called dipole dipole interaction is short-ranged. A similar interaction can be visualized inside a closed environment provided by a cavity when a system of atoms is placed inside it. Now, the atoms can experience a coupling due to the vacuum induced interaction within the resonator environment, even if they are positioned significantly far apart from each other [21]. This way, a long-ranged entanglement can be engineered through an exchange of energy between the atoms and the cavity field. Some theoretical studies of the method include [22–24], while an experiment is reported in [25].

Cavity quantum electrodynamics (QED) [26], the quantum mechanical interaction between a field confined within a cavity and atoms is a topic of active current research and has been studied extensively. The mathematical model that describes the simplest case of the interaction of a bosonic degree of freedom, a single mode of electromagnetic radiation and an effective two-level atom is known as the Jaynes-Cummings model [27]. The calculations of interaction with a quantized single mode field in both semi-classical and quantum pictures can be found in many quantum optics text books [28, 29]. The general case of several many-level atoms and many modes requires more effort.

Despite the rapid advancements on theoretical grounds, experimental verifications of the model, nevertheless, began quite late not only due of the lack of the techniques to manufacture high-finesse cavities but also mainly because trapping single atoms in the cavities for long enough times was extremely challenging since only beams of atoms were available. The first experiment for the laboratory observation of the collapse and revivals predicted in the atomic population inversion by the idealized example [27] was reported in 1987 [30]. This experiment at the Max Planck Institute for Quantum Optics involved thermal field cavity. Later, in 1996, Serge Haroche's group at Ecole Normale Supérieure, performed a much improved experiment with quantized coherent fields [31]. Due to his pioneering efforts in the field to measure and manipulate single atoms, S. Haroche won this year's Nobel prize in physics [32]. Nowadays, cavity QED is possible even with single atoms in optical transitions [33, 34]. This progress, on one hand, opens up new horizons for the construction of a quantum network, which aims at performing quantum computation. On the other hand, elementary verifications of quantum mechanics can be carried out.

The Jaynes-Cummings model, however, does not take into account the coupling of the atom-cavity system and the environment. Since no losses due to spontaneous emission of the atom into external cavity modes, characterized by the natural decay rate $\Gamma$ and the cavity decay rate $\kappa$, which is the leakage of the radiation to the environment outside the cavity are considered for the calculation, a time dependent Schrödinger's equation is used to obtain the equations of motion for the probability amplitudes. The decay channels can be included if the master equation approach to describe the equations of motion of the density matrix is used [35]. It allows the formation of mixed quantum states which is not possible in the plain Schrödinger's theory. The coupling between the atoms and the cavity, described by the coupling constant $g$ can be strong or weak depending on the values of $\Gamma$ and $\kappa$. If $\{\Gamma, \kappa\} \gg g$, no coherent evolution of the system is to be expected. This is called the weak coupling regime. On the other hand, the strong coupling condition, $\{\Gamma, \kappa\} \ll g$ allows the system to evolve coherently for relatively much longer time until ultimately dephasing occurs.

Generation of quantum entanglement by direct interaction between the particles has also been studied in great detail [14, 17, 36–39]. A typical method which provides a reliable source of strong entanglement is spontaneous parametric down-conversion (SPDC). It was experimentally demonstrated for the first time in 1970 [40]. Light from a coherent source, termed as the *pump* beam with frequency $\omega_p$ and momentum $\vec{k}_p$ enters a non-linear medium, for example, a photonic crystal. The crystal splits the incoming light into two beams of frequency different from $\omega_p$. The low energy correlated twins from the output beams are usually referred to as the *signal* and the *idler* beams having frequencies $\omega_s$ and $\omega_i$, and momenta $\vec{k}_s$ and $\vec{k}_i$, where $|\vec{k}_s| = |\vec{k}_i|$, $\omega_s = \omega_i = \omega_p/2$, respectively. Since under phase-matched conditions, the process of SPDC does not exchange energy with the non-linear crystal, according to the conservation of energy and momentum $\omega_p = \omega_s + \omega_i$ and $\vec{k}_p = \vec{k}_s + \vec{k}_i$, respectively. A simple interaction picture Hamiltonian of the process can be written as $H = \chi^{(2)} a_s^\dagger a_i^\dagger a_p +$h.c., where $\chi^{(2)}$ represents the second order non-linearity, $a_{s(i)}^\dagger$ denotes the creation operator corresponding to the signal (idler) photon, $a_p$ is the creation operator for the pump photon, respectively and h.c. stands for hermitian conjugate. The signal and idler beams can be of the same or perpendicular polarization with respect to each other. These set ups are called type I and type II SPDC, respectively. For the former, entanglement does not occur naturally, however, still there are experimental techniques by which it can be produced [41]. If the polarization of the two is perpendicular to each other, an entanglement between the polarizations of the output photons is created naturally. High intensity SPDC sources configured for generation of polarization-entangled photon pairs have been reported, for example, in [7, 42].

The polarization of the photons is not the only observable that allows for entanglement. Several recent experimental set ups show that SPDC sources can also be configured to create entanglement with respect to position and momentum (spatial entanglement) [43] or energy and time (time entanglement) [44] or path and number (momentum) [45].

The simplest and most famous example of a maximally momentum-entangled source of light is a two photon NOON state [45–47] created by the Hong-Ou-Mandel effect [48], which works as follows. Consider a 50:50 beam splitter. If identical single photons enter from each port of the beam splitter, both photons can exit only from the same output port. Because of the destructive interference of the amplitudes of two of the output probabilities where a single photon exits from each output port, there is no possibility of a coincidence detection. Such non-classical sources of light play an extremely vital role in studying macroscopic quantum interference [49, 50]. These states are helpful for performing high precision phase measurements which are integral parts of modern quantum metrology [51, 52] and have also been proposed for the use in quantum optical lithography and interferometry [45, 53]. By entangling $N$ photons in the incident beam, an effective $N$ times reduced wavelength and hence, a resolution enhancement by factor of $N$ can be achieved [54]. The mechanism of resolution enhancement by using non-classical features of the probing light is going to be studied in a great detail in this thesis.

Having listed a few out of many ways to generate and use quantum entanglement, we turn towards the detection and measurement of the entanglement. Being a phenomenon of great practical importance, a lot of research has been carried out on this topic. Many methods have been proposed and are being widely used to verify the presence of entanglement. The procedures, however, are limited to two or three qubit systems. Specifically, for entangled systems consisting of more than two particles, the methods to characterize the entanglement, at present, are very limited.

The physical approach to detect entanglement treats the quantum states of the particles as states belonging to a physical system. These physical states are experimentally produced either in the laboratory or they exist in nature [55–57], for example, Bell inequalities, entanglement witnesses, concurrence and so on. Schemes are developed which help access the correlations between the particles directly in an experiment. Here, one tries to identify the properties of a correlated system that can be relevant for the correlation detection. If entanglement is detected in the laboratory, it can help realize experiments, for example, based on quantum information processing.

In one part of the thesis, we have used concurrence [56, 57] as a measure of entanglement. Experiments to detect entanglement via concurrence include [58, 59]. In another part of the thesis, the count rates for coincidence detection have been estimated using a novel technique for directly detecting the correlations via fluorescent light.

This doctoral thesis is aimed at a deep investigation, thorough understanding and a detailed discussion of quantum entanglement, its applications and detection. While the underlying mechanism for the entire content is quantum entanglement and collective effects in interacting systems, the thesis has not been conceived to be read in a continuous manner. (Except Chapter 4, which is an extension of Chapter 3,) Every chapter in itself can be read and understood as a distinct unit since the necessary background, mathematical formalism, model system, results, conclusions and outlook have been presented separately.

In **Chapter (1)**, a system of a one-dimensional ring cavity assumed initially to be in a vacuum state, containing two identical two-level atoms at fixed positions in the strong coupling regime has been modeled [60]. The dynamics of entanglement between the two atoms caused by the interaction with the common electromagnetic field present in the vicinity has been studied in the presence of retardation. The effect of retardation is related to the finite time that is required by a photon to travel between the atoms and the boundaries of the cavity. The non-Markovian set up considered paves the path for an interference between the spontaneously emitted light and the radiation that has been reflected off by the cavity mirror. Here, we have used concurrence for the quantification of quantum entanglement between the atoms. In the very strong coupling regime, we have observed clear signatures of retardation in the time evolution of concurrence. Our studies include the analysis for various initial conditions of the atoms as well as the cavity. By varying the number of effective cavity field modes to which the atoms couple, we could switch between the domains of strong and negligible retardation. Through changes of inter atomic separations, we discovered that retardation effects are important not only at large inter atomic distances but also at sub-wavelength separations. We considered both short time dynamics of concurrence as well as long-time temporal evolution on both large as well as vanishing inter atomic separation scales. At short time scales designated by a few round trips of the photon inside the cavity, vivid and sudden changes in the concurrence due to retardation are attributed to a transfer of the population from the atoms to the symmetric Dicke state. The long time evolution shows periodic oscillations which have an overall beat-like envelop that can be described using the collapses and revivals in Jaynes-Cummings model. Furthermore, we studied the sudden birth, sudden death and resurrection of quantum entanglement in the presence of retardation.

Conventional schemes of optical lithography are limited in resolution by the Rayleigh diffraction limit given by $\lambda/2$, where $\lambda$ is the wavelength of the impinging light. In **Chapter (2)**, a resolution enhancement scheme based on the optical centroid method [54] has been studied. This scheme makes use of light sources having non-classical correlations. An ensemble of $N$ entangled photons having an effective wavelength of $\lambda/N$, provides with a resolution $\lambda/(2N)$. This much shorter wavelength can be used to beat the usual diffraction limit by a factor of $N$ and hence enhance the resolution $N$ times in optical imaging schemes. Nevertheless, the detection of such highly energetic multi photon states is a stringent experimental limitation due to either the unavailability or the high cost of good multi photon resists. On the other hand, the optical centroid method for resolution enhancement requires a detection system consisting of arrays of single photo detectors. The measurement proposal that does not demand a multi photon absorption is shown to be fundamentally more efficient than any quantum lithography scheme. The first proof-of-principle experiment with two photon NOON states has been reported in [61]. The experimentalists performed both quantum lithography and optical centroid measurements with two photon NOON states and showed that although the same resolution enhancement was achieved with the two measurement procedures, as predicted, the optical centroid method was to be preferred due to its higher efficiency. We have inspected the mentioned scheme numerically by extracting events randomly from the incident wave function and later post processing them. This way, we could optimize the detection parameters for an experimental implementation. We have examined the scheme with the non-classical states of light mentioned in [54], that is, NOON states and jointly Gaussian states [62] and also explored other new kind of input states, that is, correlated Schrödinger's cat states [34,63, 64], that can also be exploited for resolution enhancement with the current method. For all of the incident non-classical states, we could recover the centroid probability distribution with different number of photons to verify the resolution enhancement with an increase in the number of photons. We have also performed multi photon absorption analysis with different states in different ways.

**Chapter (3)** is founded on the direct detection of atomic correlations through light scattered off a few-particle ensemble. A small ensemble of atoms is correlated via the dipole dipole interaction or Rydberg-Rydberg interaction(RRI) [65]. A Rydberg atom is a large-sized (large principle quantum number $n$), long-lived atom with huge electric dipole moment. A non-negligible dipole dipole interaction takes place between atoms excited to Rydberg states if their product Rydberg states are nearly degenerate. The RRI can be Förster Resonance (scales like $\sim r^{-3}$) or classical van-der-Waals interaction (scales like $\sim r^{-6}$) for inter atomic distance $r$, depending upon the strength of the interaction and the energy difference between the pair states. RRI has in fact the longest range (scales as $n^{11}$) that has been observed among neutral atoms. Therefore, in a gas of cold Rydberg atoms, an atom is bound not only to interact with its nearest neighbors but many-body interactions [66] take place and interesting effects like dipole blockade occur [67,68]. In [69], a correlated atomic ensemble which is in the form of a linear chain is considered. The sample is driven weakly by resonant lasers incident perpendicularly and the fluorescent signal is recorded as a function of detection angles. A coincidence detection apparatus is used to record the second order correlation function. A decomposition of the second order correlation function allows to distinguish the correlations among different numbers of atoms out of the ensemble. These correlations among the different atoms can be experimentally accessed through coincidence detection in certain directions of the detectors. We have extended the work of [69] to determine the efficiency of the scheme. We discovered that despite the weak interactions among the atoms, a coincidence signal of significant size can be attained. Thus low count rate is not going to cause a problem for the experimental realization of the scheme. Moreover, we analyzed the situation for different number of atoms in the chain and discovered that not only the interesting detection directions still pointed out to correlations among different atoms but also in many cases, the signal size increased with the number of scatterers.

As an extension of this work, in **Chapter (4)**, we consider ensembles of Rydberg atoms in more generalized geometries. Here, we do not confine the atoms to be at equidistant positions in a line but allow them to be in various position configurations in a line or a plane which is perpendicular to the incoming laser field. Interesting results have been obtained as a result of more general orientations and distances. In particular, we discovered and explained the counter-intuitive fact that in certain geometries as the inter atomic distance is increased, 3-particle correlations vanish even before the elimination of 4-particle correlations. Separating the atoms further eventually makes 4-atom correlations disappear too such that only 2-atom correlations survive. Ultimately, at large distances, all the atoms become uncorrelated. We have explained this result using two independent approaches. There is still room for promising ideas that can be pursued with RRI atoms in arbitrary geometries with respect to the incident resonant laser fields.

Finally, the main results presented in the thesis are summarized in the last section.

# Chapter 1

# Effect of retardation on the dynamics of entanglement between atoms

The main results of this chapter have been published in the paper [60]:
**Q. Gulfam**, Z. Ficek, and J. Evers
*Effect of retardation on the dynamics of entanglement between atoms*
Phys. Rev. A **86**, 022325 (2012).

*The role of retardation in the entanglement dynamics of two distant atoms interacting with a multi-mode field of a ring cavity is discussed. The retardation is associated with a finite time required for light to travel between the atoms located at a finite distance and between the atoms and the cavity boundaries. We explore features in the concurrence indicative of retardation and show how these features evolve depending on the initial state of the system, distance between the atoms and the number of modes to which the atoms are coupled. In particular, we consider the short-time and the long time dynamics for both the multi- and sub-wavelength distances between the atoms. It is found that the retardation effects can qualitatively modify the entanglement dynamics of the atoms not only at multi- but also at sub-wavelength distances. We follow the temporal evolution of the concurrence and find that at short times of the evolution the retardation induces periodic sudden changes of entanglement. To analyze where the entanglement lies in the space spanned by the state vectors of the system, we introduce the collective Dicke states of the atomic system that explicitly account for the sudden changes as a periodic excitation of the atomic system to the maximally entangled symmetric state. At long times, the retardation gives rise to periodic beats in the concurrence that resemble the phenomenon of collapses and revivals in the Jaynes-Cummings model. In addition, we identify parameter values and initial conditions at which the atoms remain separable or are entangled without retardation during the entire evolution time, but exhibit the phenomena of sudden birth and sudden death of entanglement when the retardation is included.*

## 1.1 Introduction

Entanglement is one of the most familiar phenomena resulting from the presence of non classical correlations between quantum systems [70, 71]. A large number of studies have demonstrated that entanglement can be created in variety of systems ranging from simple systems such as single photons or atoms to more complex systems such as spin chains or biological samples. The presence of an entanglement between systems has been tested experimentally in various optical experiments. For example, slowly moving atoms can be entangled while passing through a cavity [72,73], and the entanglement between the atoms can be detected by probing the atomic state of the atoms after leaving the cavity [34, 74]. Another common setup is the entanglement of photons obtained from a down-conversion process. In [75], an experimental study of polarization entanglement is performed. The entanglement is found to be dependent on not only the bandwidth of the spectral filters but also on the length of the down-conversion crystal. [76] also is an experimental verification of the theory of spontaneous parametric down conversion (SPDC). Here, in spatially separated bulk crystals, the interference effects are discovered to be generated from SPDC. An experimental evidence of the creation of short wavelength, ultraviolet entangled photon pairs has been provided in [77]. The method is based on third order non-linear process in a semiconductor for producing a pair of entangled photon. [78] uses micro-ring resonator structures for the enhancement of a SPDC process. SPDC at telecommunication wavelength is performed in a simple but deterministic manner in [79]. By fabricating a special crystal, highly entangled photons at two different wavelengths are created. In all these cases, the entanglement between the photons can be verified, for example, by detecting correlations between their polarizations [80, 81].

Apart from the issue of creating entanglement, also a detailed analysis of the dynamics of an entangled system is of importance. One motivation for this is the possibility for transferring entanglement between distant quantum systems [82]. Such transfers have become especially interesting since a number of experiments have succeeded in the creation of quantum gates necessary for the implementation of quantum networks [83]. However, if one examines the dynamics of an entangled system coupled to a network of quantum systems, it becomes apparent that the unavoidable coupling of the systems to the external environment can lead to the irreversible loss of the transferred entanglement. In this connection, one would expect that the coupling of the systems to local environments, with a Markovian assumption of the process, could lead to an exponential decay of the entanglement from its initial value. However, there are some entangled states, particularly those involving at least two excitations, that may decay in an essentially non-exponential manner resulting in the disappearance of the entanglement in a finite time. This effect, known as sudden death of entanglement (SDE), has been studied in a numerous number of papers [71, 84–88], and has recently been observed in experiments involving photons [89, 90] and atoms [91]. Furthermore, theoretical treatment of the coupling of sub-systems to a common (non-local) environment has predicted that the already destroyed entanglement could suddenly revive or initially separable systems could become entangled after a finite time, the phenomenon known as sudden birth of entanglement (SBE). [92] is a study of entanglement that is induced by spontaneous emission in two non-overlapping atoms.

The cases of identical as well as non-identical atoms are considered. In [93], again SBE dependent on collective damping is investigated. Here, two initially entangled qubits are coupled collectively to a multimode vacuum. [94] is a description of time-delayed SBE caused by spontaneous emission. The threshold time for SBE is also determined. Entanglement of two cavities coupled to two independent reservoirs has been accounted for in [95]. The disappearance of cavity entanglement results necessarily in reservoir entanglement. Finally, entanglement of qubits in a common structured Lorentzian reservoir has been discussed in [96]. The revivals of entanglement occur due to the back-action of the non-Markovian reservoir.

From experimental point of view, in particular the study of the generation of entanglement in systems confined within optical or microwave cavities [26,34,74,97,98] is of importance. Cavities provide a well-defined mode spectrum and a relatively loss-free environment such that the atom-field interactions can have anomalously large coupling strengths, leading to reversible, non-Markovian type dynamics of the system. As a consequence, the already dead entanglement can revive even if in the equivalent free-space situation no revival is predicted [84,85,96,99–105]. However, calculations based on deriving the master equation for the reduced density operator of two atoms, both placed inside a cavity, frequently assume a large distance between the atoms such that there is no direct interaction between them. At the same moment the treatments assume that each atom influences the other instantaneously. For this, there is no time delay or equivalently no phase difference between the oscillating atomic dipole moments resulting in an effective coupling between the atoms independent of their distance. It turns out that these non-retarded models to physical systems are suitable if the atoms interact with a single cavity mode. A more interesting parameter regime arises if the atom couples to a large number of cavity modes. In this case, retardation effects become important [21, 106–108]. These effects are associated with a finite time required for light to travel, e.g., from the atom to the boundary of the cavity and back to the atom after being reflected from the cavity mirror. This leads to the interference between instantaneously emitted photon and the retarded waves that are reflected from the cavity walls.

In an early study Milonni and Knight [106, 107] discussed the effect of the retardation on the collective behavior of two atoms. They demonstrated that that retardation effects in the interaction between two atoms in free space become important for distances larger than the half-wavelength of the field. Recent studies of the interaction of atoms with multi-mode cavities have predicted strong non-Markovian and retardation effects in the population dynamics [21, 108]. The multi-mode cavity field can be treated as a small environment to the atoms [109]. This leads to a spatial modulation of the field amplitude which significantly alters the nature of the interaction between the atoms and the field.

While most of the studies on SDE and SBE assumed the Markovian approximation such that a backaction of the environment on the atoms is effectively excluded, recently, however, also the non-Markovian case has received considerable attention [84, 85, 96, 99–105]. In particular those explicitly taking into account the distance between the particles are of relevance [110–112]. In these works it was shown that for certain initial states, the distance between the qubits can qualitatively change the entanglement dynamics. For example, depending on the distance, SDE and SBE can occur or not. However, these works made use of a continuum of environmental modes by integrating over all wave vectors $\vec{k}$. This raises the question about the entanglement dynamics of atoms in multi-mode cavities with a set of discrete field modes, which are known to exhibit strong non-Markovian and retardation effects in the population dynamics [21].

In this chapter, we investigate the effect of retardation on the generation and dynamics of entanglement between two two-level atoms located inside a ring cavity while constraint the number of excitations in the system first to one and then to two. The model studied requires that we develop a multi-mode theory of the interaction of the atoms with the cavity field so the effects of propagation are fully incorporated in our analysis of the time evolution of the entanglement measure, concurrence [56, 57]. The goal then is to trace the time evolution of the concurrence in the case of single or double excitations present in the system. We show that the quantum nature of the cavity field crucially affects the generation of entanglement in the system. There is no SDE/SBE when we do not allow for a double excitation in our system. The absence of SDE for single-excitation inside a lossy cavity has been shown by [113]. In the course of the calculation we observe that the retardation effects do play a significant role in the creation of entanglement between the atoms in the double excitation case. Certain transient effects such as abrupt kinks in the time evolution of the populations and the concurrence occur. The kinks reflect the effects of multiple photon exchange between the atoms and appear at intervals corresponding to the multiplets of time required for the photon to travel between the atoms or to take the round trip in the cavity. The effect of the retardation on the phenomena of sudden death, revival and sudden birth of entanglement is also discussed.

In particular, we identify parameters and initial conditions, in which the atoms remain separable without retardation throughout the entire evolution time, but exhibit sudden birth and death of entanglement with retardation, and vice versa. Both, the short-time and the long time dynamics are analyzed, and we also study time-averaged concurrences. Lastly, we show that the exact placement of the atom within a wavelength is very important. We also study the distance dependence on two scales: First, in integer multiples of the wavelength, corresponding to different positions in a periodic potential, and second on a sub-wavelength scale.

We begin in Sec. 1.2 by introducing the model comprising of the atoms and the ring cavity and derive the equations of motion for the probability amplitudes in two cases of single and double excitations present in the system. These equations are obtained by considering a multi-mode rather than a single-mode interaction of the atoms with the electromagnetic cavity field assumed initially to be in the vacuum state. Then, in Sec. 1.3.3 we apply the solutions for the probability amplitudes to the problem of the time evolution of the populations and the concurrence. Throughout, we assume that the atoms interact with a finite number of the cavity modes. The numerical results for various special cases of the time evolution of the populations and the concurrence are illustrated in Sec. 1.4. We also present there the qualitative discussion of the short and long time behaviors as well as the average behavior of the concurrence. Finally, in Sec. 1.6 we briefly summarize our results. A succint outlook follows in Sec. 1.7.

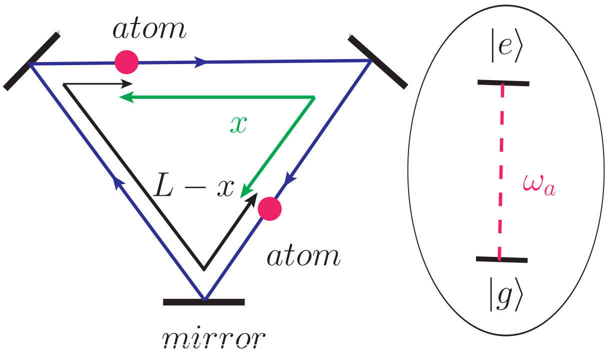

Figure 1.1: (Color online) Schematic diagram of the system considered. Two identical two-level atoms are at fixed positions, distant $x$ from each other, located inside a one-dimensional ring cavity of the round trip path $L$. The internal structure of each atom is shown in the right inset. The atoms are modeled as two-level systems with the excited $|e_i\rangle$ and ground $|g_i\rangle$ states separated by the transition frequency $\omega_a$.

## 1.2 The model

We consider two identical atoms, located inside a ring cavity at fixed positions $\vec{x}_1$ and $\vec{x}_2$, with distance $|\vec{x}_2 - \vec{x}_1| = x$. The atoms are modeled as two-level systems with excited state $|e_i\rangle$ and ground state $|g_i\rangle$ ($i \in \{1,2\}$) separated by energy $\hbar\omega_a$, as shown in Fig. 1.1.

The cavity is considered as a multi-mode cavity with frequency difference between adjacent modes (free spectral range) such that multiple modes are supported within the atomic resonance line width. The consideration of several rather than a single mode in the interaction of the atoms with the cavity field will be found crucial for the occurrence of retardation in the radiative coupling between the atoms.

### 1.2.1 Hamiltonian of the system

The Hamiltonian of the atoms interacting with the common electromagnetic field of the ring cavity can be written as [21]

$$H = H_a + H_f + H_{af}, \tag{1.1}$$

where

$$H_a = \sum_{j=1}^{2} \hbar\omega_a S_j^+ S_j^- \tag{1.2}$$

is the free Hamiltonian of the atoms,

$$H_f = \hbar \sum_{\mu} \omega_n a_\mu^\dagger a_\mu \tag{1.3}$$

is the free Hamiltonian of the cavity field, and

$$H_{af} = -\vec{D}_1 \cdot \vec{E}(\vec{x}_1) - \vec{D}_2 \cdot \vec{E}(\vec{x}_2) \tag{1.4}$$

is the interaction between the atoms and the cavity field, written in the electric dipole approximation.

In the Hamiltonian Eq. (1.1), the atoms are represented by the transition dipole moment operators

$$\vec{D}_j = \vec{d}_j S_j^+ + \vec{d}_j^* S_j^-, \tag{1.5}$$

where $S_j^+ = |e_j\rangle\langle g_j|$ and $S_j^- = |g_j\rangle\langle e_j|$ are respectively the dipole raising and lowering operators of the atom $j$, and $\vec{d}_j = \langle g_j|\vec{D}_j|e_j\rangle$ is the dipole matrix element of the atomic transition.

The cavity field is represented by the creation $a_\mu^\dagger$ and annihilation $a_\mu$ operators in which the subscript $\mu$ indicates the particular set of the cavity plane-wave modes $\mu = \{\vec{k}_n, l\}$ of the wave number $k_n = \omega_n/c$, frequency $\omega_n$ and polarization $l$, to which the atoms are coupled.

The cavity field at position $\vec{x}$ can be given in the plane-wave mode expansion as

$$\vec{E}(\vec{x}) = i \sum_\mu \mathcal{E}_\mu \left( a_\mu \mathrm{e}^{i\vec{k}_n \cdot \vec{x}} \hat{e}_l - \mathrm{H.c.} \right), \tag{1.6}$$

where

$$\mathcal{E}_\mu = \sqrt{\frac{\hbar\omega_n}{2\epsilon_0 L}}, \tag{1.7}$$

is the electric field amplitude of the $n$th mode, $\omega_n = 2\pi nc/L$ is in the frequency of the modes set by the periodic boundary conditions of the ring cavity, and $\hat{e}_l$ is the unit polarization vector of the mode $\mu$.

After substituting Eqs. (1.5) and (1.6) into Eq. (1.4), and retaining only the terms which play a dominant role in the rotating wave approximation, the interaction Hamiltonian takes the form

$$H_{af} = i\hbar \sum_{j=1}^{2} \sum_\mu \left[ g_\mu(\vec{x}_j) a_\mu S_j^+ - \mathrm{H.c.} \right], \tag{1.8}$$

where

$$g_\mu(\vec{x}_j) = \frac{\mathcal{E}_\mu}{\hbar} \left( \vec{d}_j \cdot \hat{e}_l \right) \mathrm{e}^{i\vec{k}_n \cdot \vec{x}_j} \tag{1.9}$$

is the position-dependent Rabi frequency which determines the strength of the coupling of the $j$th atom with the mode $\mu$ of the cavity field.

Our objective is to find effects of the retardation in the interaction of the atoms with the multi-mode cavity field on the evolution of the system. We are in particular interested in the effect of the retardation on the creation of entanglement between the atoms. Two cases will be studied, with the system initially (1) in a single excitation state, and (2) in a double excitation state. Before going into detailed calculations, we first briefly explain how retardation effects are incorporated in our calculations.

### 1.2.2 Origin of the retardation

The atom-cavity system exhibits retardation effects if its dynamics is affected by the finite propagation time of the light. In our model, two effects need to be distinguished [21]. First, an atom embedded in a larger cavity initially evolves as in free space, but after a finite time of order $L/c$ (and integer multiples thereof) reacts to the presence of the cavity with a sudden kink in the time evolution. Speaking pictorially, this time is required for a photon emitted by the atom to cycle through the cavity and be reabsorbed by the same atom. This gives rise to retardation effects which occur already for a single atom in the cavity. The second effect is due to the interaction of two atoms in the cavity. Here, the retardation occurs because of the finite time required for a photon to travel between the two atoms.

In the following, we provide an intuitive picture how the distance information required for the two different retardation effects enters our model. This discussion will be made more precise in Sec. 1.3.1, where we identify the origin of the two types of retardation in the equations of motion governing the atom-cavity system.

A typical representation of the interaction of an atom with a cavity field is illustrated in Fig. 1.2. Evaluating the electric field operator (1.6) in the Heisenberg picture to include the time evolution, we find

$$\vec{E}(\vec{x}) = i \sum_{\mu} \mathcal{E}_{\mu} \left( a_{\mu} \mathrm{e}^{i\varphi_n(\vec{x},t)} \hat{e}_l - \mathrm{H.c.} \right) . \tag{1.10}$$

The time and space dependence enters via the phases $\varphi_n(\vec{x},t) = \vec{k}_n \vec{x} - \omega_n t = \omega_n (x/c - t)$ of the different modes. In the last step and throughout this section, we assume a one-dimensional problem, and thus $\vec{k}_n \vec{x} = k_n x$ for simplicity.

Let us first discuss a simplified model, the interaction of the atom with a single mode only, say the central cavity mode $\mu = 0$, as shown in Fig. 1.2(a). Suppose now that atom 1 represented by a red blob is located at position $x_1$, whereas atom 2, represented by a blue blob can be located at three different positions $x_2, x_{2'}$ and $x_{2''}$. It is easily verified that if $x$ is displaced by $\delta x$ such that $k_0 \cdot \delta x = 2\pi n$, where $n$ is an integer, then the phase of the single mode remains unchanged, $\varphi_0(x,t) = \varphi_0(x + \delta x, t)$. This implies that the electric field operator has the same value at positions differing by an integer multiple of the cavity wavelength. Hence, the interaction Hamiltonian $H_{af}$ remains the same if the distance between the two atoms is changed by an integer multiple of the wavelength. In this sense, the system dynamics is independent of the distance, and thus the system itself cannot exhibit effects of retardation if only a single mode is considered.

It should be noted that the interaction Hamiltonian still depends on the relative distance between the atoms. For atomic separations $|x_2 - x_1|$ and $|x_{2'} - x_1|$ that are equal to multiple integer of the wavelength, $g_0(x_1) = g_0(x_2) = g_0(x_{2'})$, since at these separations the Rabi frequencies have the same value. In other words, the atoms are coupled equally to the field mode. But for separations between the atoms that do not satisfy the periodicity condition, such as $|x_{2''} - x_1|$, the atoms experience different amplitudes and phases of the field. As a consequence, the interaction $H_{af}$ is modified due to to a change of the Rabi

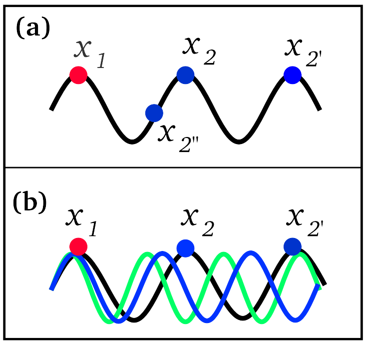

Figure 1.2: (Color online) Atoms represented by colored blobs inside the cavity field. $x_1$ denotes the position of atom 1 which is placed at the first anti node. (a) Single mode of the cavity field with three different positions for atom 2. (b) Two additional modes shown in blue and green are taken into account.

frequency. However, this variation of the interaction Hamiltonian with the inter atomic distance in the single mode field has nothing to do with retardation.

Let us now assume that apart from the central mode, there are additional cavity modes taking part in the interaction with the atoms, as illustrated in Fig. 1.2(b). Suppose that at point $x_1$, all modes have the same phase ($\varphi_n(x_1, t) = \varphi_0$ for all $n$), which we for simplicity assume to be zero. Then, the position $x$ entering the field operator can be interpreted as the distance $\delta x = x_2 - x_1$ between the two atoms. Due to their different wave numbers $k_n$, at point $x_2$, the modes typically have different phases, i.e., $\varphi_n(x_2, t) \neq \varphi_m(x_2, t)$ for $n \neq m$. In other words, the modes are shifted or "retarded" with respect to each other. This means that the atom at position $x_2$ experiences the field emitted by atom 1 into the different cavity modes with different relative phases, such that the response of atom 2 in the limit of large mode number averages out. However, at specific times, all modes can evolve in phase again. From the definition of $\varphi_n(x, t)$, it is clear that this happens at times $x/c$, i.e., exactly the times corresponding to the flight time of light between the two atoms. At this instance in time, the cavity modes act in phase onto atom 2, such that a sudden response is observed. This is the origin for the retardation effects of the second type.

In contrast, the retardation effects of the first type are embedded in the quantization of the cavity mode's frequency spectrum. The frequency spacings are such that the phases at times separated by integer multiples of $L/c$ are different by an integer multiple of $2\pi$, as $\omega_n L/c = 2\pi n$. While at most times the different modes are out of phase because of the different free evolution frequencies, at times equal to integer multiples of $L/c$ all modes are in phase again, and a sudden response of the atom appears. From this interpretation, it is apparent that this first type of retardation already occurs for a single atom.

A straightforward combination of both arguments also explains the retardation of the second type at times $(L - x)/c$. Furthermore, in the subsequent evolution of the atoms also combinations of the different retardation time intervals can occur, as we will see in the numerical analysis.

Thus, retardation effects are expected to play an important role in the interaction of atoms as soon as multiple modes with different wave numbers interact with the atoms. This can also be related to the Fourier relation of position and momentum space. The small frequency distribution of a single mode gives rise to a large distribution or uncertainty in the position. In contrast, a broad frequency distribution or many modes allow to precisely determine the position.

## 1.3 Excitation probabilities and concurrence

We are interested in determining the effect of retardation on the time evolution of the system initially prepared in separable states of single and double excitations. In particular, we shall discuss the subsequent time-dependent behavior of the excitation probabilities and the concurrence.

The time evolution of the system is governed by the Schrödinger equation, which in the interaction picture is given by

$$i\hbar\frac{\partial|\psi(t)\rangle}{\partial t} = H_{af}|\psi(t)\rangle. \tag{1.11}$$

Note that this description in terms of the Schrödinger equation does not take into account incoherent processes such as cavity loss or spontaneous emission of the atoms outside of the resonator mode. Therefore, we can only analyze the dynamics over times which are short compared to the lifetime of photons in the cavity mode, and to the lifetime of the excited atomic states. In the following, we will focus on evolution times up to $2000L/c$, which would require a resonator finesse larger than 2000. Resonators with suitable finesses have been achieved with different quantum systems and cavity types [114, 115]. Also typical lifetimes of the respective excited atomic states are much longer than the considered propagation time, such that it is justified to consider the coherent dynamics only.

We will consider two particular classes of initial conditions. In the first, we assume that at $t = 0$ the system was in a single-excitation state. In the second class, we assume that initially two excitations were present in the system. In both cases, the (single or double) excitation is initially either present in the atoms or in the cavity, or in a superposition of atoms and cavity.

### 1.3.1 The case of single excitation

If we take for the initial state of the system a single-excitation state, then the time-dependent state vector of two atoms coupled to a multi-mode field can be written as

$$|\psi(t)\rangle = b_1(t)|e_1g_2\{0\}_\mu\rangle + b_2(t)|g_1e_2\{0\}_\mu\rangle + \sum_\mu b_\mu(t)|g_1g_2\{1\}_\mu\rangle, \tag{1.12}$$

The different kets in the above equation specify the electronic state of the first atom, the electronic state of the second atom and the field state in the Fock state representation, respectively, that is, $|i_1 j_2 \{k\}_\mu\rangle = |i_1\rangle \otimes |j_2\rangle \otimes |\{k\}_\mu\rangle$. $\{1\}_\mu$ denotes the state of the cavity modes with a single excitation present in the mode $\mu$ and zero occupation numbers for all the remaining modes.

The time evolution of the state vector is determined by the Schrödinger equation (1.11) which transforms it into three coupled equations of motion for the probability amplitudes

$$\dot{b}_j(t) = \sum_\mu g_{\mu j} b_\mu(t), \quad j \in \{1,2\}, \tag{1.13a}$$

$$\dot{b}_\mu(t) = -\, i\Delta_\mu b_\mu(t) - \sum_{j=1}^{2} g^*_{\mu j} b_j(t), \tag{1.13b}$$

where $\Delta_\mu = \omega_\mu - \omega_a$ is the detuning of the cavity mode frequency $\omega_\mu$ from the atomic transition frequency $\omega_a$ coinciding with the central cavity mode frequency, and we have simplified the notation $g_{\mu i} \equiv g_\mu(\vec{x}_i)$.

The formal integration of Eq. (1.13b) gives

$$b_\mu(t) = b_\mu(0)\mathrm{e}^{-i\Delta_\mu t} - \sum_{j=1}^{2} g^*_{\mu j} \int_0^t dt' b_j(t')\mathrm{e}^{-i\Delta_\mu (t-t')}, \tag{1.14}$$

and when this relation is substituted into Eq. (1.13a), we find

$$\dot{b}_j(t) = \sum_\mu g_{\mu j} b_\mu(0)\mathrm{e}^{-i\Delta_\mu t} - \sum_{j'=1}^{2} \int_0^t dt' \sum_\mu g_{\mu j} g^*_{\mu j'} b_{j'}(t-t')\mathrm{e}^{-i\Delta_\mu t'}. \tag{1.15}$$

At this point, the two types of retardation effects are fully visible also from the analytical expressions. The first type leading to retardation effects at times equal to integer multiples of the cavity round trip time $L/c$ can be understood in terms of the detunings $\Delta_\mu$. Since the detunings $\Delta_\mu$ differ by integer multiples of $2\pi c/L$, the phases $\Delta_\mu t$ will be multiples of $2\pi$ for all modes $\mu$ simultaneously at times $t$ equal to integer multiples of $L/c$. Then, the system response will exhibit sharp peaks due to the constructive interference of all modes. At other times, the different phase factors of the various modes do not add up constructively. This discrete response is independent of the coupling between the atoms, and could be observed even if only a single atom is present inside the cavity.

The second type of retardation is due to the interaction between the atoms, i.e., the second part of Eq. (1.15). The coupling constants $g_{\mu j} g^*_{\mu j'}$ together with the detuning phase lead to phase contributions $i[k_\mu(x_1 - x_2) - \omega_\mu t] = i\omega_\mu[(x_j - x'_j)/c - t]$ for the different modes. Again, constructive interference is obtained, but in this case at a time corresponding to the flight time $x/c$ between the two atoms. A similar argument also explains constructive interference at time $(L-x)/c$.

Subsequent iterations of the two types of retardation lead to kinks in the system evolution also at times arising from combinations of the two effects. Obviously, constructive interference can only lead to sharp change in the system response if many different frequency components contribute, i.e., if the system couples to many cavity modes. In the extreme case of free space, $L \to \infty$, and the first type of retardation cannot occur at a finite time. But the retardation in the coupling between the two atoms is still present in the free-space limit, and must be considered, e.g., in calculating the dipole-dipole coupling between atoms in free space.

### 1.3.2 The case of double excitation

If initially the system was in a double excitation state, then the state vector can be written as

$$\begin{aligned} |\tilde{\psi}(t)\rangle = {} & b_{12}(t)|e_1e_2\{0\}_\mu\rangle + \sum_\alpha b_{\alpha 1}(t)|e_1g_2\{1\}_\alpha\rangle + \sum_\alpha b_{\alpha 2}(t)|g_1e_2\{1\}_\alpha\rangle \\ & + \sum_\alpha b_{\alpha\alpha}(t)|g_1g_2\{2\}_\alpha\rangle + \sum_{\alpha>\beta} b_{\alpha\beta}(t)|g_1g_2\{1\}_\alpha\{1\}_\beta\rangle, \end{aligned} \tag{1.16}$$

where $\{2\}_\alpha$ denotes the state of the cavity modes with double excitation of the mode $\alpha$ and zero occupation numbers for all the remaining modes.

The Schrödinger equation transforms the state vector (1.16) into the following set of coupled equations of motion for the probability amplitudes

$$\begin{aligned} \dot{b}_{12}(t) = {} & \sum_{j\neq j'=1}^{2} \sum_\alpha g_{\alpha j} b_{\alpha j'}(t), \\ \dot{b}_{\alpha j}(t) = {} & -i\Delta_\alpha b_{\alpha j}(t) - g^*_{\alpha j'} b_{12}(t) + \sqrt{2} g_{\alpha j} b_{\alpha\alpha}(t) + \sum_{\beta>\alpha} g_{\beta j} b_{\beta\alpha}(t) + \sum_{\beta<\alpha} g_{\beta j} b_{\alpha\beta}(t), \\ & (j \neq j' \in \{1,2\}), \\ \dot{b}_{\alpha\beta}(t) = {} & -i(\Delta_\alpha + \Delta_\beta) b_{\alpha\beta}(t) - \sum_{j=1}^{2} \left[ g^*_{\alpha j} b_{\beta j}(t) + g^*_{\beta j} b_{\alpha j}(t) \right], \\ \dot{b}_{\alpha\alpha}(t) = {} & -2i\Delta_\alpha b_{\alpha\alpha}(t) - \sqrt{2} \sum_{j=1}^{2} g^*_{\alpha j} b_{\alpha j}(t). \end{aligned} \tag{1.17}$$

The case of double excitation is described by a complicated set of equations of motion. It involves probability amplitudes of the states with the excitation redistributed over two cavity modes, $b_{\alpha\beta}(t)$, as well as states with the excitation occupying the same mode $b_{\alpha\alpha}(t)$.

### 1.3.3 Concurrence

We are mainly interested in studying the retardation effects on the entanglement dynamics between the two atoms that are coupled to the multi mode vacuum field inside the cavity. The dynamics of the atoms are determined by the reduced density matrix $\rho$ that is obtained by tracing the density matrix of the total system over the field degrees of freedom. We then exploit concurrence introduced by Wootters [56, 57], which is a widely accepted measure of entanglement between two qubits, and is defined by

$$C = \max\{0, \sqrt{\lambda_1} - \sqrt{\lambda_2} - \sqrt{\lambda_3} - \sqrt{\lambda_4}\}, \tag{1.18}$$

where $\lambda_i$ are the eigenvalues (in descending order) of the Hermitian matrix $R = \rho\tilde{\rho}$ in which $\tilde{\rho}$ is given by

$$\tilde{\rho} = \sigma_y \otimes \sigma_y \rho^* \sigma_y \otimes \sigma_y. \tag{1.19}$$

and $\sigma_y$ is a Pauli matrix. The concurrence ranges between 0 and 1. If the two atoms are maximally entangled, the concurrence evaluates to unity whereas, if they are completely disentangled, $C = 0$.

The usual way is to express the concurrence in the basis of the product states of the two-atom system, i.e., $|1\rangle = |e_1 e_2\rangle, |2\rangle = |e_1 g_2\rangle, |3\rangle = |g_1 e_2\rangle, |4\rangle = |g_1 g_2\rangle$. In this basis, the concurrence takes the form [99]

$$C(t) = 2\max\bigl\{0, |\rho_{23}(t)| - \sqrt{\rho_{44}(t)\rho_{11}(t)}, |\rho_{14}(t)| - \sqrt{\rho_{22}(t)\rho_{33}(t)}\bigr\}. \tag{1.20}$$

There are two terms contributing to the concurrence, one resulting from the presence of the one-photon coherence $|\rho_{23}(t)|$ and the other from the two-photon coherence $|\rho_{14}(t)|$. It is interesting that these two contributions complement each other. In the single excitation case, $\rho_{11} = 0, \rho_{14} = 0$, and then the expression for the concurrence (denoted in this case by $\mathbf{C}$) reduces to

$$\mathbf{C}(t) = 2\max\{0, |\rho_{23}(t)|\} = 2\max\{0, |b_1^*(t)\, b_2(t)|\}. \tag{1.21}$$

It shows that in the single excitation case it is sufficient for $|\rho_{23}(t)|$ to be different from zero to create entanglement between the atoms. In this sense, entanglement is equivalent to atomic coherence in this case.

The situation is quite different when two excitations are present in the system. But surprisingly, tracing the density matrix of the system over the field degrees of freedom results in an expression for the concurrence that does not involve the two-photon coherence $\rho_{14}(t)$. To see this more explicitly, we calculate the density matrix $\rho_T$ associated with the two-excitation state Eq. (1.16), and find

$$\begin{aligned}
\rho_T = {} & |b_{12}(t)|^2 |e_1 e_2\{0\}_\mu\rangle\langle e_1 e_2\{0\}_\mu| + \sum_\alpha |b_{\alpha 1}(t)|^2 |e_1 g_2\{1\}_\alpha\rangle\langle e_1 g_2\{1\}_\alpha| \\
& + \sum_\alpha b_{\alpha 1}(t) b_{\alpha 2}^*(t) |e_1 g_2\{1\}_\alpha\rangle\langle g_1 e_2\{1\}_\alpha| + \sum_\alpha b_{\alpha 2}(t) b_{\alpha 1}^*(t) |g_1 e_2\{1\}_\alpha\rangle\langle e_1 g_2\{1\}_\alpha| \\
& + \sum_\alpha |b_{\alpha 2}(t)|^2 |g_1 e_2\{1\}_\alpha\rangle\langle g_1 e_2\{1\}_\alpha| + \sum_{\alpha>\beta} |b_{\alpha\beta}(t)|^2 |g_1 g_2\{1\}_\alpha\{1\}_\beta\rangle\langle g_1 g_2\{1\}_\alpha\{1\}_\beta| \\
& + \sum_\alpha |b_{\alpha\alpha}(t)|^2 |g_1 g_2\{2\}_\alpha\rangle\langle g_1 g_2\{2\}_\alpha| + ND,
\end{aligned} \tag{1.22}$$

where $ND$ stands for the sum of all off-diagonal terms in the field modes which vanish in tracing over the cavity modes. Then, by taking trace of the density matrix $\rho_T$ over the cavity modes, we arrive at the following reduced density matrix of the two atoms

$$\rho = |b(t)|^2|1\rangle\langle 1| + \sum_\alpha |b_{\alpha 1}(t)|^2\,|2\rangle\langle 2| + \sum_\alpha |b_{\alpha 2}(t)|^2\,|3\rangle\langle 3| + \sum_\alpha b_{\alpha 1}(t)b^*_{\alpha 2}(t)\,|2\rangle\langle 3| + \sum_\alpha b_{\alpha 2}(t)b^*_{\alpha 1}(t)\,|3\rangle\langle 2| + \left(\sum_{\alpha>\beta}|b_{\alpha,\beta}(t)|^2 + \sum_\alpha |b_{\alpha,\alpha}(t)|^2\right)|4\rangle\langle 4|. \tag{1.23}$$

It is clear that tracing out the field modes results in the density matrix with $\rho_{14} = 0$. In this case, the concurrence denoted by $\mathcal{C}$ takes the form

$$\mathcal{C}(t) = 2\max\left\{0, |\rho_{23}(t)| - \sqrt{\rho_{44}(t)\rho_{11}(t)}\right\}, \tag{1.24}$$

which in terms of the probability amplitudes can be written as

$$\mathcal{C}(t) = \max\{0, \mathcal{C}_1(t)\}, \tag{1.25}$$

where

$$\mathcal{C}_1(t) = 2\sum_\alpha |b^*_{\alpha 2}(t)b_{\alpha 1}(t)| - |b(t)|\sqrt{\sum_{\alpha>\beta}|b_{\alpha,\beta}(t)|^2 + \sum_\alpha |b_{\alpha,\alpha}(t)|^2}. \tag{1.26}$$

Similar to the single excitation case, the concurrence depends on the coherence $\rho_{23}(t)$. However, in the presence of two excitations in the system, the condition for a nonzero concurrence of $|\rho_{23}(t)| \neq 0$ is a necessary one, it is not in general sufficient one, since there is a subtle condition of the coherence to be larger than a threshold value of $\sqrt{\rho_{44}(t)\rho_{11}(t)}$. Thus, the presence of the two excitations in the system introduces a threshold for the coherence above which the entanglement between the atoms could occur. Needless to say, the first term in Eq. (1.26), $|b^*_{\alpha 2}(t)b_{\alpha 1}(t)|$, must be different from zero and exceed the second term numerically for the concurrence to be positive.

We should point out here that the involvement of only the one-photon coherence in the concurrence of the double excitation case is a direct consequence of the quantum nature of the field. The definite total excitation number entangles the excitation number of the atoms uniquely to the excitation number of the cavity. If the cavity is projected into particular excitation number channels with classical probabilities not allowing for quantum superpositions in tracing over the cavity modes, due to this entanglement, also the atoms are projected into the corresponding excitation number subspaces. This rules out coherence or even entanglement between atomic states of different excitation number. This situation was treated by Yönaç *et al.* [116,117], who showed that in the case of a two mode cavity, $\alpha \in \{1, 2\}$, no coherence and equivalently no entanglement can be found in a system determined by the double excitation state (1.16).

The coherence could be present if one includes an auxiliary state $|g_1 g_2\{0\}_\alpha\{0\}_\beta\rangle$, the ground state with no excitation, to the state (1.16). Then, the total excitation number would not be fixed, and there would be no definite entanglement between the atom and cavity excitation numbers. Alternatively, if the photon number states in Eq. (1.22) were replaced by a classical field amplitude, for example, by a coherent state $|\alpha\rangle$, one could then arrive at the concurrence involving the two-photon coherence $\rho_{14}$. Thus, the condition for entanglement based on $\rho_{14}$ would become relevant. It is easy to see, replacing in Eq. (1.22) the photon number states $|\{n\}_\mu\rangle$ by the coherent state $|\alpha\rangle$, we obtain a state vector

$$|\hat{\psi}(t)\rangle = b_{12}(t)|e_1e_2\alpha\rangle + \sum_\alpha b_{\alpha 1}(t)|e_1g_2\alpha\rangle + \sum_\alpha b_{\alpha 2}(t)|g_1e_2\alpha\rangle + \sum_\alpha b_{\alpha\alpha}(t)|g_1g_2\alpha\rangle. \quad (1.27)$$

Using $\hat{\psi}(t)$ from Eq. (1.27), one can calculate the density matrix $\rho^{cl}$. Now

$$\begin{aligned}\rho^{cl}_{14} =&\langle 1|\rho^{cl}|4\rangle \\ =&b^*_{12}(t)b_{\alpha\alpha}(t)\langle e_1e_2\alpha|\hat{\psi}(t)\rangle\langle\hat{\psi}(t)|g_1g_2\alpha\rangle \\ =&|b^*_{12}(t)|^2|b_{\alpha\alpha}(t)|^2.\end{aligned} \quad (1.28)$$

It is seen that the resulting density matrix element containing contributions from the two-photon coherences no more vanishes. This is consistent with our interpretation, as a coherent state has a distribution of photon numbers rather than a well-defined occupation as a Fock state.

## 1.4 Results and discussion

Having discussed the general features of the concurrence, we now turn to analyze the transient behavior of the populations and concurrence for initial conditions in which the atoms are prepared in separable single or double excitation states and for an initial condition in which the atoms are initially in a partially or a maximally entangled state. We shall allow for an arbitrary inter atomic spacing and length of the cavity, but we limit the discussion to situations in which the central cavity mode is in resonance with the transition frequency of the atoms, i.e., $\omega_0 = \omega_a$. Also, since the coupling of the atoms to the cavity modes decreases with increasing detuning, we take into account in the numerical calculation a finite number of cavity modes distributed about $\omega_0$ with a frequency range on the order of several atomic line widths. The required number of modes depends on the cavity length $L$, as the distance between the adjacent cavity modes decreases with increasing $L$. Thus, the number of the cavity modes to which the atoms can be coupled increases with an increasing $L$.

Equations (1.21) and (1.24) for the concurrence are functions of several parameters: the inter atomic spacing $x$, the detuning of the cavity modes from the atomic transition frequency $\Delta_\mu$, the number of the cavity modes $N$ to which the atoms are coupled, the coupling strength of the atoms to the cavity modes $g_{\mu i}$, the cavity length $L$, and the time $t$. For fixed $N$ and $L$, one can obtain time evolution of the concurrence by monitoring the populations of the atomic states and coherence between the atoms as a function of $t$. Alternatively, one can monitor the time evolution of the populations of the collective states of the two-atom system. In the following, we give illustrative figures of both on a short time and a long time behavior of the concurrence.

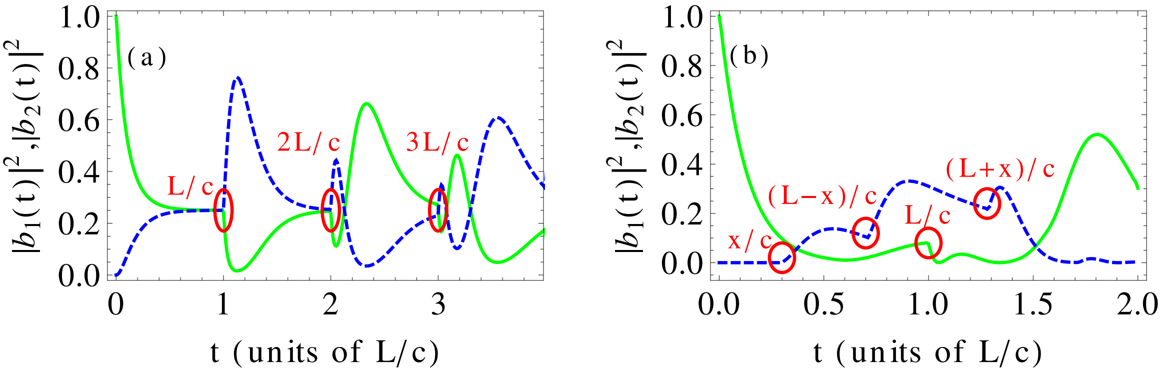

Figure 1.3: (Color online) The time variation of the probabilities $|b_1(t)|^2$ (solid green line) and $|b_2(t)|^2$ (dashed blue line) for $L = 3.48 \times 10^3\lambda_a$, $N = 99, \omega_a = 1.11 \times 10^4\Omega_0$, where $\Omega_0$ is the vacuum Rabi frequency of the central resonant mode, and inter atomic spacings: (a) $x = 0$ and (b) $x = 999\lambda_a$. The sudden jumps of the probabilities due to retardation are marked by red circles. The first atom is located at $x_1 = 1\lambda_a$. Note that in the case (b), the atom "2" starts to become excited after a finite time, $t = x/c$, that is due to the retardation.

### 1.4.1 Effects of retardation on the population dynamics

Before discussing the effects of retardation on the transient properties of the concurrence, it is important to understand the transient behavior of the populations of the single-excitation case. Transient excitation probabilities are first studied for arbitrary initial conditions for the atomic and the collective states of the system. The effects of retardation on the population dynamics were studied by Goldstein and Meystre [21]. However, these calculations were not specifically oriented towards studying the transient properties of the collective states of the system which, as we shall see below, are very useful for the interpretation of the entanglement dynamics of the atoms.

To calculate the population dynamics, we solve numerically the set of coupled equations for the probability amplitudes, Eqs. (1.13a)-(1.13b), assuming that the atoms were prepared at time $t = 0$ in a product state

$$|\psi(0)\rangle = |e_1\rangle \otimes |g_2\rangle \otimes |\{0\}_\mu\rangle \equiv |e_1 g_2 \{0\}_\mu\rangle, \tag{1.29}$$

where $|\{0\}_\mu\rangle$ denotes the product state vector of the cavity modes with zero occupation numbers for all the modes $\mu$. The initial condition (1.29) corresponds to $b_1(0) = 1$ and $b_2(0) = b_\mu(0) = 0$. We then compute the time evolution of the excitation probabilities $|b_1(t)|^2$ and $|b_2(t)|^2$ of the atoms.

Figure 1.3 shows the time evolution of $|b_1(t)|^2$ and $|b_2(t)|^2$ for two different inter atomic spacings. The frame (a) illustrates the case when the atoms are very close to each other, with spacing $x \approx 0$. We see that the initially excited atom decays almost exponentially in time, corresponding to the free space regime defined in [21]. A part of the excitation is transferred directly to the second atom. There is no delay in the excitation of the second

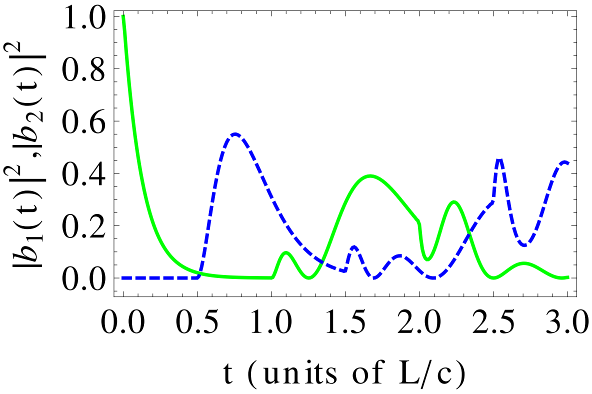

Figure 1.4: (Color online) Time variation of the probabilities $|b_1(t)|^2$ (solid green line) and $|b_2(t)|^2$ (dashed blue line) for the same parameters as in Fig. 1.3 except that $x = L/2$.

atom, as the inter atomic spacing is negligibly small. A notable feature of the temporal evolution is that at the particular times that correspond to $nL/c$, where $n$ is an integer, a sudden change (jump) in the probabilities occurs. These are just the times when the radiation field emitted into the cavity modes returns to the atoms. It is interesting that the returning radiation does not simultaneously excite both atoms, as one could expect. It rather stimulates a sudden transfer of the population from atom 1 to atom 2.

The sudden jumps continue in time. However, the periodic maxima of the populations are reduced in magnitude as $t$ increases. This result is consistent with energy-time uncertainty arguments and is readily understood if it is recalled that the excitation wave packet spreads during the evolution, that is, the excitation becomes less localized as time progresses. An alternative explanation is that there are more and more possible evolution pathways for the excitation to open up as time progresses that are possibly delayed with respect to each other, e.g., due to temporary re-absorptions by the atoms, and then interfere resulting in increased distortions of $|b_1(t)|^2$ and $|b_2(t)|^2$.

Frame (b) of Fig. 1.3 illustrates the time evolution of the probabilities for a large inter atomic spacing, $x = 999\lambda_a$. There are now two pathways for the excitation to be transferred between the atoms, $x$ and $L-x$. At very early times, $t \ll L/c$, the initially excited atom 1 decays with the rate equal to the free space decay rate. The atom 2 remains in its ground state indicating that initially the excitation is exclusively transferred to the cavity, which essentially appears as open space. The atom 2 remains in its ground state until the time $t = x/c$, at which the population of the atom 2 abruptly starts to build up. This is the time required for the excitation emitted by the atom 1 to reach the atom 2 through the shorter pathway $x$. The population of the atom 2 changes abruptly again at time $t = (L-x)/c$. Note that the abrupt buildup of the excitation of the atom 2 is not accompanied by an abrupt de-excitation of the atom 1. There are no sudden changes of the population of the atom 1 until the time $t = L/c$. This is the time the excitation returns for the first time to the atom 1. In fact, neither of the sudden changes of the population of one of the atoms are accompanied by sudden changes of the other. This feature is linked to the fact that the atoms are at different positions and we have taken $x < L/2$.

Of particular interest is the situation when the two atoms are separated by a distance equal to half of the cavity length, Fig. 1.4. While the sudden kinks in the time evolution of the probability $|b_1(t)|^2$ are still observed at integer multiples of time $L/c$, the number of kinks in evolution of $|b_2(t)|^2$ reduce to one half as the two paths available for radiation to travel from atom 1 to atom 2 are now of equal length. Therefore, in the time behavior of $|b_2(t)|^2$, kinks are witnessed only at odd integer multiples of $L/(2c)$. Another interesting observation is that there are no sudden jumps of the populations at times $2nx/c$ and $2n(L-x)/c$, where $n$ is an integer, indicating that the excitation wave packets do not appear to reverse their propagation directions during the interaction with the other atom.

A physical understanding of these behaviors can be obtained if we consider the atomic dynamics in terms of the collective Dicke states of the two-atom system

$$\begin{aligned} |g\rangle &= |g_1\rangle \otimes |g_2\rangle, \\ |s\rangle &= \frac{1}{\sqrt{2}}\left(|e_1\rangle \otimes |g_2\rangle + |g_1\rangle \otimes |e_2\rangle\right), \\ |a\rangle &= \frac{1}{\sqrt{2}}\left(|e_1\rangle \otimes |g_2\rangle - |g_1\rangle \otimes |e_2\rangle\right). \end{aligned} \tag{1.30}$$

The advantage of expressing the system in terms of the Dicke state basis is that we can immediately see in which collective state the excitation evolves in time.

Using Eqs. (1.12) and (1.30), we find that the excitation probabilities of the collective symmetric $|s\rangle$ and the antisymmetric $|a\rangle$ states are

$$\begin{aligned} |b_s(t)|^2 &= \frac{1}{2}\left(|b_1(t)|^2 + |b_2(t)|^2 + 2\mathrm{Re}\left[b_1(t)b_2^*(t)\right]\right), \\ |b_a(t)|^2 &= \frac{1}{2}\left(|b_1(t)|^2 + |b_2(t)|^2 - 2\mathrm{Re}\left[b_1(t)b_2^*(t)\right]\right). \end{aligned} \tag{1.31}$$

Figure 1.5 shows how the probabilities $|b_s(t)|^2$ and $|b_a(t)|^2$ evolve in time. At $t = 0$, the collective states $|s\rangle$ and $|a\rangle$ are populated with the same probabilities, $|b_s(t)|^2 = |b_a(t)|^2 = 1/2$. The population of the symmetric state decays exponentially in time whereas the population of the antisymmetric state remains constant in time. In this figure, the two atoms couple to the cavity modes symmetrically as $x = 0$. Therefore, the anti-symmetric excitation state effectively decouples from the cavity, reminiscent of electromagnetically induced transparency or decoherence free sub-spaces. A similar effect can be achieved if the two atoms couple anti-symmetrically to the cavity, in which case the symmetric excitation state remains constant in time. In contrast, the symmetric state in Fig. 1.5 becomes re-excited periodically at the time instants given by $nL/c$, where $n$ is an integer. At these times, the emitted radiation field returns to the atoms chronologically.

We see that the simultaneous sudden changes of both probabilities at the particular discrete times can be explained as an excitation of the collective atomic system from the

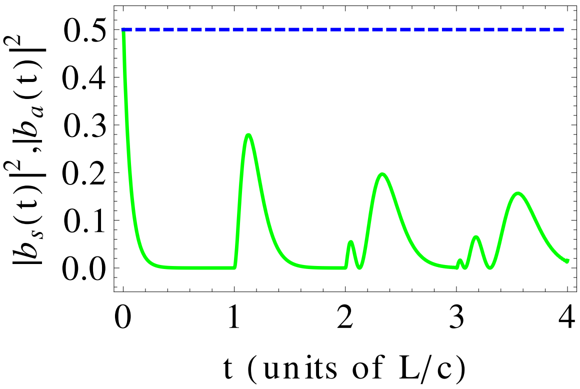

Figure 1.5: (Color online) Variation of the excitation probabilities $|b_s(t)|^2$ (solid green line) and $|b_a(t)|^2$ (dashed blue line) with time for the same parameters as in Fig. 1.3(a).

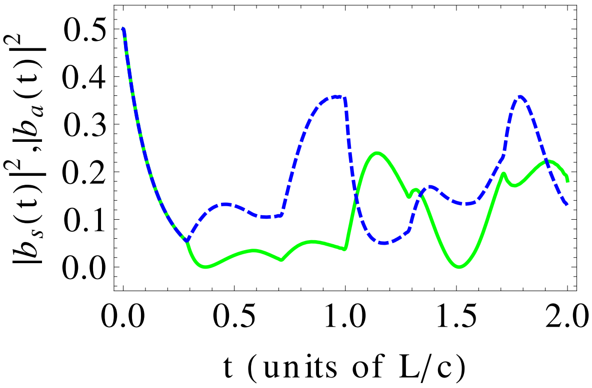

Figure 1.6: (Color online) Variation of the probabilities $|b_s(t)|^2$ (solid green line) and $|b_a(t)|^2$ (dashed blue line) with time for the same situation as in Fig. 1.3(b).

ground state to the symmetric state. In other words, the jumps represent a collective excitation of the atomic system by the returning radiation field.

It is interesting to note that shortly before the sudden re-excitation times, the state of the atomic system is

$$\begin{aligned} |\psi(t = nL/c)\rangle =& \frac{1}{\sqrt{2}} \left(|g\rangle + |a\rangle\right), \\ =& \frac{1}{\sqrt{2}}|gg\rangle + \frac{1}{2}(|eg\rangle - |ge\rangle), \end{aligned} \tag{1.32}$$

which shows that the system is in an equal superposition of the ground $|g\rangle$ and the anti-symmetric $|a\rangle$ states of the two-atom system and explains why in Fig. 1.3(a) $|b_1(nL/c)|^2 = |b_2(nL/c)|^2 = 1/4$.

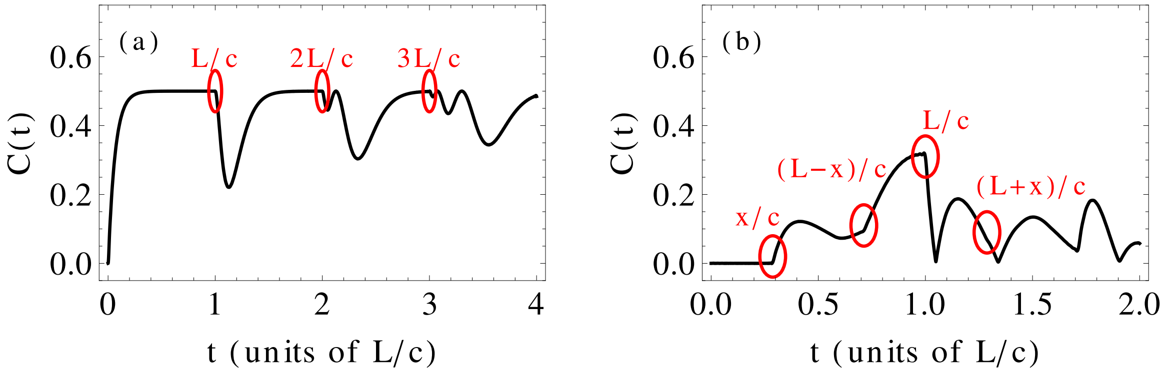

Figure 1.7: (Color online) Transient buildup of entanglement from the initial separable state $|e_1 g_2\{0\}_\mu\rangle$ for inter atomic spacings: (a) $x = 0$ and (b) $x = 999\lambda_a$. The other parameters are the same as in Fig. 1.3. The red circles mark the positions of the kinks due to retardation.

Figure 1.6 shows the time evolution of the populations of the symmetric and antisymmetric states for the same situation as in Fig. 1.3(b). The initial populations decay exponentially with the same rates until $t = x/c$, at which the sudden jump of the populations occurs. A notable difference between the time evolution of $|b_s(t)|^2$ and $|b_a(t)|^2$, and that of the individual atoms $|b_1(t)|^2$ and $|b_2(t)|^2$, shown in Fig. 1.3(b), is the occurrence of the sudden jumps at the same discrete times. Notice that the most dramatic change in the populations occurs at the time $t = L/c$, i.e. when the excitation returns to the initially excited atom 1.

### 1.4.2 Effects of retardation on entanglement - single excitation case

We now turn to the discussion of the effects of retardation on the entanglement between the atoms. We first focus on short time behavior of the concurrence with two sets of initial conditions in which atoms are prepared in the separable state (1.29) and the maximally entangled state

$$|\psi(0)\rangle = \frac{1}{\sqrt{2}}\left(|e_1\rangle \otimes |g_2\rangle + |g_1\rangle \otimes |e_2\rangle\right) \otimes |\{0\}_\mu\rangle. \tag{1.33}$$

The concurrence in the single excitation case can be determined from Eq. (1.21) in which the probability amplitudes are found solving the set of two coupled equations (1.15).

We graph the effect of the retardation on the transient buildup of entanglement between the atoms from the initial separable state Eq. (1.29) for inter atomic spacings $x = 0$ and $x = 999\lambda_a$, respectively, in Figs. 1.7(a) and 1.7(b). We can see how the entanglement between the atoms is affected by the retardation and how it could be related to the population of the collective states. A comparison of Fig. 1.7(a) with Fig. 1.5 shows that for $x = 0$ the manner in which the concurrence evolves in time resembles the evolution of the population of the symmetric state. This is readily understood if one writes the

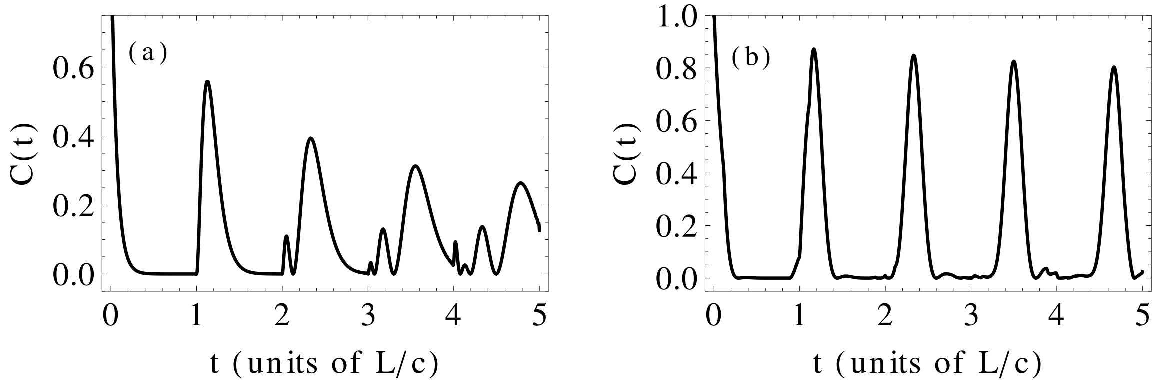

Figure 1.8: Concurrence as a function of time for the same parameters as in Fig. 1.3 except that the atoms were initially prepared in the maximally entangled state $|s\rangle$. The inter atomic spacing is in (a) $x = 0$, and in (b) $x = 999\lambda_a$.

concurrence Eq. (1.21) in the basis of the collective Dicke states to find

$$\mathbf{C}(t) = \max\left\{0, \sqrt{[\rho_{ss}(t) - \rho_{aa}(t)]^2 + (2\mathrm{Im}\,[\rho_{as}(t)])^2}\right\}. \tag{1.34}$$

Since $\rho_{ss}(0) = \rho_{aa}(0) = 1/2$, and at short times $\mathrm{Im}[\rho_{as}(t)] \approx 0$, the time evolution of the concurrence depends essentially on the evolution of the population $\rho_{ss}(t)$. It is seen that $\mathbf{C}(t) > 0$ for all times except $t = 0$. It is only at $t = 0$ that the atoms are unentangled. The most positive value of $\mathbf{C}(t)$ is achieved when $\rho_{ss}(t) = 0$, in which case $\mathbf{C}(t) = 1/2$, so that we may speak of 50% entanglement. The effect of retardation shows up clearly as the sharp decrease of the concurrence from its maximal value of 1/2. This is due to the transfer of the population from the ground state $|g\rangle$ to the symmetric state $|s\rangle$.

Figure 1.7(b) shows the time evolution of the concurrence for a large inter atomic spacing, $x = 999\lambda_a$. The effect of going to a nonzero inter atomic spacing is clearly to decrease the amount of entanglement and to restrict the time during which it occurs. We see that the initially unentangled atoms remain separable until the time $t = x/c$. The physical reason for the delay in the creation of entanglement is in the retardation effect. No entanglement is created between the atoms until the photon emitted by atom 1 reaches atom 2. The atoms remain entangled until the time $t = L/c$ at which the excitation returns to atom 1. At this time the concurrence suddenly drops to zero. The behavior of the concurrence is entirely consistent with the behavior of the populations of the symmetric and the antisymmetric states, shown in Fig. 1.6.

Equation (1.34) predicts that for maximal entanglement between the atoms we would need to put all of the population in one of the collective states, either $|s\rangle$ or $|a\rangle$. Following this observation, we plot in Fig. 1.8(a) the time evolution of the concurrence for the same parameters as in Fig. 1.7(a), but with the new initial condition $\rho_{ss}(0) = 1$, i.e., the atoms are initially prepared in the maximally entangled state $|s\rangle$. Since $\rho_{aa}(t) = 0$ for $t \geq 0$, the dynamics of the system reduces to that between two states only, the symmetric $|s\rangle$

and the ground $|g\rangle$ states. In this case the concurrence is simply equal to the population of the symmetric state, $\mathbf{C}(t) = \rho_{ss}(t)$. For $t = 0$ the atoms are maximally entangled due to our choice of the initial state of the system. Immediately afterwards, the concurrence begins to decrease because of the spontaneous emission to the cavity modes. As soon as the emitted light returns to the atoms, that happens periodically at the times equal to $nL/c$, where $n$ is an integer, the atoms thereafter become entangled because the system returns to the symmetric state. In the time $t < L/c$, the concurrence approaches zero. This effect, however, is not sudden death of entanglement because $\mathbf{C}(t)$ does not become exactly zero. We already found previously that the concurrence for the case of having only one quantum of energy in the system cannot suffer the phenomenon of sudden death because in accordance with Eq. (1.21), $\mathbf{C}(t)$ can either be zero or positive and hence it cannot disappear. In order to have sudden death of entanglement, the second part in the max function of Eq. (1.21) would have to be negative.

The revival of concurrence at later times can significantly be enhanced by adjusting the inter atomic spacing. An example is shown in Fig. 1.8(b), which is for the same parameters as in frame (a) except for the distance between the atoms. It can be seen that at later times, the time evolution of the concurrence does not split up into multiple peaks as in frame (a). Instead, single peaks with higher amplitudes are obtained. In frame (b), the inter atomic spacing is chosen such that some retardation revivals coincide with the main concurrence revivals found in frame (a). In particular, the spacing $x$ is adjusted such that the first revival occurs approximately at $t = (L + x)/c$.

#### 1.4.2.1 Long-time dynamics

In Figs. 1.7 and 1.8 the concurrence is plotted for short times of the evolution, up to only $t = 5L/c$. The results showed that entanglement occurs or is reduced in a periodic fashion, like the pulse periodic excitation, with the magnitude of the subsequent oscillations damped due to the spread of the excitation wave packet. One could expect that the oscillations should collapse after a sufficiently long time and never revive. As we shall see below, this is not the case. Continuing the calculation to much longer times we find that there is an interesting recurrence of the oscillations.

Figure 1.9(a) shows the evolution of the concurrence for the same situation as in Fig. 1.7(a), but extended to much longer times. It can be seen that the damping of concurrence observed in the initial time evolution does not continue. Rather, on a longer time scale, nearly periodic collapse and revival of the concurrence is observed. Throughout the revivals, the concurrence becomes as large as $\mathbf{C}(t) = 0.8$.

The presence of the pronounced long time oscillations is linked not only to the difference between the populations in the symmetric and anti-symmetric atomic states. Rather, it is also due to an additional contribution to the concurrence which comes from $\mathrm{Im}[\rho_{as}(t)]$, see Eq. (1.34). In other words, the coupling of the atoms to the multi mode cavity field leads to a nonzero long-time coherence between the collective states. This is shown in Fig. 1.9(b), where we plot $\mathrm{Im}[\rho_{as}(t)]$ for the same parameters as in frame (a). The coherence is initially zero but beyond $t \sim 10L/c$ starts to build rapidly with the fast

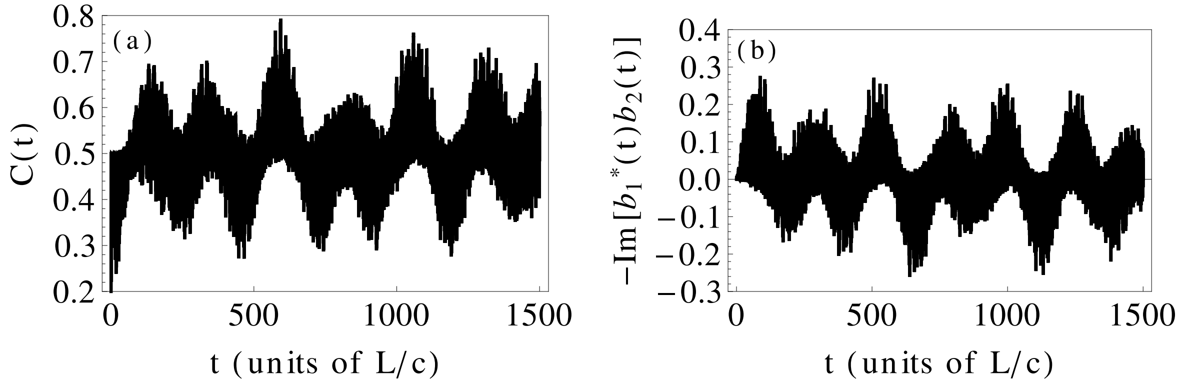

Figure 1.9: The long-time behavior of the concurrence for the same situation as in Fig. 1.7(a). Frame (a) shows the concurrence $\mathbf{C}(t)$, while frame (b) shows the contribution of $\mathrm{Im}[\rho_{as}(t)]$ to the concurrence, as predicted by Eq. (1.34).

oscillations accompanied by a slow modulation.

The origin of the modulation is in the discrete set of Rabi frequencies $g_{\mu j}$ coupling the atoms to the different modes. The Rabi oscillations are not perfectly periodic due to unequal couplings of the atoms to the discrete modes that causes the imperfection of the modulation. The modulated oscillations bear an interesting relation to the Jaynes-Cummings model with a coherent initial state [27]. The graininess of the electromagnetic field results in a discrete set of the Rabi frequencies of the coupled atom-field system that are not perfectly periodic but collapse and revive.

To further analyze the origin of this oscillation, we have calculated the power spectrum of the time signal, which is shown in Fig. 1.10. It can be seen that in particular for lower frequencies, the power spectrum decomposes in a set of near-discrete modes. At larger frequencies, the discrete modes decompose into bands of multiple modes, but the discrete spacing is still visible. This suggest an interpretation of the slow beat-like structure of the long-time dynamics in terms of collapses and revivals, as it is known from the Jaynes-Cummings-model.

The frequencies appearing in the power spectrum can be traced back to the effective Rabi frequencies occurring in the system of two atoms coupled to many cavity modes. To verify this interpretation, we calculated the time evolution of the atoms analytically in certain limiting cases. The simplest example is the Jaynes-Cummings model [27], in which a single atom interacts with a single mode field. Then, the population oscillates at the Rabi frequency $\Omega_0$ of the resonant mode which results in a single peak at this frequency in the power spectrum. Similarly, we analyzed the case of two atoms coupling to a single mode, and to two modes. When two atoms couple to a single mode, the oscillation frequency of the population inversion is $\Omega_{n0}/\sqrt{2}$, as assured by the analytical calculation. If both atoms couple to two modes, $|b_1(t)|^2 = \cos^4(\Omega_{n0}t)$ while $|b_2(t)|^2 = \sin^4(\Omega_{n0}t)$. Thus peak in the Fourier transform of the atomic populations occurs at $\Omega_{n0}$ whereas the cavity population oscillates twice as fast as the atomic population because

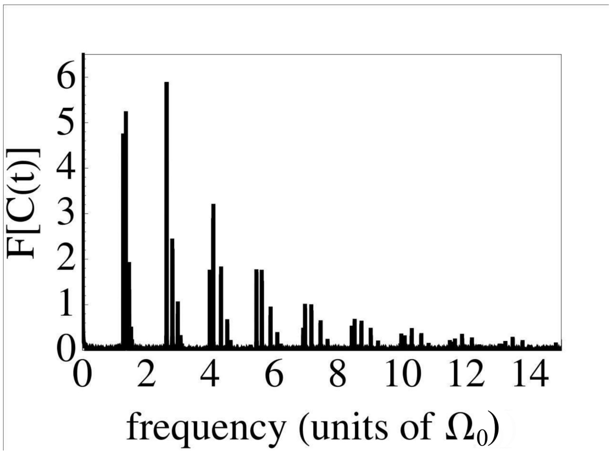

Figure 1.10: The Fourier transform of $\mathbf{C}(t)$ shown in Fig. 1.9(a).

$|b_\mu(t)|^2 = (1/4)\sin^2(2\Omega_{n0}t)$. However, in the general case of two atoms coupling to many modes, the analytical calculations become cumbersome and the identification of all the peaks is a complicated task.

We have found out by the inverse Fourier transformation technique that only first few peaks of the frequency domain signal are enough to produce approximately the time varying signal. This is to be expected since the low-frequency peaks have much higher amplitudes than the others, see Fig. 1.10.

#### 1.4.2.2 Time-averaged concurrence

We have seen that the retardation effects show up clearly as the sharp kinks in the concurrence. As seen in Fig. 1.9(a), revivals of concurrence appear periodically at long times, with large maximum values of concurrence. But because of the presence of fast oscillations, it is not clear whether the enhancement of the entanglement could be observed in practice. Detectors typically respond over a finite time that could be longer than the oscillation periods of the concurrence. Therefore, we consider the mean concurrence $\langle\mathbf{C}(t)\rangle$ averaged over a detection time. As we shall see, the mean concurrence is instructive because it shows how the detected entanglement could be sensitive to the separation between the atoms. We consider both long-range and sub-wavelength separations.

The mean concurrence $\langle\mathbf{C}(t)\rangle$, averaged over a time interval $0 \leq t \leq 800L/c$, is shown in Fig. 1.11. Frame (a) illustrates $\langle\mathbf{C}(t)\rangle$ at large inter atomic spacings, $x \gg \lambda_a$, with $x$ chosen as integer multiples of $\lambda_a$. Complementarily, frame (b) shows the variation of $\langle\mathbf{C}(t)\rangle$ at sub-wavelength spacings with $x$ varying within a half of the wavelength, $x \leq \lambda_a/2$. We observe in both cases that the magnitude of $\langle\mathbf{C}(t)\rangle$ is smaller than 1/2 with the maximum $\langle\mathbf{C}(t)\rangle = 1/2$ for $x$ at $(0, L)$ for large separations, and at $(0, \lambda_a/2)$ for the sub-wavelength separations. Note that the mean concurrence is symmetric with respect to the mid point between the maxima. For the case shown in frame (a) it corresponds to $x = L/2$, whereas for the case (b) it corresponds to $x = \lambda_a/4$. The behavior of the

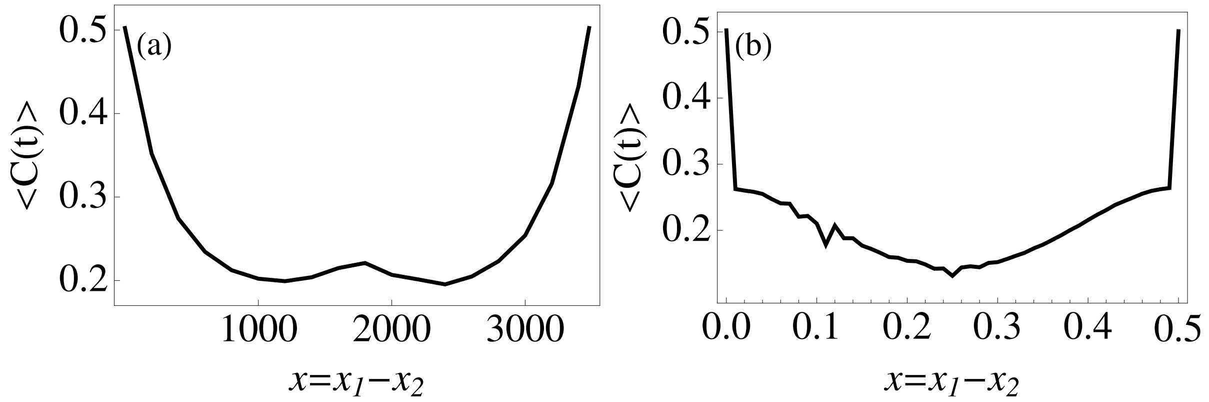

Figure 1.11: The concurrence averaged over time with respect to the inter atomic separation is shown for the same parameters as in Fig. 1.3. In frame (a) $x$ varies in large steps, while in frame (b) $x$ varies within a half of the wavelength.

mean concurrence has a simple explanation. For the separations corresponding to the maxima of the concurrence, the different cavity modes couple to the atoms with the same phases resulting in the same values for the concurrence. For other separations, the atoms experience different phases of the cavity modes relative to the resonant mode, such that the concurrence on average decreases. For the case shown in frame (a), near one-third of the cavity length, the phase difference among different modes starts decreasing. As a consequence, the curve goes up till the half of the length of the cavity is reached where a symmetry point exists in the sense that the phases of all the even modes match and so do the phases of the odd modes but are completely out of phase from each other.

We may conclude, that the retardation effects make the concurrence sensitive to the inter atomic spacing not only at large but also at sub-wavelength spacings.

### 1.4.3 Effects of retardation on entanglement - double excitation case

We now turn to the discussion of the effects of retardation on the entanglement dynamics when two excitations are present in the system. We show how the well known phenomena resulting from the threshold effects in the concurrence Eq. (1.25), such as sudden death, sudden birth and revival of entanglement, can be related to retardation. We will demonstrate that retardation can induce, suppress, or strongly modify these sudden phenomena. To clearly establish the effect of retardation on the sudden phenomena, we concentrate on properties of the quantity $\mathcal{C}_1(t)$, defined in Eq. (1.26), rather than on $\mathcal{C}(t)$. Simply speaking, the quantity $\mathcal{C}_1(t)$ can be positive as well as negative which will allow us to distinguish between the sudden phenomena and sudden changes in the evolution due to the retardation that could occur in time periods where the atoms are separable. The concurrence $\mathcal{C}(t) = \mathcal{C}_1(t)$ for $\mathcal{C}_1(t) \geq 0$.

We illustrate the role of retardation by examining the time evolution of the system for

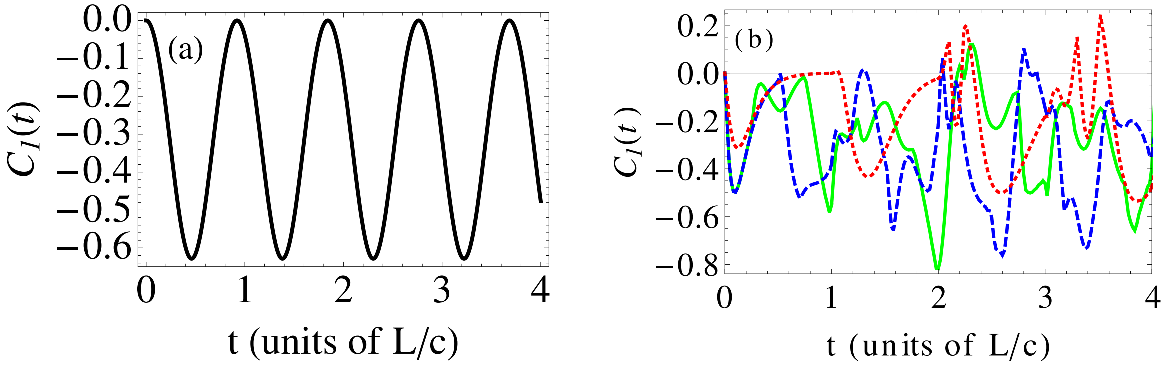

Figure 1.12: (Color online) Time evolution of $\mathcal{C}_1(t)$ for the initial state $|\tilde{\psi}(0)\rangle_1 = |e_1e_2\{0\}_\mu\rangle$, $L = 3.48 \times 10^3\lambda_a$ and $\omega_a = 1.11 \times 10^4\Omega_0$. In frame (a) $N = 1$ and in (b) $N = 45$. The dotted red, solid green and dashed blue curves are atomic separations $x = 0$, $x = L/4$ and $x = L/2$, respectively.

two sets of initial states for which the sudden phenomena are known to not occur in the absence of retardation. Later, we consider an initial state where even in the absence of retardation, sudden phenomena are present.

Consider first an initial state

$$|\tilde{\psi}(0)\rangle = |e_1\rangle \otimes |e_2\rangle \otimes |\{0\}_\mu\rangle \equiv |e_1e_2\{0\}_\mu\rangle, \tag{1.35}$$

in which both atoms are excited and the cavity is empty. Figure 1.12(a) shows the time evolution of $\mathcal{C}_1(t)$ when the atoms are coupled to only a single mode ($N = 1$) of the cavity field. In this case no retardation is present. We see that independent of the distance between the atoms, $\mathcal{C}_1(t)$ oscillates sinusoidally in time and is always negative. This indicates that no entanglement is present at any time. This is also confirmed by the analytical calculation,

$$\begin{aligned}\mathcal{C}_1(t) =& \frac{2}{9}\left(3 - 4\sqrt{2} + (3 - 2\sqrt{2})\cos(2\sqrt{3}\Omega_{n0}t)\right)\sin^2(\sqrt{3}\Omega_{n0}t)\\ =& -0.222\left(2.656 - 0.171\cos(2\sqrt{3}\Omega_{n0}t)\right)\sin^2(\sqrt{3}\Omega_{n0}t).\end{aligned} \tag{1.36}$$

From the above equation, it is clear that $\mathcal{C}_1(t) \leq 0$ if the atoms interact with the central resonant cavity mode only.

Figure 1.12(b) shows the corresponding behavior of $\mathcal{C}_1(t)$ for a large number of the cavity modes ($N = 45$) to which the atoms are coupled. In this case the retardation effects occur. It is apparent that the evolution of $\mathcal{C}_1(t)$ is profoundly affected by the presence of retardation. The most interesting aspect of the retardation is the occurrence of the sudden phenomena that lead to an entanglement at some discrete periods of time. The degree of the created entanglement depends on the distance between the atoms.

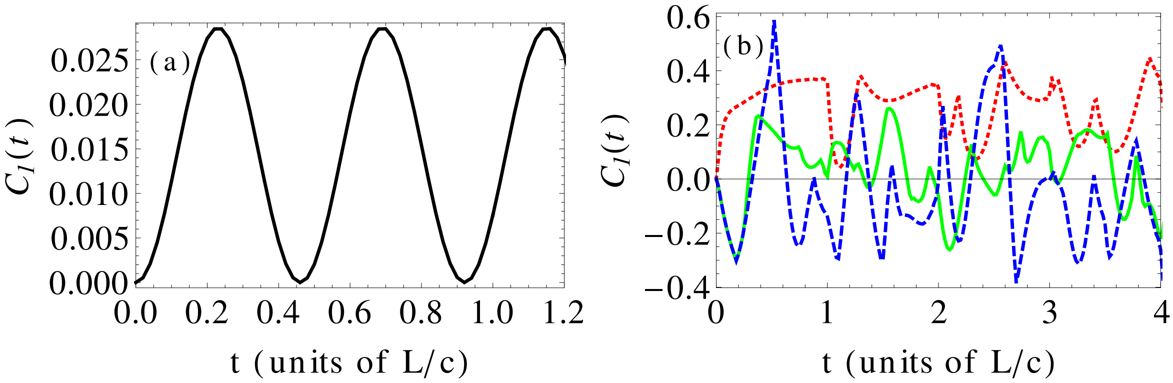

Figure 1.13: (Color online) Time evolution of $\mathcal{C}_1(t)$ for initial condition Eq. (1.40) and the same parameters as in Fig. 1.12. In frame (a) $N = 1$ and in (b) $N = 45$. The dotted red, solid green and dashed blue curves correspond to $x = 0$, $x = L/4$ and $x = L/2$, respectively.

We have observed also for a number of other initial states the similar behavior, that is, there is no entanglement if the atoms couple to a single resonant mode of the cavity electromagnetic field but entanglement is suddenly born, it suddenly dies and revives in the presence of retardation. Examples include $|\tilde{\psi}(0)\rangle = |\{1\}_{0r}\{1\}_{0l}\rangle \otimes |g_1 g_2\rangle$, that is, none of the atoms is in the excited state and the two photons are in the same (resonant) mode but propagate in opposite directions. We assure that $\mathcal{C}(t) = 0$ by performing the analytical calculation for a single mode case.

$$\mathcal{C}_1(t) = \frac{1}{9}\Big( - 4\nu \sin^2(\sqrt{3}\Omega_{n0}t) + 3\sin^2(2\sqrt{3}\Omega_{n0}t)\Big), \tag{1.37}$$

where

$$\nu = \sqrt{6 + 2\cos(2\sqrt{3}\Omega_{n0}t) + \cos(4\sqrt{3}\Omega_{n0}t)} > 0. \tag{1.38}$$

After some algebraic manipulation, Eq. (1.37) can be written as

$$\mathcal{C}_1(t) = \frac{1}{9}\big(1 - \cos(2\sqrt{3}\Omega_{n0}t)\big)\big( - 2\nu + 3(1 + \cos(2\sqrt{3}\Omega_{n0}t))\big). \tag{1.39}$$

It is not difficult to see that $\mathcal{C}_1(t) \leq 0$ and thus $\mathcal{C}(t) = 0$.

Another example of such initial states is $|\tilde{\psi}(0)\rangle = (1/\sqrt{2})\,(|\{0\}_{0r}\{2\}_{0l}\rangle + |\{2\}_{0r}\{0\}_{0l}\rangle) \otimes |g_1 g_2\rangle$, i.e., the atoms are in the ground state, and two photons propagate in the same direction either to the left or to the right in the central cavity mode with equal probability. The analytical expressions for concurrence are easy to derive in the single mode case. Therefore, we do not mention them in every case.

Consider now an initial state

$$|\tilde{\psi}(0)\rangle = \frac{1}{\sqrt{2}}\,(|\{0\}_{0r}\{1\}_{0l}\rangle + |\{1\}_{0r}\{0\}_{0l}\rangle) \otimes |e_1 g_2\rangle, \tag{1.40}$$

in which atom 1 is in excited state, atom 2 is in ground state and the cavity central counter-propagating modes $\omega_{0r}, \omega_{0l}$ are excited into a coherent superposition of the single-quantum states.

In Fig. 1.13(a) we show the time evolution of $\mathcal{C}_1(t)$ for the initial state Eq. (1.40) when the atoms are coupled to the central counter-propagating modes. It is seen that $\mathcal{C}_1(t)$ oscillates sinusoidally in time and is non-negative at all times. Once again we notice that no sudden phenomena occur when the atoms are coupled to the central counter-propagating modes. However, contrary to the initial state Eq. (1.35), the atoms are entangled even when they were initially in a separable state. A naive interpretation for the occurrence of entanglement is that the atoms periodically exchange the excitation through the cavity modes.

The situation becomes different when the atoms couple to a large number of cavity modes. In this case, shown in Fig. 1.13(b), the retardation effects occur and the behavior of $\mathcal{C}_1(t)$ is seen to be qualitatively different from the previous case. These curves are non-sinusoidal, change sharply in non-periodic way such that $\mathcal{C}_1(t)$ can become negative at some discrete periods of time. Thus, $\mathcal{C}_1(t)$ clearly exhibits the phenomena of sudden death, sudden birth and revival. Again, the degree of concurrence as well as the qualitative dynamics is affected strongly by the inter atomic separation. For example, depending on the distance, atomic entanglement immediately builds up ($d\mathcal{C}_1(0)/dt > 0$), or only at a later time via SBE ($d\mathcal{C}_1(0)/dt < 0$). Interestingly, we find in Fig. 1.13(b) that for negligible separation between the atoms, the concurrence exhibits no death in the presence of retardation, and even persists without intermediate points of zero entanglement in contrast to the non-retarded case. Furthermore, at the separation $x = L/2$, the degree of entanglement is more than one order of magnitude larger than that found in the non-retarded case.

It is interesting to note that the degree of entanglement increases with an increasing separation between the atoms. Again, qualitatively similar behavior is also found for other initial states, such as $(|e_1 g_2\{1\}_{0l}\rangle + |g_1 e_2\{1\}_{0r}\rangle)/\sqrt{2}$, in which both the atom and the cavity are entangled.

Lastly, we analyze initial states which lead to periodic death and revival of entanglement even without retardation. For this, we consider the separable initial state

$$|\tilde{\psi}(0)\rangle = |g_1\rangle \otimes |g_2\rangle \otimes |\{2\}_{0r}\rangle \equiv |g_1 g_2\{2\}_{0r}\rangle, \tag{1.41}$$

in which both atoms are in the ground state, and two photons propagate in the same direction in the central cavity mode. The entanglement dynamics without retardation is shown in Fig. 1.14(a). It can be seen that starting from zero concurrence, entanglement builds up, but then vanishes again. This rebirth and death then repeats periodically. The analytical expression for $\mathcal{C}_1(t)$ in this case is given by

$$\begin{aligned}\mathcal{C}_1(t) =& \frac{1}{36}\Bigg(12 - 9\cos(4\Lambda) - 3\cos(4\sqrt{3}\Lambda)) - 4\times \\ & \sqrt{42 + 18\cos(4\Lambda) + 8\cos(2\sqrt{3}\Lambda) + 4\cos(4\sqrt{3}\Lambda)}\sin^2(\sqrt{3}\Lambda)\Bigg),\end{aligned} \tag{1.42}$$

where $\Lambda = \Omega_{n0}t$. The zeros in the above equation mark the times of sudden death of

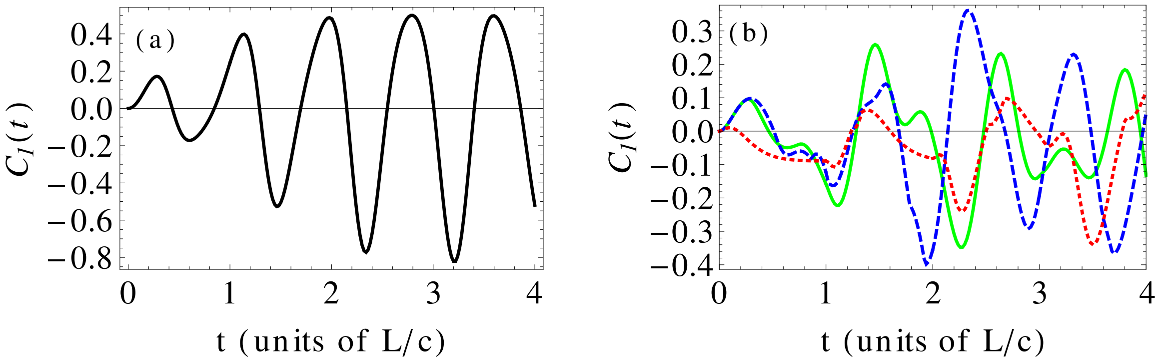

Figure 1.14: (Color online) Time evolution of $\mathcal{C}_1(t)$ for the initial state Eq. (1.41) and the same parameters as in Fig. 1.12. In frame (a) $N = 1$ and in (b) $N = 45$. The dotted red, solid green and dashed blue curves correspond to $x = 0$, $x = L/4$ and $x = L/2$, respectively.

entanglement. However, since there is no retardation, the inter atomic spacing does not affect the dynamics.

The corresponding results with retardation are shown in Fig. 1.14(b). In this case, while the exact temporal dynamics and the magnitude of concurrence is again affected by the inter-particle separation, the qualitative dynamics manifesting itself in the periodic death and birth of entanglement is independent of the retardation effects. In this particular example, as the distance between the atoms increases, so does the maximum entanglement between them as has been observed for $t \leq 4L/c$.

Qualitatively similar results again are also observed for other initial states, such as $|\tilde{\psi}(0)\rangle = \sqrt{p}|e_1e_2\{0\}_\mu\rangle + \sqrt{1-p}|e_1g_2\{1\}_{0l}\rangle$, which we analyzed for $p \in \{1/10, 2/10, 3/10, 4/10\}$. Also the initial state $|\tilde{\psi}(0)\rangle = (|e_1g_2\rangle + |g_1e_2\rangle)|\{1\}_{0l}\rangle/\sqrt{2}$ with maximum entanglement between the atoms behaves qualitatively similar.

We can gain a qualitative understanding of the behavior of $\mathcal{C}_1(t)$ in the presence of retardation by making use of Eq. (1.30) for the collective states of the system and expressing $\mathcal{C}_1(t)$ in terms of the probability amplitudes $b_{\alpha s}(t)$ and $b_{\alpha a}(t)$ as

$$\mathcal{C}_1(t) = \sum_\alpha \left||b_{\alpha s}(t)|^2 - |b_{\alpha a}(t)|^2 - 2\mathrm{Im}\left[b^*_{\alpha s}(t)b_{\alpha a}(t)\right]\right| - |b(t)|\sqrt{\sum_{\alpha>\beta}|b_{\alpha,\beta}(t)|^2 + \sum_\alpha |b_{\alpha,\alpha}(t)|^2}, \tag{1.43}$$

where

$$\begin{aligned} b_{\alpha s}(t) &= \frac{1}{\sqrt{2}}\left[b_{\alpha 1}(t) + b_{\alpha 2}(t)\right], \\ b_{\alpha a}(t) &= \frac{1}{\sqrt{2}}\left[b_{\alpha 1}(t) - b_{\alpha 2}(t)\right], \end{aligned} \tag{1.44}$$

are the probability amplitudes of the states $|s\rangle \otimes |\{1\}_\alpha\rangle$ and $|a\rangle \otimes |\{1\}_\alpha\rangle$, respectively.

The first line of the right-hand-side of Eq. (1.43) is associated with the one-photon coherence determined by both, unequal populations of the collective states and the coherence between them, whereas the second line is attributable to the two-photon populations of either the atomic system, determined by $b(t)$, or the cavity modes, determined by $b_{\alpha,\beta}(t)$ and $b_{\alpha,\alpha}(t)$. Thus, the mechanism for entanglement with two excitations initially present in the atomic system is similar to that of the single excitation case. Entanglement between the atoms, $\mathcal{C}_1(t) > 0$, can be traced back to the single-excitation sub-space, and in particular imbalances between the symmetric and the anti-symmetric singly-excited atom states. However, in contrast to the single excitation case, this asymmetry must exceed the threshold set by the contribution from the systems with both excitations either in the atoms or in the cavity.

The entanglement seen in Figs. 1.12(b), 1.13(b) and 1.14(b) indicates that the retardation effects lead to a non-zero population difference between the symmetric and antisymmetric states that at some periods of time overcomes the threshold factor in the expression for $\mathcal{C}_1(t)$. What this means is that the time evolution of the atoms is not linked to the total cavity population. In particular, if one excitation is in the cavity, the other excitation can be in different atomic states with varying population imbalance between symmetric and anti-symmetric states.

#### 1.4.3.1 Long-time and time-averaged dynamics

The above investigations have shown that the presence of the retardation effects leads to a non-sinusoidal evolution of the concurrence which results in the phenomena of sudden death and sudden birth of entanglement. One can notice from Figs. 1.12(b), 1.13(b) and 1.14(b) that there are finite periods of time at which $\mathcal{C}_1(t)$ is negative. These are dead zones of entanglement or equivalently at these times the atoms are separable. The following question then arises: In which states, entangled or separable, do the atoms spend most of the time? To answer this question, we first extend the calculations of $\mathcal{C}_1(t)$ to long times and then average $\mathcal{C}_1(t)$ over a long evolution time. We concentrate on the case illustrated in Fig. 1.13(b).

The corresponding long-time dynamics of $\mathcal{C}_1(t)$ is shown in Fig. 1.15(a). It is seen that the time evolution of $\mathcal{C}_1(t)$ is very spiking with the amplitude of the fast oscillations slowly modulated in time. It can also be noticed that the amplitude of $\mathcal{C}_1(t)$ oscillates around $\mathcal{C}_1(t) = 0$ which suggests that over a long period $\mathcal{C}_1(t)$ might average to zero or negative values. Therefore, we calculate the mean value of $\mathcal{C}_1(t)$ by averaging over the evolution time $0 \leq t \leq 2000L/c$ for different inter atomic distances around a distance of half the cavity length, in an interval of half a wavelength $\lambda_a$. As expected, we find that depending on the inter-atomic separation the mean value of $\mathcal{C}_1(t)$ can be positive or negative. Next, we average the more important concurrence $\mathcal{C}(t)$ itself in the same way. The result is shown in Fig. 1.15(b). The first atom is located at $x_1 = \lambda_a$, and the second atom is located close to $1740\lambda_a$ such that they are separated roughly by half of the cavity length. It is seen that the precise positioning of the atoms within a wavelength at such large distances plays a vital role in the entanglement between the atoms. The effect of going away from the $x = L/2$ position is clearly to decrease the amount of entanglement. But

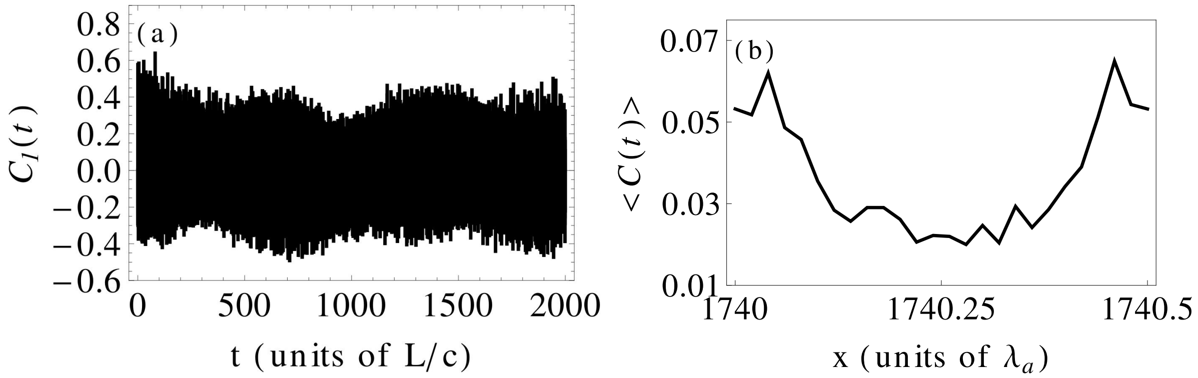

Figure 1.15: (a) The long time behavior of $\mathcal{C}_1(t)$ is shown for $L = 3.48 \times 10^3 \lambda_a, \omega_a = 1.11 \times 10^4 \Omega_0, N = 45, x = L/2$ and the initial state $|\tilde{\psi}(0)\rangle = (|e_1 g_2 \{1\}_{0l}\rangle + |e_1 g_2 \{1\}_{0r}\rangle)/\sqrt{2}$. (b) The concurrence averaged over a long evolution time is shown as a function of the inter atomic spacing $x$. The distance $x$ varies around half of the cavity length, over an interval of one half of the cavity wavelength.

as expected, the concurrence is positive for all distances even in an average sense, due to the non-negative nature of $\mathcal{C}(t)$.

## 1.5 Ring cavity as a Gyroscope

We have also investigated if the current setup that we have can be used to observe the Sagnac effect [118]. By rotating our ring cavity from the centre of gravity, the distances covered by clockwise and counterclockwise modes for one round trip will be different. This difference in the path lengths can be used to measure shifts in the frequency as in a gyroscope. We did some preliminary calculations for that purpose. Suppose, the rotation is given in the clockwise direction, then the time taken by the mode going to left or the counterclockwise mode for a complete trip is given by

$$t_l = \frac{L - r\omega_{rot} t_l}{c}, \tag{1.45}$$

where $r$ is the perpendicular distance from the center of gravity of the resonator to its wall. For arbitrary cavity geometry, this distance can be calculated by $r = 2A/p$, where $A$ is the enclosed area by the path of the light and $p$ is the perimeter of the light path. For an equialteral triangle having sides equal to $L/3$ as we have, $A = L^2/(12\sqrt{3})$ and $p = L$, which gives $r = L/(6\sqrt{3})$.

Eq. (1.45) implies that

$$t_l = \frac{L}{c + r\omega_{rot}}. \tag{1.46}$$

The co-propagating mode, on the other hand travels a distance larger than the length of the cavity for one round trip. Thus

$$t_r = \frac{L + r\omega_{rot} t_l}{c} = \frac{L}{c - r\omega_{rot}}. \tag{1.47}$$

The time difference between the oppositely traveling modes is given by

$$\Delta t = t_r - t_l = \frac{2Lr\omega_{rot}}{c^2 - r^2\omega_{rot}^2}. \tag{1.48}$$

Note that

$$r^2\omega_{rot}^2 << c^2. \tag{1.49}$$

Therefore

$$\Delta t \approx \frac{2Lr\omega_{rot}}{c^2}. \tag{1.50}$$

The round trip optical path length difference can be written as

$$\Delta L = c\Delta t = \frac{2Lr\omega_{rot}}{c}. \tag{1.51}$$

From the above equation, we see that the optical path difference is directly proportional to the rotation rate of the cavity. Now resonance condition insists that for an integer $m$,

$$m\lambda_l = L_l, \quad m\lambda_r = L_r, \tag{1.52}$$

so the mode frequencies for the right and left propagating modes can be written as

$$\omega_{\mu i} = \frac{2\pi\mu c}{L_i}, \quad i \in \{l, r\}. \tag{1.53}$$

Now the frequency shift $\Delta\omega$ is given by

$$\Delta\omega = \omega_l - \omega_r = 2\pi\mu c \frac{L_r - L_l}{L_r l_l} = \frac{\omega \Delta L}{L}, \tag{1.54}$$

since $L_r L_l \approx L^2$. This implies that

$$\frac{\Delta\omega}{\omega} \approx \frac{\Delta L}{L}. \tag{1.55}$$

The length of the cavity that we have assumed in our calculations is $3480\lambda_a$. In optical regimes, which we are interested in, this corresponds to large frequency shifts. The efficiency of a gyroscope, however, lies in detecting very small frequency shifts. Nevertheless, one can find suitable parameters under which the present set up can be used to detect small shifts in the frequency.

## 1.6 Summary

We have studied the effects of retardation on the entanglement properties of two atoms located inside a multi-mode ring cavity. Retardation effects become pronounced if the mode spacing of the cavity is small enough such that the atoms can simultaneously couple to many modes of the cavity field. The Schrödinger equation for the wave function of the system was solved for different atomic separations and initial conditions with single and double excitations present in the system. It was shown that the retardation effects are manifest not only in the dynamics of the atomic population but also in the dynamics of entanglement between the atoms. Characterizing entanglement between the atoms by the concurrence, we have found that the retardation leads to abrupt kinks in the concurrence at intervals corresponding to the flight time of a photon between the atoms or to the time corresponding to a round trip in the cavity.

Furthermore, we demonstrated that the retardation effects crucially depend on the atom separation both, on the multi- and sub-wavelength distance scale. We have also distinguished significantly different short-time and long-time retardation effects in the evolution of the concurrence. In particular, at short times the concurrence exhibits periodic sudden changes from separable to highly entangled states. At long times, the retardation gives rise to periodic beats in the concurrence that resemble the phenomenon of collapses and revivals in the Jaynes-Cummings model. We finally identified parameter values and initial conditions at which retardation qualitatively changes the entanglement dynamics. In particular, the atoms can remain either separable or entangled throughout the whole time evolution without retardation, whereas they exhibit the phenomena of sudden birth and sudden death of entanglement when the retardation is included.

Lastly, we found that our model system could be used as a gyroscope but due to the size of the ring cavity, it can only be used to measure very large frequency shifts since optical wavelengths are assumed.

## 1.7 Outlook

- We discover that all the effects we have observed strongly depend on the accurate placement of the atoms inside the cavity. Controlling the motion of the atom may not be easily achieved in an experiment. An interesting investigation can be done if the positions of the atoms are not fixed to one point but they are allowed to move within some small spatial domain, for example, inside a harmonic trap.
- Throughout our analysis, we assumed the cavity field to be in a number state. It will be interesting to describe the cavity field by a coherent state because then the two photon coherence $\rho_{14}$ will survive. Both criteria given in Eq. (1.20) for the calculation of concurrence will compete. We expect interesting effects by the replacement of a quantum state by a classical counterpart.
- Introducing a slight detuning between the cavity central mode and the Bohr atomic transition frequency can also be studied.

- The asymmetry in the long-time behavior of concurrence for single and double excitation case, Figs. (1.9a) and (1.15a), repectively can be investigated. Like in the single excitation case, Fourier transformation to identify the frequencies of the different interacting modes may be used to achieve the purpose.
- The parameters can be optimized in order to use the current set up as a ring gyroscope.

# Chapter 2

# Numerical optical centroid measurements

The main results of this chapter have been submitted to Phys. Rev. A:
**Q. Gulfam**, and J. Evers
*Numerical optical centroid measurements*
(`arXiv:1301.0774 [quant-ph]`)

*Optical imaging methods are typically restricted to a resolution of order of the probing light wavelength $\lambda_p$ by the Rayleigh diffraction limit. This limit can be circumvented by making use of correlated $N$-photon states, having an effective wavelength $\lambda_p/N$. But the required $N$-photon detection usually renders these schemes unfeasible. In [54], an imaging scheme, referred to as optical centroid measurements (OCM) is proposed that replaces the multi-photon detectors by an array of single-photon detectors. It has been predicted in [54] that using a post-processing of the measured data, the resolution scaling of $\lambda_p/N$ can be achieved for certain states of light. We extend the approach to a broader class of input states, find optimum detection strategies, and quantitatively study the approach. For this, complementary to the existing approximate analytical results, we explore the approach using "experimental" data obtained from numerical experiments by sampling detection events from the initial state wave function. We analyze the resolution in dependence on the detector size to find optimum parameters for an experimental implementation. We also find indications that the scheme might work for a broader class of states than predicted based on the analytical estimates.*

## 2.1 Introduction

Conventional optical lithography schemes are always impeded by the Rayleigh diffraction limit [119, 120] owing to the wave nature of light. Due to the continuous and everincreasing demand of faster devices in microelectronics, ever-smaller structures in semiconductors need to be written. Several mechanisms have been established to beat this classical limit. Various techniques employ classical fields. The correlation of wave vector and frequency in a narrow band has been utilized in [121, 122] while in [123, 124] the $N$ photon absorption medium is simulated by $N$th harmonic generation. On the other hand, non-classical effects to surpass the diffraction limit are also greatly explored. In [125], an exposure arrangement based on the use of multiplicity of two photon excitation frequencies is introduced to obtain two fold resolution enhancement. [126] made use of four mode reciprocal binomial states. Later, [45] presented the first proposal of quantum lithography (QL), an optical interferometric scheme using entangled photon number states. Soon after the theoretical proposal, [127] performed the first proof-of-principle QL experiment involving two photons and demonstrated the improvement in the classical diffraction limit by a factor of 2.

Since the diffraction limit [119, 120] is on the order of the wavelength of the incident light, ever-shorter wavelengths are desirable. The drawback of using extremely energetic photons in lithographic schemes is not only that they may damage the material that absorbs them but also that these techniques demand costly optical imaging systems. Entangled states of light overcome the multi photon absorption hindrances because of the reduced effective wavelength. $N$ entangled photons offer an $N$ times improvement in the resolution. Thus non-classical states of light have paved their way to quantum lithography [45, 126] by offering extremely small wavelengths.

For regular sources of light such as lasers operating at coherent light fields, $N$ photon absorption provides with the standard quantum limit in resolution, which goes as $\lambda_p/(2\sqrt{N})$. This limit improves the Rayleigh diffraction limit [119] by a factor of $\sqrt{N}$. This standard quantum limit, however, is not ultimate and can be surpassed by using quantum light which possesses special non-classical characteristics of entanglement. The ultimate quantum limit also known as the Heisenberg limit scales as $\lambda_p/(2N)$ for $N$ entangled photons [128–131].

Still the availability of efficient multi photon resists that are in addition required to be able to resolve the photon number is a technical limitation [62, 132]. Moreover, the count rate associated with multi photon absorption is also low [62].

The detection of entangled photons is done in a far efficient manner using the technique proposed in [54] based on optical centroid method (OCM) as no multi photon detection is needed. Both methods, that is, QL and OCM succeed in enhancing the resolution $N$ folds, however, the efficiency of OCM is shown to be fundamentally higher than that of the former [54]. Novel schemes that do not require multi photon absorption also include [133, 134]. [133] is a lithography proposal relying on a system prepared in a position-dependent dark state, however, multi beams and multi lambda systems are needed. [134] utilizes multiple Rabi oscillations between two atomic levels so no entanglement is necessary. Nevertheless, it requires non-linear atom-field interaction. On the other hand, the scheme [54] needs only to measure the intensity of non-classical light and later a numerical post processing of the image. An array of single photo detectors detects the incoming photons. Afterwards, centroid of these detected photon positions is calculated.

The measurement procedures are to be repeated several times since a distribution of the centroid is involved. Recently, the first proof-of-principle experiment of OCM for two photon entangled state has been carried out by [61, 135]. The experiment used two kinds of detectors: One is a pair of single photon detectors for OCM while the other is two-photon absorption detector for QL. The experiment verified that OCM achieved the same quantum superresolution as QL but much more efficiently.

We apply the scheme numerically to several non-classical states of light. Our numerical study encompasses input states mentioned already in [54] and also considers new kind of states that are helpful in resolution enhancement by OCM. We generate random numbers as positions of photons from the position space non-classical wave function. Afterwards, we calculate the centroid of the discrete data as a result of employing a model detection system. Utilizing the numerical centroid coordinates, we try to recover the probability distributions along the centroid axis corresponding to all these states.

We characterize the error in the recovery of the theoretical centroid distribution by root mean square deviation. We find straight-forward interpretation for the results of rms deviation as a function of the size of the detector for the case of fixed detector positions from the incident wave function. Later, we give reasons why a fixed detector array cannot recover the complete probability distribution along the centroid axis. Another more sophisticated detection method is employed which either utilizes detector arrays composed of very small sized detectors or the detector positions require to be shifted many times, as done in [61, 135]. The results show that only small sized detectors can serve as good detectors, as expected. Via our quantitative investigations, we could discover the effect of statistically unstable outcome at very small detector sizes. The resolution enhancement with an increase in the number of photons in the impinging wave function was verified. An in-depth inspection of multi photon absorption is performed not only as a function of the detector size but also as a function of the number of photons in the initial states for different parameter regimes.

The chapter is organized as follows. In Sec. (2.2), we review in brief the basic equations in the configuration space presented in [54], introduce the various non-classical input states and discuss in detail the important technical issues which come up as the centroid scheme is implemented numerically to non-classical states, the discretization of the numerical data by a model detection system and an estimation of the error between the numerical result and the theoretical distribution. In Sec. (2.3), we explain the results for different types of non-classical input states as well as the various analysis procedures thoroughly. The article is summarized in Sec. (2.4) and a brief outlook is given in Sec. (2.5).

## 2.2 Theoretical considerations

### 2.2.1 Centroid method

We briefly review the formalism of resolution enhancement developed in [54, 62] using quantum lithography and optical centroid measurements. We consider photons of wavelength $\lambda_p$ incident on a detection plane under an angle such that the wavelength associated to the wave vector component in the detection plane is given by $\lambda = \lambda_p/\sin\theta$. In the following, we restrict the analysis to one spatial dimension in the detection plane. Let $\hat{a}(k)(\hat{a}^\dagger(k))$ denote the photon annihilation (creation) operator in this transverse momentum space.

These operators follow the commutation relation

$$[\hat{a}(k), \hat{a}^\dagger(k')] = \delta(k - k') \,. \tag{2.1}$$

An $N$-photon momentum eigenvector can be defined using $\hat{a}^\dagger(k_i)$ as

$$|k_1, k_2, \ldots, k_N\rangle = \frac{1}{\sqrt{N!}}\hat{a}^\dagger(k_1)\hat{a}^\dagger(k_2)\ldots\hat{a}^\dagger(k_N)|0\rangle \,, \tag{2.2}$$

where $|0\rangle$ indicates the state without photons. The momentum space wave function representation of a pure $N$-photon Fock state $|N\rangle$ is given by

$$\phi(k_1, k_2, \ldots, k_N) = \langle k_1, k_2, \ldots, k_N|N\rangle. \tag{2.3}$$

The transverse momenta of the photons are restricted by the Rayleigh diffraction limit [119] such that

$$\phi(k_1, k_2, \ldots, k_N) = 0 \tag{2.4}$$

for any $|k_n| > 2\pi/\lambda$. The spatial annihilation operator is defined as

$$\hat{A}(x) \equiv \frac{1}{\sqrt{2\pi}}\int dk\hat{a}(k)\exp(ikx). \tag{2.5}$$

A corresponding $N$-photon state can be constructed as

$$|x_1, x_2, \ldots, x_N\rangle \equiv \frac{1}{\sqrt{N!}}\hat{A}^\dagger(x_1)\ldots\hat{A}^\dagger(x_N)|0\rangle \,. \tag{2.6}$$

The position space wave function is obtained by taking the $N$-dimensional Fourier transform of $\phi(k_1, k_2, \ldots, k_N)$ and is given by

$$\psi(x_1, x_2, \ldots, x_N) = \langle x_1, x_2, \ldots, x_N|N\rangle. \tag{2.7}$$

Of fundamental importance in the centroid scheme is the transformation of the photon position coordinates $x_i$ to the centroid coordinate $X$ and the relative position coordinates $\xi_n$ which are defined as

$$X \equiv \frac{1}{N}\sum_{n=1}^{N} x_n, \qquad \xi_n \equiv x_n - X. \tag{2.8}$$

Note that when $x_1 = x_2 = \cdots = x_N = x$, $X = x$, that is, if all photons are constrained to arrive at the same point $x$, the relative positions $\xi_n$ become zero and the centroid variable also lies at the same point $x$ according to Eq. (2.8).

Conventional quantum lithography proposals rely on $N$-photon detection at a single detector at position $x$. The input state is a $N$-photon state $\hat{\rho}_N = |N\rangle\langle N|$. The probability density for multi photon absorption is therefore given by

$$\begin{aligned} p_{MP}(x) = \langle : \hat{I}^N(x) : \rangle &= \langle [\hat{A}^\dagger(x)]^N [\hat{A}(x)]^N \rangle \\ &= N|\psi(x, x, \ldots, x)|^2. \end{aligned} \tag{2.9}$$

The centroid method, in contrast, relies on an array of detectors, such that each of the incident $N$ photons is detected by an individual detector. Out of the individual photon detection positions, the centroid position $X$ is calculated. The probability density of the centroid distribution is obtained from

$$\langle : \Pi_{n=1}^N \hat{I}(x_n) : \rangle \tag{2.10}$$

as a marginal probability density by tracing out all relative positions $\xi_n$ using $x_n = X + \xi_n$,

$$\begin{aligned} p_{OCM}(X) &= \int d\xi_1, \ldots, d\xi_{N-1} \langle : \Pi_{n=1}^N \hat{I}(X + \xi_n) : \rangle \\ &= \int d\xi_1, \ldots, d\xi_{N-1} N|\psi(X + \xi_1, X + \xi_2, \ldots, X + \xi_N)|^2. \end{aligned} \tag{2.11}$$

The key result of Tsang's analysis is that the two distributions Eq. (2.11) and Eq. (2.9) have the same spatial dependence and thus resolution. Therefore, the technically challenging $N$-photon detection in a single detector can be replaced by $N$ single-photon detections. A further advantage of the centroid method is that it is potentially much more efficient than multi-photon detection, i.e., for experimentally relevant parameters, $p_{OCM}(X)$ can exceed $p_{MP}(X)$ significantly [54, 61, 62].

### 2.2.2 Trial states

Throughout our analysis, we apply the optical centroid method using numerical experiments to various non-classical photon states, which we introduce in the following.

#### 2.2.2.1 NOON states

Following [62], we consider momentum-correlated $N$-photon NOON states

$$|NOON\rangle = \frac{1}{\sqrt{2}} \left( |N\rangle_A |0\rangle_B + |0\rangle_A |N\rangle_B \right) \tag{2.12}$$

in which the two modes $A$ and $B$ correspond to two wave vector directions for the photons incident on the detection plane, with mean transverse component of the wave vector $k_0$ and $-k_0$, respectively. The momentum spread of the transverse wave vector is denoted by $\Delta k$ with $k_0 \gg \Delta k$. Denoting the (normalized and even) transverse wave vector profile as $f(q)$, the momentum space wave function is

$$\phi_{NOON}(k_1, k_2, \ldots, k_N) = \frac{1}{\sqrt{2\Delta k^N}} \left[ \prod_{n=1}^N f\left( \frac{k_n - k_0}{\Delta k} \right) + \prod_{n=1}^N f\left( -\frac{k_n - k_0}{\Delta k} \right) \right]. \tag{2.13}$$

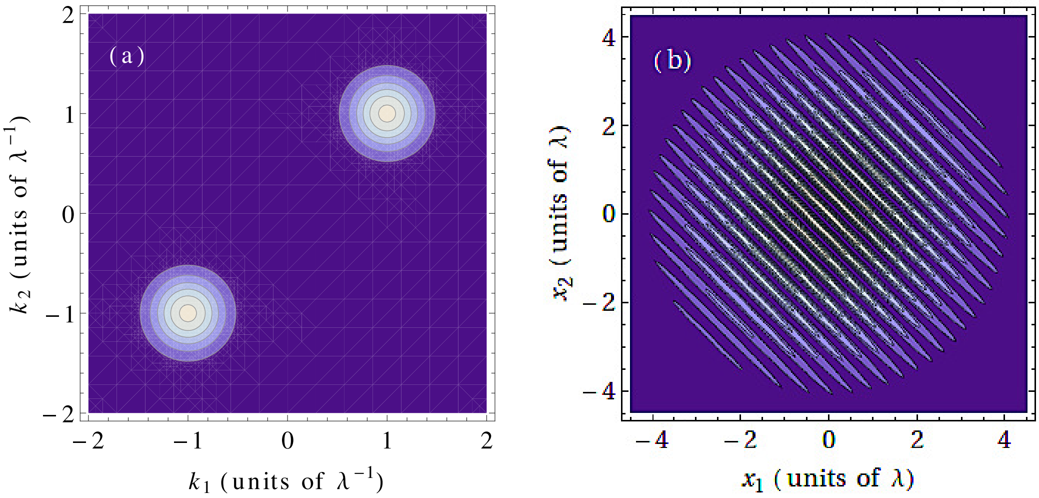

Figure 2.1: (Color online) Momentum (a) and the corresponding position (b) space probability distributions of a two-photon NOON state

By Fourier transform, assuming $f(q) = \pi^{-1/4}e^{-q^2/(2\Delta k^2)}$, we obtain the position space wave function

$$\psi_{NOON}(x_1, x_2, \ldots, x_N) = \frac{\sqrt{2}\,\Delta k^N}{\pi^{N/4}}\, e^{-\frac{1}{2}\Delta k^2\, \sum_{i=1}^{N} x_i^2} \times \cos\left(k_0 \sum_{i=1}^{N} x_i\right) . \tag{2.14}$$

The probability distribution thus follows as

$$|\psi_{NOON}(x_1, x_2, \ldots, x_N)|^2 = 2\left(\frac{\Delta k}{\sqrt{\pi}}\right)^N e^{-\Delta k^2\, \sum_{i=1}^{N} x_i^2} \cos^2\left(k_0 \sum_{i=1}^{N} x_i\right) . \tag{2.15}$$

Note that this expression is only normalized in the limit $\Delta k \ll k_0$, in which the field operators for the two modes $A$ and $B$ satisfy the usual bosonic commutation rules.

For numerical simulations we employ dimensionless position variables $\bar{x} = x/\lambda$ such that the position coordinates are measured in the units of $\lambda$. In terms of the dimensionless variables, Eq. (2.15) becomes

$$2\left(\frac{\Delta k}{\sqrt{\pi}}\right)^N e^{-\frac{4\pi^2}{\sigma^2}\, \sum_{i=1}^{N} \bar{x}_i^2} \cos^2\left(2\pi \sum_{i=1}^{N} \bar{x}_i\right) . \tag{2.16}$$

Using $\lambda = 2\pi/k_0$, we have defined the dimensionless width $\sigma = k_0/\Delta k$. Throughout the numerical analysis, we have chosen $\sigma = 4\sqrt{2}\pi$ such that $\Delta k \ll k_0$ as required.

An example for the position space probability distribution of a two-photon NOON state using dimensionless variables is shown in Fig. (2.1).

2-photon NOON states can be created using spontaneous parametric down conversion combined with the Hong-Ou-Mandel effect [45, 48]. Such NOON states have been employed in proof-of-principle experiments on resolution enhancement [61, 127, 136]. Higher order NOON states with larger $N$ have also been created experimentally [137–142].

#### 2.2.2.2 Jointly Gaussian states

The momentum space representation of a jointly Gaussian state can be written as [62]

$$\phi_{JG}(k_1, k_2, \ldots, k_N) = \sqrt{\frac{C}{N}}\, e^{-\frac{1}{4}\sum_{n,m} k_n B_{nm} k_m}\,, \tag{2.17}$$

with components of the matrix $B$ given by

$$\begin{aligned} B_{nn} &= \frac{1}{N^2 B^2} + \left(1 - \frac{1}{N}\right)\frac{1}{\beta^2}\,, \\ B_{nm} &= \frac{1}{N^2 B^2} - \frac{1}{N\beta^2}, \quad n \neq m\,. \end{aligned} \tag{2.18}$$

$C$ is a normalization constant. $B$ can be interpreted as the width of the average momentum of the photons, whereas $\beta$ characterizes the width in momenta relative to the average [62]. These two parameters determine the variance of $k_n$ given by

$$\langle k_n^2 \rangle = B^2 + (1 - \frac{1}{N})\beta^2. \tag{2.19}$$

The position wave function for the jointly Gaussian state then follows as

$$|\psi_{JG}(x_1, x_2, \ldots, x_N)\rangle \propto \exp(-\sum_{n,m} x_n B^{-1}_{nm} x_m)\,. \tag{2.20}$$

The multi photon absorption pattern $\langle : \hat{I}^N(x) : \rangle$ is a Gaussian with a root mean square width $1/(2NB)$. If $B = \beta/\sqrt{N}$, the distribution becomes classical and the photons are independent. This distribution is a symmetric Gaussian with equal widths along the diagonal axes in the configuration space. The classical multi photon absorption width is given by the standard quantum limit $W_C = 1/(2\sqrt{N\langle k_n^2\rangle})$. Increasing $B$ from the classical value makes the distribution quantum mechanical. The maximum value of $B$, $B = \sqrt{\langle k_n^2 \rangle}$ renders the ultimate quantum limit for the width of the multi photon absorption pattern $W_{\min} = 1/(2N\sqrt{\langle k_n^2\rangle})$.

The quantum mechanical elongated jointly Gaussian has a shorter width along the centroid direction and is stretched along all the other diagonals in the position space.

The position space probability distribution is

$$|\psi_{JG}(x_1, x_2, \ldots, x_N)\rangle|^2 \propto \exp(-2\sum_{n,m} x_n B^{-1}_{nm} x_m)\,. \tag{2.21}$$

Fig. (2.2) shows the position space probability distribution for a quantum mechanical jointly Gaussian state in terms of dimensionless position variables defined in Sec. (2.2.2.1).

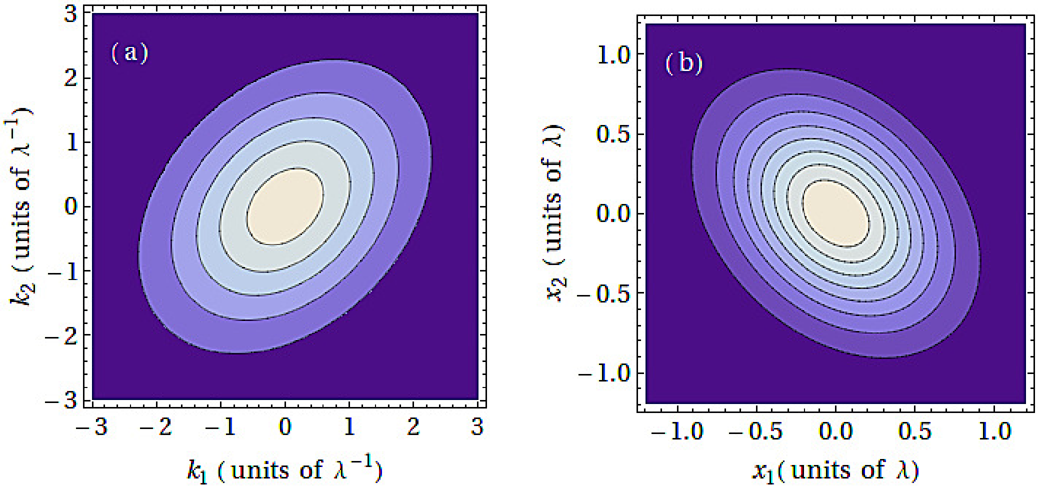

Figure 2.2: (Color online) Momentum (a) and the corresponding position (b) space probability distributions of a joint Gaussian state with $N = 2$ and $B = \beta = \lambda^{-1}$

#### 2.2.2.3 Cat states

The third class of states we investigate are correlated coherent cat states. We in particular analyze two mode states of the form [63]

$$|\psi_{ccc}\rangle = \mathcal{N}(|\alpha\rangle_1|\alpha\rangle_2 + |-\alpha\rangle_1|-\alpha\rangle_2)\,, \tag{2.22}$$

in which $|\alpha\rangle_i$ is a coherent state in mode $i$ with complex parameter $\alpha$, defined by $a_i|\alpha\rangle_i = \alpha|\alpha\rangle_i$, where $a_i$ is the photon annihilation operator of mode $i$. Note that other two mode cat states have also been considered in the literature in different contexts [64, 143, 144]. These states can be seen as an extension of the famous single particle Schrödinger coherent cat states [145] given by $|\alpha_+\rangle \equiv |\alpha\rangle + |-\alpha\rangle$ [146–148]. A proposal for the generation of Schrödinger's cat state has been discussed in [149]. Experiments performed on the optical cat states include [150–152]. $\mathcal{N}$ is a normalization factor which is given by $1/\sqrt{2(1+\exp(-4|\alpha|^2)}$.

While Eq. (2.22) resembles a two-photon NOON state, there is an important difference between the states. The bi photon NOON state consists of exactly two photons. Individual realizations of the same cat state, however, can contain different numbers of photons. The probability $p(n_1, n_2)$ to detect $n_i$ photons in mode $i$ evaluates to

$$\begin{aligned} p(n_1, n_2) &= \langle n_1, n_2|\psi_{ccc}\rangle\langle\psi_{ccc}|n_1, n_2\rangle \\ &= 2\mathcal{N}^2 \frac{e^{-2|\alpha|^2}}{n_1!\, n_2!}|\alpha|^{2(n_1+n_2)}\,[1 + (-1)^{n_1+n_2}]. \end{aligned} \tag{2.23}$$

It follows that the state can only contain even numbers of photons. For a certain range of $|\alpha|$, states with less or equal to two photons are populated with high probability. This motivates the analysis of detection events, in which one photon is detected in each of the two modes. In the following, we will focus on this case.

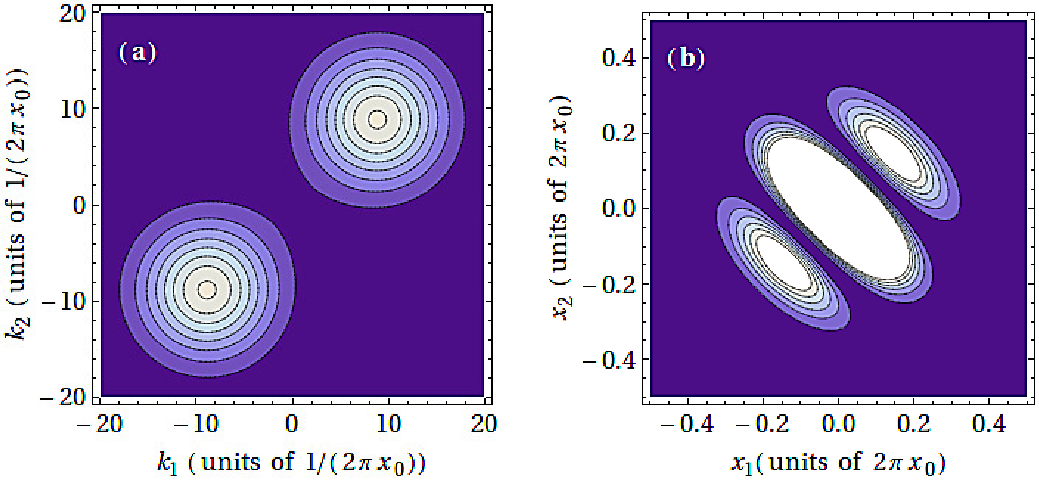

Figure 2.3: (Color online) Momentum (a) and the corresponding position (b) space probability distributions of a correlated cat state with $\alpha = i$

The position representation of a single mode coherent state is [153]

$$\langle x|\alpha\rangle = \frac{1}{\sqrt{x_0\sqrt{\pi}}} e^{-\frac{1}{2}(\alpha^2-|\alpha|^2)} e^{-\frac{1}{2}(x/x_0-\sqrt{2}\alpha)^2} \tag{2.24}$$

with $x_0 = \sqrt{\hbar/(m\omega_0)}$. The position space representation of Eq. (2.22) then follows as

$$\begin{aligned}\psi_{ccc}(x_1,x_2) =&\langle x_1|\alpha\rangle_1\langle x_2|\alpha\rangle_2 + \langle x_1|-\alpha\rangle_1\langle x_2|-\alpha\rangle_2\\ =&\frac{2\mathcal{N}}{\sqrt{\pi}x_0} e^{-\frac{1}{2x_0^2}(x_1^2+x_2^2)} e^{-2|\alpha|\alpha\cos(\phi)} \cosh\left(\frac{\sqrt{2}\alpha}{x_0}(x_1+x_2)\right) ,\end{aligned} \tag{2.25}$$

where $\alpha = |\alpha|\exp(i\phi)$.

For the further discussion, we now specialize to the case of $\alpha = i|\alpha|$ (i.e., $\phi = \pi/2$) to obtain a probability density

$$|\psi_{ccc}(x_1,x_2,\alpha = i|\alpha|)|^2 = \frac{4\mathcal{N}^2}{\pi x_0^2} e^{-\frac{1}{x_0^2}(x_1^2+x_2^2)} \cos^2\left(\frac{\sqrt{2}|\alpha|}{x_0}(x_1+x_2)\right) . \tag{2.26}$$

The structure of this expression resembles the probability density for the two photon NOON states. Other choices for $\phi$ allow to rotate the fringe pattern in the position space with respect to the centroid axis. This way, the condition for the centroid method that the probability density should separate into a function of the centroid coordinate times a function of all other coordinates can be continuously violated by modifying $\phi$ from $\pi/2$.

As before, for the numerical calculations we define dimensionless position variables $\bar{x}$. For $x = 2\pi\, x_0\, \bar{x}$, Eq. (2.26) becomes

$$|\psi_{ccc}(x_1,x_2,\alpha = i|\alpha|)|^2 = \frac{4\mathcal{N}^2}{\pi x_0^2} e^{-4\pi^2(\bar{x}_1^2+\bar{x}_2^2)} \cos^2\left(2\pi\sqrt{2}|\alpha|(\bar{x}_1+\bar{x}_2)\right) . \tag{2.27}$$

Comparing Eq. (2.27) with Eq. (2.15), we find that the exponential parts of the two expressions agree for $\sigma = 1$, whereas the cosine-parts differ in the sense that the cat state allows to continuously tune the structure size of the fringe pattern by varying $|\alpha|$. This way, the sub-wavelength resolution capabilities of the centroid method can be probed independent of the number of detected photons.

Note that alternatively, one could choose dimensionless variables $x = \sqrt{2}\pi/|\alpha|\, x_0 \bar{x}$, such that the cosine-parts of the NOON-state and the cat-state probability densities become the same. However, in this scaling, neither the overall scaling nor the width $\sigma$ of the cat state are independent of the choice of $|\alpha|$.

The probabilty distribution for $\phi = \pi/2$ in configuration space is shown in Fig. (2.3). Increasing $\phi$ from $\pi/2$ (Fig. (2.3b) results in an increase of the width of each fringe along the centroid direction such that the fringes merge into each other. Further increase causes the middle fringe to become smaller and smaller until eventually at $\phi \approx \pi$, the two modes of the coherent states no more interfere and can be seen as separate circles.

## 2.2.3 Numerical experiments

In order to simulate the centroid method numerically, we first generate a large number of random photon events distributed and correlated according to the respective position space wave function. Next, we apply a discretization scheme to model the experimentally accessible signal for different detector characteristics. Finally, we perform the centroid analysis on this data to recover a wave function. We then compare this wave function to the original position space wave function and calculate the root-mean-square deviation to access the predictive power of the centroid method for the given conditions. In the following, we describe all steps in more detail.

### 2.2.3.1 Random number generation

The first step is to generate random photon events according to the respective position space wave function. As can be seen from Eqs. (2.15), (2.21) and (2.27), the position variables are correlated. To facilitate the random event generation, we apply unitary transformations to a set of uncorrelated variables. For example, the probability distribution

$$2\left(\frac{\Delta k}{\sqrt{\pi}}\right)^2 e^{-\Delta k^2\,(x_1^2+x_2^2)} \cos^2\left[k_0(x_1+x_2)\right] . \tag{2.28}$$

of Eq. (2.15) specialized to the case of two photons ($N = 2$) does not allow to draw random positions $x_1, x_2$ independently. Applying the transformation

$$\vec{Y}_2 = M_2 \vec{X}_2, \tag{2.29}$$

with $\vec{X}_2 = (x_1, x_2)^T$, $\vec{Y}_2 = (y_1, y_2)^T$, and

$$M_2 = \frac{1}{\sqrt{2}} \left[\begin{array}{cc} 1 & -1 \\ 1 & 1 \end{array}\right] ,$$

the probability distribution Eq. (2.28) becomes

$$2\left(\frac{\Delta k}{\sqrt{\pi}}\right)^2 \left(e^{-\Delta k^2\, y_1^2}\right)\left(e^{-\Delta k^2\, y_2^2}\,\cos^2\left[\sqrt{2}k_0 y_2\right]\right)\,. \tag{2.30}$$

In this form, random values can be drawn for $y_1$ and $y_2$ independently. In a similar way, also 3- and 4-photon events can be handled, with coordinate transforms

$$M_3 = \frac{1}{\sqrt{3}}\begin{bmatrix} 1 & 1 & 1 \\ 0 & \sqrt{3/2} & -\sqrt{3/2} \\ \sqrt{2} & -1/\sqrt{2} & -1/\sqrt{2} \end{bmatrix}$$

and

$$M_4 = \frac{1}{\sqrt{4}}\begin{bmatrix} 1 & 1 & 1 & 1 \\ 0 & 0 & \sqrt{2} & -\sqrt{2} \\ 0 & 2\sqrt{2/3} & \sqrt{2/3} & -\sqrt{2/3} \\ \sqrt{6} & -1/\sqrt{3} & -1/\sqrt{3} & -1/\sqrt{3} \end{bmatrix},$$

respectively.

One can easily verify that all the transformed basis vectors are normalized as well as mutually orthogonal. As an example, we write down explicitly the new basis vectors that span the space for 3 photon case in the following.

$$(\frac{x_1+x_2+x_3}{\sqrt{3}},\ \frac{x_2-x_3}{\sqrt{2}},\ \sqrt{\frac{2}{3}}x_1 - \frac{x_2+x_3}{\sqrt{6}})^T, \tag{2.31}$$

where $\vec{X}_3 = (x_1, x_2, x_3)^T$ comprise the original basis in 3 dimensions.

After application of the variable transform, for the NOON and correlated coherent cat states, $N-1$ of the new variables follow univariate normal distributions. The only exception is one variable which coincides with the centroid coordinate except for an overall scaling factor of $\sqrt{N}$. For the random number generation in this variable, we apply the cumulative distribution function. This function for a continuous random variable $V$ is obtained from the probability density function $\mathcal{I}$ via

$$\mathcal{F}_V(v) = \int_{-\infty}^{v} \mathcal{I}(t)dt, \tag{2.32}$$

If $x_i$ are random numbers drawn from the cumulative distribution, $\mathcal{F}^{-1}(x_i)$ is a random sample from $\mathcal{I}$.

The situation is simpler in the case of a jointly Gaussian distribution. In this case, all transformed variables follow univariate Gaussian distributions, even though one of the new variables is proportional to the centroid variable.

A back-transformation from the variables $y_i$ to the original coordinates $x_i$ via the inverse $M_i^{-1}$ (or equivalently $M_i^T$, since the matrices are unitary) then yields the desired correlated photon events. In all cases, we verified that the position distribution of the obtained random numbers agree to the original respective position space distribution functions.

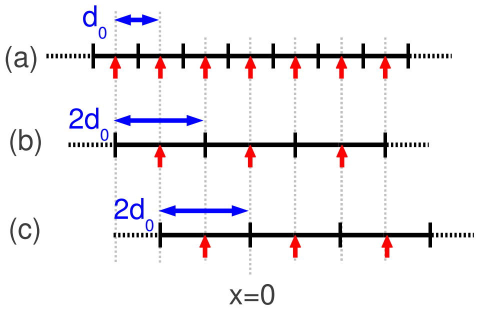

Figure 2.4: (Color online) Model for the detection setup. (a) shows an array of detectors of size $d_0$. The red arrows indicate the central positions of the individual detectors. (b) shows the corresponding array with double detector size $d_0$. Compared to (a), only half of the possible detection positions occur. (c) shows the array of (b) suitably shifted that now the possible detection events cover those of (a) which are missing in (b).

### 2.2.4 Modeling of the detection system

The positions of the correlated $N$-photon states obtained in the previous section are continuously distributed. Any measurement, however, employs detectors of finite size, which yield a discretized position information. To model this discretization, we assume an array of identical detectors, as shown in Fig. 2.4(a). Each detector has size $d_0$. We assume that the detectors do not overlap, and that there is no space between two adjacent detectors. Thus, each photon position of the continuous position distribution obtained from the random number generation can uniquely be assigned to a single detector. The numerical discretization procedure thus amounts to replacing the position of each individual photon with the central position of the detector which registers the respective photon.

In a suitable coordinate system, the possible measurement outcomes are $i\, d_0$, with $i \in \mathbb{Z}$. The possible outcomes for the centroid coordinate in a $N$-photon detection with photons hitting the $i_n$th detector ($1 \leq n \leq N$) then follow from Eq. (2.8) as

$$X = \frac{d_0}{N} \sum_{n=1}^{N} i_n \,. \tag{2.33}$$

If the detector size is changed, also the set of possible detection outcomes is changed. For example, in Fig. 2.4(b), detectors of double the size compared to those in (a) lead to a set of possible measurement outcomes which contain only every second possibility compared to that of (a). In addition, the detection array can be shifted, with an example for shift $d_0$ shown in Fig. 2.4(c). The measurements of (b) and (c) together allow for a set of potential measurement outcomes which coincides with that of (a). Note, however, that the detectors in (b) and (c) overlap spatially, such that the combined measurements of (b) and (c) are not equivalent to measurement (a).

Throughout the later analysis, we will compare the performance with different detector sizes. In order to obtain comparable predictions for the wave function, we proceed as follows. For the smallest detector size $d_0$, we apply the centroid method for a single detection array position, which we denote as shift 0. Next, we double the detector size to $2d_0$, and obtain centroid data at the two shift positions 0 and $d_0$. Analogously, for detectors of size $m\,d_0$, we calculate centroid data for $m$ suitable shifts. This way, the wave function is estimated at the same set of positions for all detector sizes.

For this analysis, we employ two different methods for the calculations for different shifts. First, we generate $N_0$ realizations of the correlated $N$-photon state as described in Sec. 2.2.3.1. In method I, we then use the total number of $N_0$ events for each of the $m$ required shifts. In method II, we divide the total number of events $N_0$ by the number of shifts $m$, and evaluate each shift with $N_0/m$ events only. In terms of an experimental realization, in method I, the number of measurements required increases with detector size, whereas in method II, the number of measurements is independent of the detector size.

Due to the statistical nature of the measurement, in principle, also a limited number of individual non-adjacent detectors can be used, if their positions are shifted such that the combinations of all measurements cover the entire beam correlation area. This method has been adopted in [61, 135]. While the measurement time increases, the complicated fabrication process for an array of detectors can be avoided in proof-of-principle measurements.

### 2.2.5 Error estimation

To evaluate the performance of the centroid method for given detection parameters, we first fit the centroid data to the original distribution in order to obtain the optimum overall scaling factor for the centroid data, and multiply the centroid data with this factor. This is necessary, as we evaluate the centroid data only over a limited position range, such that the overall normalization of the measured centroid data a priori is unknown. We then employ the weighted root mean square deviation given by

$$\frac{1}{\sqrt{b}}\sqrt{\sum_{i=1}^{b} ||\psi(X_i)|^2 - z_i|^2}, \tag{2.34}$$

where $b$ is the number of centroid data points, and $|\psi(X_i)|^2$ and $z_i$ are the reference value from the original probability distribution and the estimate obtained from the centroid method, respectively, at positions $X_i$.

Note that the rms deviation in part depends on the spatial extent over which the centroid data is compared to the original wave function. If a larger range is considered, positions are included into the analysis for which both the original probability distribution and the centroid prediction are very low, such that they in essence do not increase the sum in the rms deviation, but only $b$. This is particularly important if rms values for different wave functions are compared.

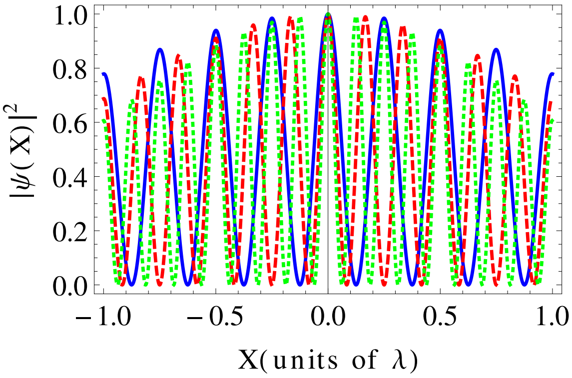

Figure 2.5: (Color online) Result of the centroid method for NOON states with different $N$, shown against the centroid position in units of the single-photon transverse wavelength $\lambda$. Continuous blue, dashed red, and dotted green curves correspond respectively to $N = 2$, 3 and 4. The increase in the number of fringes clearly shows the resolution enhancement with $1/N$.

## 2.3 Results

In the following, we present our results for three different trial states. We start with NOON states.

### 2.3.1 NOON States

#### 2.3.1.1 Resolution enhancement

Fig. 2.5 depicts the the centroid probability distributions for two, three and four photon NOON states, obtained with a detector size small enough to resolve all features of the wave function. It can be seen that there are $2N$ fringes per wavelength for $N$ photons, confirming the expected scaling of the obtained resolution with $1/N$. We thus find that our simulation technique is able to recover the predicted resolution enhancement.

#### 2.3.1.2 Dependence on the detector size

We thus turn to a detailed analysis of the centroid technique. As our first step, Fig. 2.6 shows the dependence of the rms deviation of the recovered two-photon centroid distribution from the original position space distribution as a function of the detector size. As expected, the deviation is low for small detectors, and initially increases with growing detector size. Starting from detector sizes of about $\lambda/2$, the rms deviation saturates. Next to this general structure, an increase of the deviation at detector size $\lambda/4$ and $3\lambda/4$, as well as sudden drops in the rms for $\lambda/2$ and $\lambda$ can be observed. Finally, towards very low detector sizes, the rms deviation starts to increase again. In the following, we will explain and interpret all of these features.

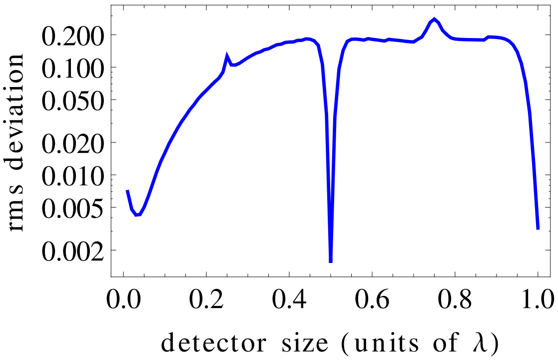

Figure 2.6: (Color online) Root-mean-square deviation of the recovered two-photon centroid distribution from the original wave function position space distribution as a function of the detector size. Note the logarithmic scale.

First, we analyze the structures at $\lambda/4$, $\lambda/2$ and $\lambda$. For this, we choose a detector size, and then calculate the rms deviation as a function of a shift of the whole detector array along the centroid axis without modifying the detector size. The results are shown in Fig. 2.7. It can be seen that for detector sizes other than $\lambda/4$, $\lambda/2$ and $\lambda$, the rms deviation is approximately constant over the whole range of shifts. For these detector sizes, we conclude that the naive expectation that a smaller detector leads to a better recovery of the wave function is correct.

In contrast, at detector size $\lambda/2$, the rms deviation strongly depends on the shift. Even more surprisingly, while there is a slight dependence on the detector shift for detector sizes $\lambda$ and $\lambda/2$, the rms deviation remains very low for all shifts despite the large detector size. We will show now that these result are artifacts of the calculation procedure, which arise due to the particular structure of the wave function to be recovered.

Fig. 2.8 explains the situation for detector size $\lambda/4$. In (a), the original position distribution along the centroid direction for a two-photon NOON state is shown together with the centroid data obtained for detector size $\lambda/4$ and zero shift. For this shift value, one of the centroid data points coincides with the position distribution maximum at $X = 0$. It can be seen that half of the centroid data points coincide perfectly with the original distribution - but the other half strongly deviates. The reason is that the position distribution is zero only at single points, whereas the large detectors cover a range around these zeros with non-zero photo detection probability. As a result, the centroid data is non-zero, in contrast to the probability distribution. This deviation for half of the points explains the large rms value at zero shift in Fig. 2.7. We next consider the same setting, but with shift $s = -13\lambda/200$, corresponding to a minimum in the rms value for detector size $\lambda/4$ in Fig. 2.7. Fig. 2.8(b) shows the corresponding centroid result obtained with the same scaling of the centroid data as in (a) as blue dots. It can be seen that the deviation to the probability distribution is strong. But if we fit the overall scaling factor of the centroid data to the original distribution, then good agreement is obtained. This is the reason for the minimum in Fig. 2.7, in which the centroid data is fitted to the original distribution for each shift position individually. The analogous analysis for detector size $\lambda$ is shown

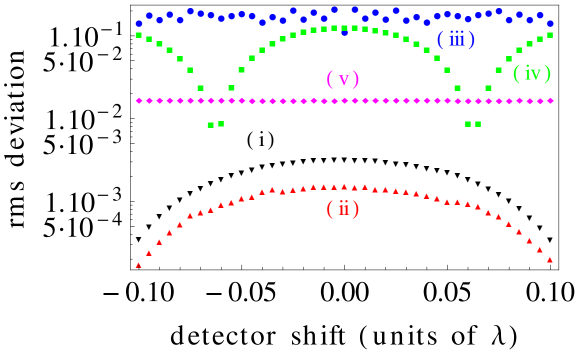

Figure 2.7: (Color online) Root-mean-square deviation of the recovered two-photon centroid distribution from the original wave function position space distribution as a function of the detector shift. The different curves show results for the detector sizes (i) triangles faced right $\lambda$, (ii) triangles faced left $\lambda/2$, (iii) blue blobs $0.3\lambda$, (iv) green squares $\lambda/4$, and (v) magenta rhombuses $\lambda/10$. Note the logarithmic scale.

in Fig. 2.9. In this case, due to the $\lambda$-periodicity of the wave function, a perfect fit of the centroid data is possible for any detector shift.

However, in an actual measurement, results from all shifts would have to be accounted for with the same overall prefactor, as an individual fitting to the unknown distribution to be determined is impossible. For this reason, detectors of size $\lambda$ or $\lambda/2$ cannot recover the wave function. To show this, we have taken a set of $N_0 = 10^6$ detection events, calculated the centroid distributions for a large number of shifts, and joined the corresponding distributions for the respective shifts without further processing them beforehand. Only the total set obtained from all shifts was then fitted in amplitude to the original position distribution. The result was a structure-less Gaussian which did not contain the sub-wavelength fringe features of the original distribution. Therefore, in conclusion, it is not possible to recover the wave function with detectors of specific larger sizes, despite the small rms deviation for specific detector shifts, which has to be interpreted as an artifact of the analysis. Note, however, that such measurements with larger detectors could potentially be sufficient to analyze the periodicity or the symmetry of a given wave function.

Next, we analyze why the rms deviation increases again at very small detector sizes. We found that this is a statistical effect. If the detector size is decreased while the detection area is kept constant, the number of detectors increases. Then, the mean number of events per detector decreases with the detector size. At some point, the statistical fluctuations due to the decreasing number of events become large enough to dominate the rms deviation. In order to verify this interpretation, we evaluated the rms deviation (i) once for $10^6$ events, (ii) twice for two subsets with $5 \times 10^5$ events, (iii) 5 times for subsets of $2 \times 10^5$ events, and (iv) 10 times for subsets of $10^5$ events. In all cases, the same $10^6$ events were analyzed, and the respective subsets were chosen disjunct. After this, we averaged the results over the respective subsets, such that in every case, the same events were analyzed. The result is shown in Fig. 2.10. It can be seen that the rms deviation of

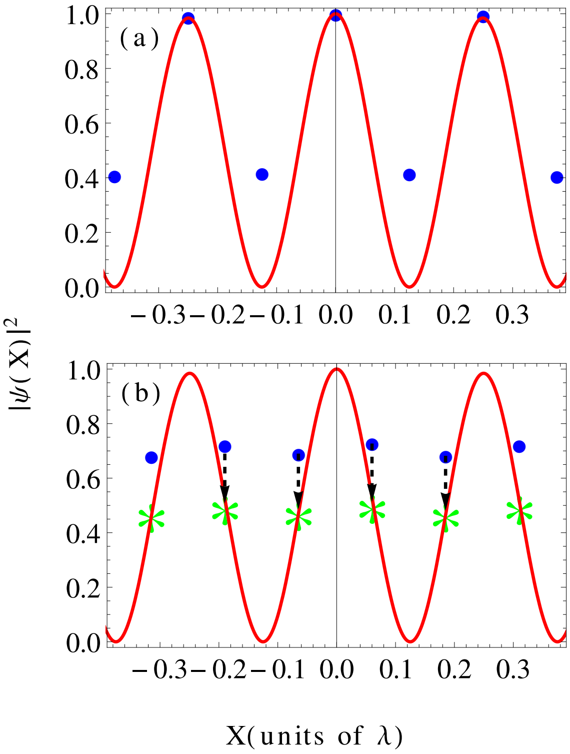

Figure 2.8: (Color online) Centroid analysis for detector size $\lambda/4$. The continuous red curve shows the probability distribution for a 2-photon NOON state. The blue dots indicate the results of a centroid measurement with particular detector settings. In (a), the detection array is not shifted with respect to the origin of the probability distribution, such that one of the centroid data points coincides with the center position $X = 0$. (b) The detection array is shifted to $s = -13\lambda/200$, which corresponds to a minimum in the rms deviation in Fig. 2.7. The blue dots show the centroid data with the same scaling as in (a). The green asterisks show this data fitted to the original distribution.

all cases approximately agrees towards larger detector sizes. But towards smaller detector sizes, the smaller the corresponding subsets are, the more the deviation increases. Note that also the difference in rms deviation between different subsets of equal size is much smaller than the difference in deviation between subsets of different size.

#### 2.3.1.3 Comparison of the two methods

In this section, we compare the two analysis methods I and II introduced in Sec. 2.2.4. Fig. 2.11 shows results for a 2-photon NOON state using the two methods. The two curves for method I (blue squares) and II (red dots) agree for larger detectors, but deviate for small detectors. In particular, the unexpected increase in the rms deviation towards low detector sizes observed in Fig. 2.10 and interpreted as statistical fluctuations due to a low number of events per detection bin is absent for method II.

The reason for this qualitative difference is as follows. For the lowest detector size $d_0$, no

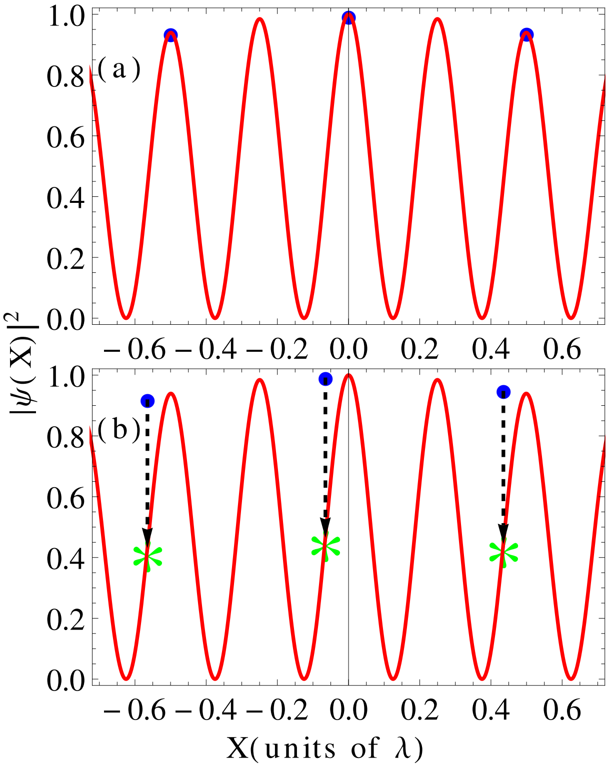

Figure 2.9: (Color online) Centroid analysis for detector size $\lambda$. The figure is analogous to Fig. 2.8, except for the detector size.

shift is required, and the two methods are equivalent. Thus, the same rms deviation is obtained. As can be seen from the increase in the rms value for method I, the prediction at this detector size is already limited by the low number of events per detection bin. For the next higher detector size $2d_0$, in method I, the number of events per detection bin is increased, as the same number of $N_0$ events are distributed over a lower number of bins. In contrast, for method II, the number of events per bin is not increased, as with increasing detector size, the number of events considered for each detector shift is reduced. As a consequence, the rms deviation for method II monotonously increases with detector size, whereas that for method I can decrease with increasing detector size. In the latter case, the reduction of the rms due more events per bin on average outweighs the increase in rms due to the increase of the detector size.

This interpretation is further supported by the two other data sets in Fig. 2.11. These show method II, but with half the number of events (green diamonds) or one third of the events (black triangles). It can be seen that the rms results for the smallest detector size $d_0$ roughly agree with those for method II with half the data points at detector size $2\,d_0$. Further, the rms for method II with one third of the data points agrees to this value at detector size $3\,d_0$. This shows that for such small detectors, the rms is dominated by the low number of counts per bin.

We obtained qualitatively similar results also for $N \in \{3, 4\}$.

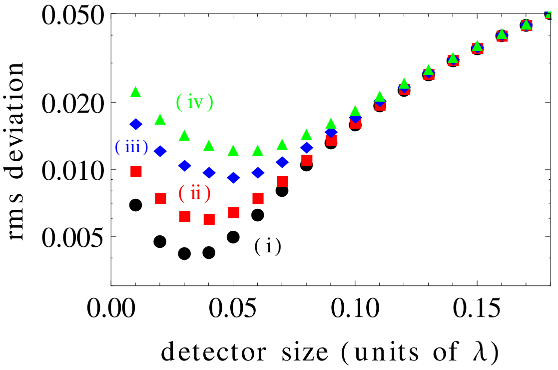

Figure 2.10: (Color online) Effect of statistical fluctuations on the centroid methods for small detector sizes. The rms deviation was evaluated (i) black blobs, once for $10^6$ events, (ii) red squares, twice for two subsets with $5 \times 10^5$ events, (iii) blue rhombuses, 5 times for subsets of $2 \times 10^5$ events, and (iv) green triangles, 10 times for subsets of $10^5$ events. In all cases, the same $10^6$ events were analyzed, and the respective subsets were chosen disjunct. The figure shows the results averaged over the respective subsets. Note the logarithmic scale.

#### 2.3.1.4 Multiphoton NOON states

We now turn to NOON states with higher photon number. Fig. 2.12 shows the rms deviation as a function of the detector size for $N = 2$, 3 and 4 photons. Note that Fig. 2.12 has been generated including all detector shifts required for the respective detector sizes, such that the spurious maxima or minima in the rms deviation at specific detectors sizes found in Fig. 2.6 due to the dependence on the shift position shown in Fig. 2.7 do not appear. All data points are generated using the same $N_0 = 10^6$ events with method I introduced in Sec. 2.3.1.3. As the spatial extent over which the probability distribution is significantly larger than zero decreases with increasing photon number $N$, we adjust the position range over which the wave function is matched to the centroid measurement accordingly. Thus, the 3- and 4-photon cases are evaluated over 2/3 and 2/4 = 1/2 the range of that of the $N = 2$ case, respectively.

It can be seen that at small detector sizes, the rms deviation is low and approximately independent of $N$. In this limit, the detectors are chosen small enough to recover all features even of the $N = 4$ wave function. With increasing detector size, the rms deviation starts differing from the small-detector limit value first for the $N = 4$, then for the $N = 3$, and finally for the $N = 2$ case. Increasing the detector size further, the rms deviation has an approximately linear dependence of the detector size, until it eventually saturates for the large-detector limit. Note also that the spatial extent of the near-linear region reduces with an increase in $N$. From Fig. (2.5) shows that the range of regions of large slope decreases as the value of $N$ is incremented.

In the near-linear region, we estimate slopes $\alpha = \Delta(\text{rms deviation})/\Delta(\text{detector size})$ for $N = 2$, 3 and 4 as 0.57, 0.72 and 0.87, as indicated in Fig. 2.12, respectively. These values are consistent with a scaling with $\sqrt{N}$. One possible interpretation of this scaling could

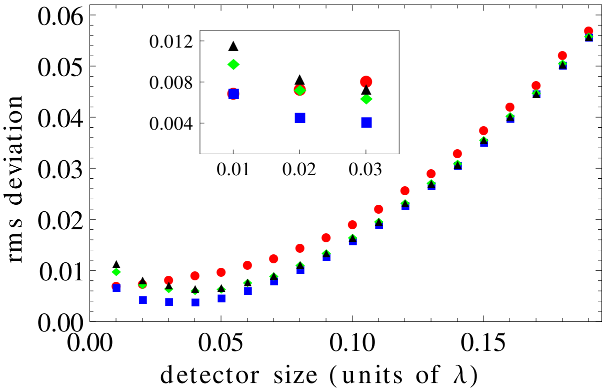

Figure 2.11: (Color online) (a) Root-mean-square deviation as a function of detector size. Results are shown for a two-photon NOON state. The blue squares are obtained using method I discussed in the text, whereas the red dots are obtained using method II. The green diamonds and the black triangles are obtained using method II with one half and one third of the total number of events used in (a), respectively. Inset shows a magnification at small detector sizes.

be as follows. If the detection positions of each of the $N$ photons acquires an uncertainty of order $d_0$ due to the finite detector size, then an estimate of the uncertainty of the centroid coordinate $X = \frac{1}{N}\sum_{i=1}^{N} x_i$ is given by $\delta X = d_0/\sqrt{N}$. This estimate is motivated by the fact that the sum of $N$ normally distributed independent variables with widths $\delta x$ is again a normal distribution, with width $\sqrt{N}\delta x$. Approximately, it also holds for other distributions. Together with the prefactor $1/N$ in the centroid variable, a scaling of $1/\sqrt{N}$ in the centroid coordinate uncertainty is obtained. Next, we use that an increase of the detector size from the low-size limit leads to most significant contributions to the rms deviation in the regions of highest slope of the centroid probability distribution. We denote such a centroid coordinate with highest slope as $x_{max}$, and note that the value of the $\cos^2()$ part in the probability distribution evaluates to $1/2$ at this point. We thus can estimate the scaling of the rms deviation via

$$\frac{1}{\sqrt{\delta X}}\sqrt{\int_{x_{max}-\delta X/2}^{x_{max}+\delta X/2}\left|\cos^2(2\pi N x)-\frac{1}{2}\right|^2 dx} \tag{2.35}$$

To leading order in the detector size, this expression scales as $\sqrt{N}\,d_0$, i.e., linearly with the detector size, and with slope proportional to $\sqrt{N}$, as observed in the numerical data.

#### 2.3.1.5 Single- and multi-photon detection

One motivation for the centroid measurement method is the technical difficulty to achieve multi-photon or photon-number resolving detection, as required, e.g., for sub-wavelength correlated multiphoton measurement schemes. If the size of the individual detectors in the centroid method is small enough, the number of events in which two or more photons hit the same detector is negligibly small, such that no photon number resolution is required.

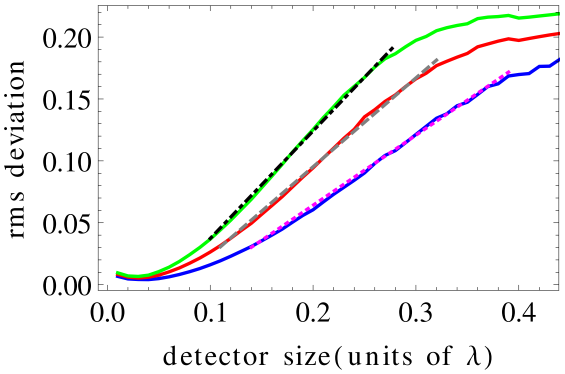

Figure 2.12: (Color online) Root-mean-square deviation versus detector size for NOON states using method I. Results are compared for number of photons $N = 2$ (lower blue curve), $N = 3$ (middle red curve), and $N = 4$ (upper green curve). The lines indicate linear fits to the curves over the indicated detector size range.

Motivated by this, we have analyzed the percentage of two-photon events in our numerical calculations, as a function of detector size. We denote the position range over which the photon probability distribution is evaluated by $\rho$. In the numerical calculations, $\rho$ is chosen such that it encompasses all parts of the probability distribution which are significantly larger than zero. For detector size $d_0$, we then estimate the number of detection bins $p$ as integer closest to $\rho/d_0$.

We then count those events in which all photons arrive in the same bin as a multi-photon detection event. There are $p$ different possibilities to realize a $N$-photon detection event. Overall, in our numerical calculation, there are $p^N$ different possible events, as we do not make use of the symmetrization of the photon states and therefore distinguish between events, e.g., in which two photons are detected at positions $x_1, x_2$ and $x_2, x_1$. Thus, we expect a ratio of multi-photon events given by approximately $p/p^N$. In terms of the detector size, we find that $p/p^N \sim d_0^{N-1}$. We then numerically generate random detection events, discretize them to model the detection procedure, and count all events in which all photons arrive in the same detection bin as multi-photon detection events. Finally, we calculate the percentage of the such obtained multi-photon events out of all detection events. Our numerical analysis indeed confirms the analytical estimate.

Note that for the NOON state, the ratio of two-photon events reaches about 14% probability for detectors of size $\lambda$. This maximum value may appear high, but it arises from the fact that in our calculations the parameters are such that the non-negligible support of the probability distribution only covers few single-photon wavelengths. Then, a detector that is wavelength sized already covers a significant part of the total relevant centroid coordinate range. It is important to note that our calculations remain valid despite the two-photon events, since our numerical approach naturally is capable of photon-number resolving "measurements" such multiphoton events do not have to be discarded.

For the numerical simulations, we have used $\rho = 7\lambda$ for $N = 2$. For $N > 2$, we used accordingly $\rho = 7\lambda * 2/N$.

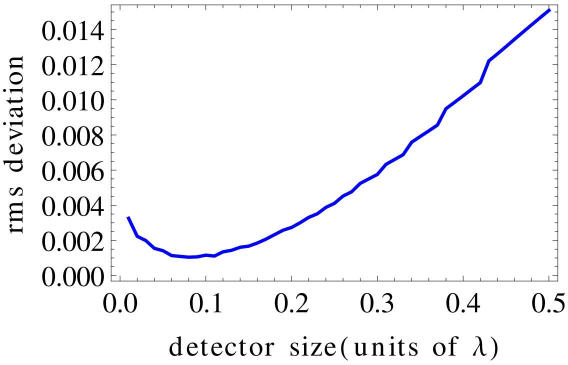

Figure 2.13: (Color online) Root-mean-square deviation versus detector size for a jointly Gaussian state using method I. The parameters are same as Fig. (2.2).

### 2.3.2 Jointly Gaussian States

We now turn to the analysis of jointly Gaussian states, as suggested in [54]. The analysis is performed in a similar way as for the NOON states. First results for the dependence of the rms deviation on the detector size incorporating all the shifts at larger detector sizes using method I are shown in Fig. (2.13). As for the NOON state, the rms deviation increases with detector size, as naively expected. The increase of rms deviation towards the smallest considered detector sizes is again due to statistical effects, as explained in Sec. 2.3.1.2. Compared to the NOON states, the absolute values of the rms derivation are smaller, which is due to the much simpler structure of the Gaussian states.

As for the NOON states, we also analyzed the rms deviation versus different detector sizes without taking into account shifts of the detector array. Contrary to the case of NOON states, there is no qualitative difference between the results with and those without shift. The reason is that for the Gaussian states, there is no fringe pattern in centroid direction which could match the periodicity of the detection array.

For jointly Gaussian states, the ratio of two photon events and the total number of events again increases uniformly with an increase in the detector size, as expected. But the ratio of two-photon events is much higher than for NOON states. For example, for a large detector size of one equal to a full wavelength, already about 50% of the total events become two photon events, i.e., both photons fall on the same detector. The reason for this is that the spatial extent of the wave function in centroid direction is on the order of $\lambda$, see Fig. (2.2).

#### 2.3.2.1 Resolution Enhancement versus Multi photon Absorption

Next to the accuracy of the wave function recovery, also the efficiency is of relevance in any practical implementation. In essence, the measurement time is limited. This raises the question, how a limited number of measurements can be used in the most efficient way. In particular, in [62], the efficiency of centroid detection was compared to

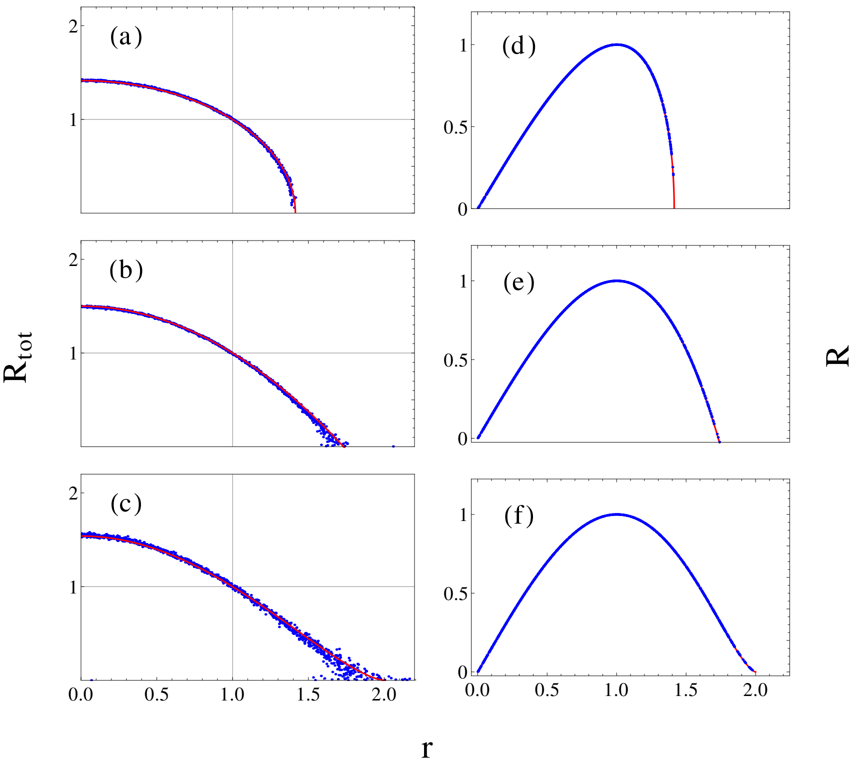

Figure 2.14: (Color online) $\langle k_n^2 \rangle = \lambda^{-1}$. (a-c) Total multi photon absorption rate and (d-f) peak multi photon absorption rate versus the spot size reduction factor for jointly Gaussian state. (Top, middle and bottom row) correspond to $N \in \{2, 3, 4\}$, respectively. The data points obtained via numerical calculation are blue while red is the theoretical prediction. We multiplied the $R_{tot}$ values with $17.8, 156, 4100$ for $N \in \{2, 3, 4\}$, respectively to normalize the data such that at $r = 1$ the corresponding value on the $y$-axis becomes unity too.

that of a multiphoton detection scheme. To analyze this in our numerical calculation, a practical way to distinguish single- from multi-photon detection events is required. We thus introduce a distance $d_{MP} = \lambda/400$, and denote $N$ photons which would hit a detector with unlimited position resolution at distance smaller than or equal to $d_{MP}$ a $N$-photon event. Photons separated by more than $d_{MP}$ are registered as individual single-photon events.

We start by analyzing the multi-photon absorption rate as a function of the spot size reduction factor $r$, which has been defined in [62] as the ratio of the classical width $W_C$ to the width $W$ of the probability distribution of the joint Gaussian defined by Eq. (2.20) for different choices of the parameters $B$ and $\beta$ such that $\langle k_n^2 \rangle$ has a fixed value. Explicitly, $r = \sqrt{N}B/\sqrt{\langle k_n^2 \rangle}$. $r = 1$ defines the standard quantum limit, whereas the ultimate Heisenberg limit is given by $r = \sqrt{N}$.

Our numerical scheme works as follows. We first fix $\langle k_n^2 \rangle$ to a positive integer multiple of $\lambda^{-1}$. Then, we vary $B$ and calculate $\beta$ from Eq. (2.19). Note that if $\langle k_n^2 \rangle$ is fixed to a

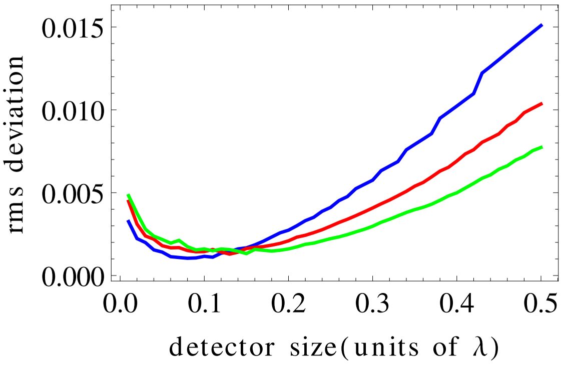

Figure 2.15: (Color online) Root-mean-square deviation plotted versus the detector size for a fixed physical size of the quantum mechanical jointly Gaussian centroid probability distribution for various $N$ using method I. The blue, red and green curves correspond respectively to $N = 2$, 3 and 4. The parameters are explained in the text.

large positive value in units of $\lambda^{-1}$, then many values of $r$ in the quantum regime given by $1 < r \leq \sqrt{N}$ cannot be accessed because increasing $B$ results in a $\beta$ which makes $B$ less than its classical value $\beta/\sqrt{N}$ . Afterwards, we generate random detection events as explained in Sec. 2.2.3.1. Note that we do not apply discretization to mimic detection by finite size detectors. We then determine those events which contain photons with distance smaller than or equal to $d_{MP}$ and call these *close events*. The width of the histogram of these close events provides us with the width $W$, which is calculated by fitting the histogram data to a Gaussian distribution of the form $ce^{-dx^2}$. The width $W$ is then given by $2/(\sqrt{2d})$. Afterwards, we divide the number of close events by the total number of $N$-photon events to calculate the normalized total multiphoton absorption rate $R_{tot}$. Fig. (2.14a) shows our results for the normalized total multiphoton absorption rate as a function of the spot size reduction factor for $N \in \{2, 3, 4\}$. It can be seen that the results quantitatively agree with the theoretical prediction $R_{tot} = ((N - r^2)/(N - 1))^{(N-1)/2}$ found in [62]. Note that the statistical fluctuation of our numerical data increases with $r$ towards the limiting value $\sqrt{N}$. The reason for this is that once the variance of $k_n$ is fixed, an increase in $B$ is balanced by a decrease in $\beta$. At $r = R_{tot} = 1$, the standard quantum limit is obtained which corresponds to a unit multi-photon absorption and a classical distribution. As $B$ is increased, the probability distribution becomes more narrow along the centroid direction, but expands along the orthogonal directions of the relative coordinates. This implies that the distance between any two random coordinates can be larger now. This is why with an increase in $B$, the number of *close events* decreases. For this calculation, we extracted 1 million pairs of random events. At $B = 0.01\lambda^{-1}$, out of the 1 million events, some $79,201$ are *close events* while at $B = 0.999\lambda^{-1}$, this number reduces to 3316.

Using our $r$, we can calculate normalized peak multi photon absorption rate defined in [62] as $r((N-r^2)/(N-1))^{(N-1)/2}$. Fig. (2.14d) shows the corresponding result. The blue data points show the numerical results while red curve plots $r\sqrt{2 - r^2}$. Again, the two results agree at most of the range of spot size reduction factor $r$ but $r = \sqrt{N}$ is not approached

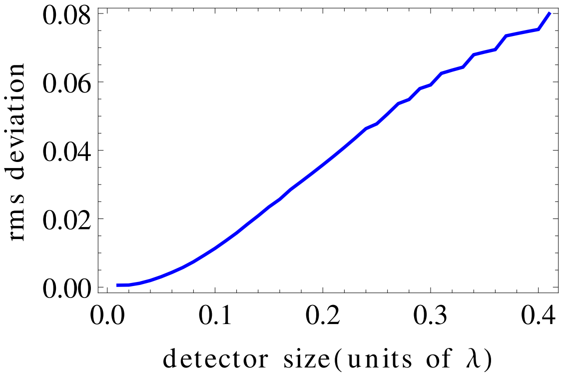

Figure 2.16: (Color online) Root-mean-square deviation against detector size for a correlated coherent cat state with $\alpha = \imath$. Results have been obtained using method I.

by the numerical data.

Note that we obtained qualitatively similar results also for $N = 3$ and $N = 4$ photon states, shown by Fig. (2.14b), (e) and (c), (f), respectively.

#### 2.3.2.2 Resolution Enhancement versus Multi photon Absorption for a Fixed Feature Size

So far, the analysis has been limited to cases in which the feature size decreases with increasing number of detected photons $N$. Now, we compare the rms deviation as a function of detector size for different $N$, but with physical feature size kept constant. For this, we notice that the probability distribution in centroid direction scales as $\exp(-2N^2B^2X^2)$, with $X$ the centroid coordinate. For each $N$, we choose $B$ in such a way that the resulting spatial extent of the distribution becomes $\exp(-8(X/\lambda)^2)$, which leads to $B = 2/(N\lambda)$. We further choose $\beta = 1/\lambda$ for $N = 2, 3$. For $N = 4$, we instead choose $\beta = 4/5\,/\lambda$, such that in all cases the parameters fulfill $B > \beta/\sqrt{N}$ and thus the probability distribution is non-classical.

The results presented in Fig. (2.15) show that as $N$ is increased, the value of rms deviation for a fixed detector size is decreased for most of the range of detector sizes. This is to be expected because if the physical size of the distribution is fixed, absorbing more photons should improve the result of the measurement. As explained before, the results at very small detector sizes are prone to numerical fluctuations if a fixed number of events is distributed over more and more detector bins.

Qualitatively similar results have also been obtained using method II. Again we found that method II leads to slightly higher rms deviations in particular at lower detector sizes, because of the lower number of events included in the calculation.

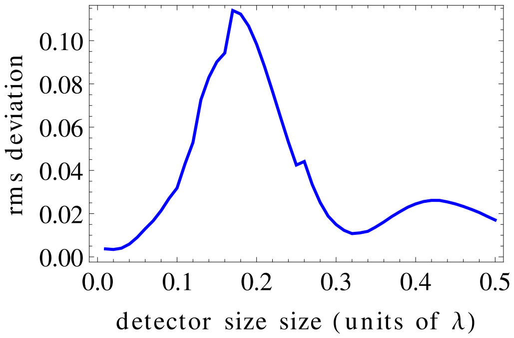

Figure 2.17: (Color online) Root-mean-square deviation versus detector size for a correlated coherent cat state with $\alpha = \imath$. In contrast to Fig. 2.16, results for a single fixed detector position are shown.

### 2.3.3 Correlated Coherent Cat States

Finally, we turn to coherent cat states. As for the other states, we start by discussing the rms deviation against the detector size. Results are shown in Fig. 2.16. Note that this figure was obtained including all different shift positions for the larger detectors, using method I such that the positions at which centroid data is obtained are the same for all detector sizes. The results is as expected, with a certain range of small detector sizes over which the recovery of the wave function is good, followed by a continuous increase of the rms with the detector size, until the rms saturates towards large detector sizes.

In contrast, the rms deviation for single fixed detection arrays of different sizes show a rather different behavior compared to the other considered states, as shown in Fig. 2.17. Here, an initial increase in rms deviation with the detector area is seen, as expected, but for detector sizes of about $0.17\lambda$, the rms deviation acquires a maximum and afterwards oscillates with the detector size. These features again can be explained via the shape of the probability distribution of the original wave function. Results for other shifts of the detection array give similar results for detector sizes up to about $\lambda/10$, but afterwards deviate significantly. As can be seen from Eq. (2.27), cat states have the advantage that the fringe pattern in centroid direction superimposed onto the overall Gaussian wave function envelope has a periodicity which can be controlled by the magnitude of $\alpha$. Since $|\alpha|^2$ is the mean number of photons in the corresponding cat state, this change in the fringe pattern goes along with a change in the number of photons in the light field. But nevertheless, some of the realizations of the cat state will consist of two photons independent of $|\alpha|$, such that we can continue to evaluate only those detection events. In this way, the feature size can be controlled without changing the number of detected photons. An example for a correlated coherent cat state with higher mean photon number ($\alpha = \imath\sqrt{2}$) is shown in Fig. (2.18). As compared to Fig. 2.3(b) with lower mean photon number, the number of fringes in the position space probability distribution increased as expected. Note that a similar shrinking was observed in Fig. 2.5 for NOON states with higher number of detected photons. Here, in contrast, the number of detected photons is kept constant at 2.

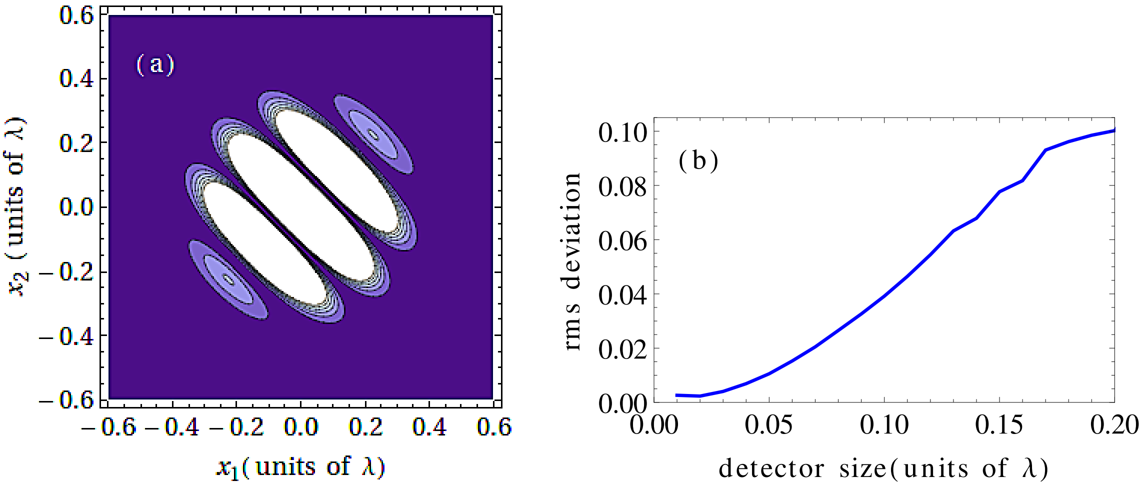

Figure 2.18: (Color online) (a) Probability distribution for a correlated coherent cat state with $\alpha = \imath\sqrt{2}$ in position space. (b) Root-mean-square deviation against detector size using method I.

Using the numerical simulations, we have verified that OCM works also if $\alpha = \sqrt{i} = \pm\sqrt{2}(1+i)/2$.

Finally, Fig. (2.19) shows the rms deviation as a function of $|\alpha|$. With increasing $|\alpha|$, the feature size of the wave function to be recovered becomes smaller, such that for a fixed detector size, increasing rms deviation with increasing $|\alpha|$ is expected. One can notice the approximate quadratic scaling with $|\alpha|$.

## 2.4 Summary

We have applied the centroid method for spatial resolution enhancement numerically to the non-classical states mentioned in [54], that is, NOON states and jointly Gaussian states and found another kind of states, correlated cat states which can be utilized for resolution enhancement with OCM. By generating a large number of random numbers as position coordinates for photons from the initial non-classical wave function and then calculating the centroid of the discrete detected data, we could recover the probability distributions along the centroid axis corresponding to all these states for various detection parameters.

The error between the numerical result and the predicted value has been estimated by the root mean square deviation. Interestingly, the results of rms deviation as a function of the size of the detector for the case of fixed detector positions can always be simply explained from impinging wave function. However, we found out evidences that a fixed detector array was not sufficient to recover the probability distribution completely. In order to obtain all the features of the probability distribution, we discovered that either detector arrays composed of very small sized detectors are needed or the detector positions require

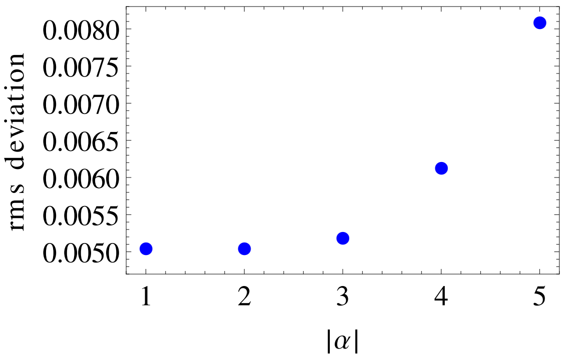

Figure 2.19: (Color online) Root-mean-square deviation for correlated cat states as a function of $|\alpha|$. In all cases, two-photon detection events are considered. $N_0 = 10^5$ events were considered with detector size $\lambda/100$.

to be shifted many times. Two methods are introduced for the detection procedure. Analysis of the results showed that only small sized detectors can be characterized as good detectors, as expected. Nevertheless, the strong statistical fluctuations were also most prominent at these detector ranges.

The resolution enhancement with an increase in the number of photons in the impinging wave function was verified.

Specially, jointly Gaussian states allow not only to study an increased resolution with $N$, but also, one can select parameters such that even if $N$ is increased, the same feature size is obtained. We studied the multi photon absorption in dependence of the detector size for both cases. In the first case, the maximum multi photon absorption rate could be obtained with a classical state, as shown analytically in [62]. The latter showed a better recovery of the wave function as more photons were absorbed. A similar multi photon analysis with mean number of photons in a coherent states was also carried out for the cat states.

We also confirmed that the probability of multi photon absorption increased linearly with the size of the detector.

## 2.5 Outlook

- Mathematical formalism which enable the detection of more than two photons from the incident wave function of a correlated cat state needs to be developed. This way, one can study the performance of the scheme with respect to the number of photons absorbed by the detector array.

- The conditions for the optical centroid method to work can be violated by adjusting the phase of the coherent states. One can study the efficiency of the method as a function of rotation of the centroid axis.

# Chapter 3

# Direct detection of $n$-particle atomic correlations via light scattering

The main results of this chapter are about to be submitted for a publication:
L. Jin, **Q. Gulfam**, M. Macovei, and J. Evers
*Direct detection of $n$-particle atomic correlations via light scattering*
which is an extension of [69].

*In [69], the creation and direct detection of $n$-particle atomic correlations in ensembles of atoms is investigated. An ensemble of laser-driven atoms in which either a dipole-dipole or a Rydberg-Rydberg interaction leads to the formation of correlations between the internal degrees of freedom of the atoms is studied. Light scattering is used to imprint information about these correlations onto light, and this information is extracted from the statistical properties of the scattered light. Observation in certain detection directions makes it possible to directly and individually measure $n$-particle atomic correlations. Here, we discuss in detail how to estimate the count rate of the scattered photons in these specific directions. We also discuss results for different number of atoms in the atomic ensemble.*

## 3.1 Introduction

The creation and detection of higher-order atomic correlations in an ensemble of atoms is studied in [69]. The authors aim at detecting correlations between the internal degrees of freedom of the atoms generated either by dipole dipole interaction (DDI) or Rydberg Rydberg interaction (RRI). For this, they analyze a linear chain of atoms which is driven by perpendicular laser beams, see Fig. 3.1. The focus is on the direct detection of atomic correlations by detecting the intensity-intensity correlation function $G^{(2)}$ of the light scattered by the atoms, with light scattering as the simplest transfer of atomic properties onto the light properties. They show that $G^{(2)}$ contains contributions which can be traced back

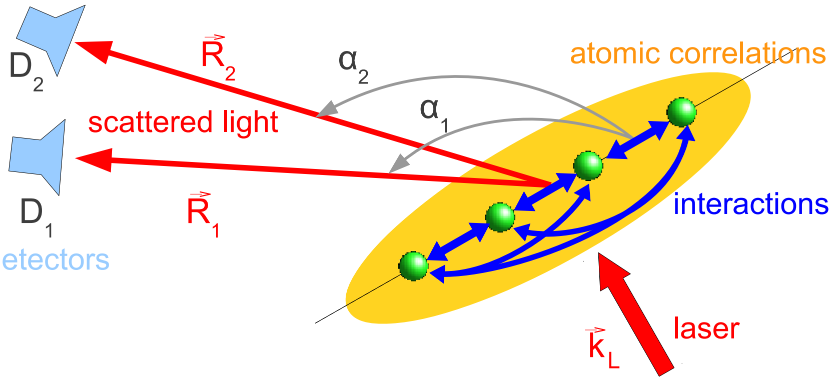

Figure 3.1: (Color online) A chain of $N$ atoms driven by a resonant laser field. Detectors $D_1$ and $D_2$ measure the second order correlation function of the scattered photons. The interaction among atoms leads to the formation of $n$-particle atomic correlations. Key objective is the direct measurement of these few-particle atomic correlations via the scattered light. (Figure taken from [69])

to 2-, 3- and 4-particle atomic correlations. A closer analysis reveals that observation in particular detection directions allows to detect the different $n$-particle atomic correlations individually. The method they propose is independent of the coupling generating the correlations, and results are given both for the case of DDI and RRI.

In order to carry out an experiment based on the mentioned scheme, the coincidence count rate of the scattered photons becomes an extremely important issue. Starting from their work, here, we develop a mathematical formalism which enables us to estimate the signal size from the $n$-particle atomic correlation directions. In the course of calculations, we find that it is very essential to take into account the correct prefactors in the correlation functions, which were not included in [69]. Moreover, directions can still be identified, and therefore an estimate of the coincidence count rate can also be obtained even if the number of atoms in the atomic chain varies.

## 3.2 Theoretical considerations

### 3.2.1 Model

A linear chain of $N$ atoms, as shown in Fig. 3.1 is investigated. The identical particles are modeled as three-level atoms with ground state $|g\rangle$, excited state $|e\rangle$, and Rydberg state $|r\rangle$ [154–156], and are located at positions $\vec{r}_i$ ($i \in \{1, 2, \cdots, N\}$), with $r_{ij} = |\vec{r}_i - \vec{r}_j|$. The lower [upper] transitions are driven by resonant laser fields with Rabi frequency $\Omega_p$ [$\Omega_c$]. Details of the theory can be found in [69].

As in [69], the master equation of the system is [157,158]

$$\frac{\partial \rho}{\partial t} = \frac{1}{i\hbar}[V,\rho] - \sum_{i=1}^{N} \frac{\gamma_c}{2}([A_{re}^{(i)}, A_{er}^{(i)}\rho] + \text{H.c.}) - \sum_{i,j=1}^{N} \frac{\gamma_p^{(ij)}}{2}([A_{eg}^{(i)}, A_{ge}^{(j)}\rho] + \text{H.c.})\,, \tag{3.1}$$

where $V = V_L + V_{dd} + V_{RR}$. $A_{\alpha\beta}^{(i)} = |\alpha\rangle_i\langle\beta|$ is an operator of $i$th atom, and $\gamma_p \equiv \gamma_p^{(ii)}$ $[\gamma_c]$ is the spontaneous decay rate on the lower [upper] transition. The atom-laser interaction is given by

$$V_L = \hbar \sum_i (\Omega_p A_{eg}^{(i)} + \Omega_c A_{re}^{(i)} + \text{H.c.})\,. \tag{3.2}$$

For the DDI case, we set $\Omega_c = V_{RR} = 0$. The coherent part of the DDI is given by

$$V_{dd} = -\hbar \sum_{i \neq j} \Omega^{(ij)} A_{eg}^{(i)} A_{ge}^{(j)}\,. \tag{3.3}$$

For RRI atoms, large inter atomic separations are assumed such that the DDI on lower transition vanishes.

$$V_{RR} = \hbar \sum_{i \neq j} V_{ij} A_{rr}^{(i)} A_{rr}^{(j)}\,, \tag{3.4}$$

where the coupling constant is given by $V_{ij} = C_6/|r_{ij}|^6$.

### 3.2.2 Observables

From the steady state solution of Eq. (3.1), in [69] the first and second order correlation function are calculated without taking into account the prefactors as [28,159]

$$G^{(1)} \propto \sum_{i,j} \langle A_{eg}^{(i)} A_{ge}^{(j)} \rangle e^{i\vec{k}_1\cdot\vec{r}_{ij}}\,, \tag{3.5a}$$

$$G^{(2)} \propto \sum_{i,j,k,l} \langle A_{eg}^{(i)} A_{eg}^{(j)} A_{ge}^{(k)} A_{ge}^{(l)} \rangle e^{i\cdot\vec{k}_1\vec{r}_{il} + i\vec{k}_2\cdot\vec{r}_{jk}}\,, \tag{3.5b}$$

The correlation functions $U^{(1)}$ and $U^{(2)}$ excluding the correlations between different atoms are defined in [69] as

$$U^{(1)} \propto \sum_{i,j} \langle A_{eg}^{(i)} A_{ge}^{(j)} \rangle_U e^{i\vec{k}_1\cdot\vec{r}_{ij}}\,, \tag{3.6a}$$

$$U^{(2)} \propto \sum_{i,j,k,l} \langle A_{eg}^{(i)} A_{eg}^{(j)} A_{ge}^{(k)} A_{ge}^{(l)} \rangle_U e^{i\cdot\vec{k}_1\vec{r}_{il} + i\vec{k}_2\cdot\vec{r}_{jk}}\,, \tag{3.6b}$$

For example, for any operators $A_i$ and $B_i$ operating on atom $i$ and any operator $C_j$ operating on a different atom $j \neq i$,

$$\langle A_i B_i C_j \rangle_U = \langle A_i B_i \rangle \langle C_j \rangle\,. \tag{3.7}$$

The outgoing wave vectors $\vec{k}_1$ and $\vec{k}_2$ are related to the detector positions as

$$\vec{k}_n \cdot \vec{r}_{ij} = (2\pi/\lambda)\,|\vec{r}_{ij}|\,\cos\alpha_n\,, \quad (n \in \{1,2\}) \tag{3.8}$$

The angles $\alpha_n$ correspond to the detection positions $\vec{R}_n$ in the far field.

## 3.3 Results

### 3.3.1 Without interaction

Without interaction

$$G^{(1)}(\vec{R}) = U^{(1)}(\vec{R}) = I\,N + C\sum_{i\neq j} e^{i\vec{k_1}\cdot\vec{r}_{ij}}\,, \tag{3.9}$$

where $I = \langle A_{ee}^{(i)}\rangle$ as a measure for the incoherent part of the scattered light intensity and $C = |\langle A_{eg}^{(i)}\rangle|^2$ as a measure for the coherent intensity are the same for all atoms $i$. The second-order correlation function can be decomposed as

$$G^{(2)} = U^{(2)} = G_2 + G_3 + G_4\,, \tag{3.10}$$

in which $G_n$ contains contributions involving $n$ atoms, i.e., those in which the indices $i, j, k, l$ in Eq. (3.5) take on $n$ different values. This decomposition allows for an interpretation of the different contributions.

### 3.3.2 With interaction

Correlations among the atoms appear as soon as they interact. Then, $G^{(1)} \neq U^{(1)}$ and $G^{(2)} \neq U^{(2)}$. Still $G^{(2)} = G_2 + G_3 + G_4$ and analogously $U^{(2)} = U_2 + U_3 + U_4$. The full second-order correlation function $G^{(2)}$ with the contribution due to $n$-particle atomic correlations subtracted is given by

$$\mathcal{C}_n = G^{(2)} - G_n + U_n\,, \tag{3.11}$$

At the detector positions for which $\mathcal{C}_n = 0$, or alternatively, $G^{(2)} = G_n - U_n$, the measured value for $G^{(2)}$ can directly be identified as the contribution arising from the $n$-atom correlations, such that the contribution of $n$-atom correlations can be detected and quantified individually. On the other hand, if $\mathcal{C}_n \gg G^{(2)}$, then $n$-atom correlations decrease the full $G^{(2)}$. This criterion again indicates atomic correlations but is in general, not guaranteed.

#### 3.3.2.1 Dipole-dipole interaction

We begin with the DDI atoms case. Fig. 3.2 shows results on the direct and individual detection of $n$-particle correlations. The contours plotted using Eq. (3.11) indicate that there are detection ranges in which $G^{(2)}$ is non-zero only due to 2-particle or 4-particle atomic correlations. At these positions, without the respective $n$-particle atomic correlation, the value of $G^{(2)}$ would be zero, and any detection signal directly can be traced back to the atomic correlations. Note that such regions do not occur for 3-particle atomic correlations. On the other hand, there are detection directions in which $\mathcal{C}_3/G^{(2)} \geq 10$ or $\mathcal{C}_4/G^{(2)} \geq 10$. Along these contour lines, the 3- or 4-particle atomic correlations dominate the value of $G^{(2)}$.

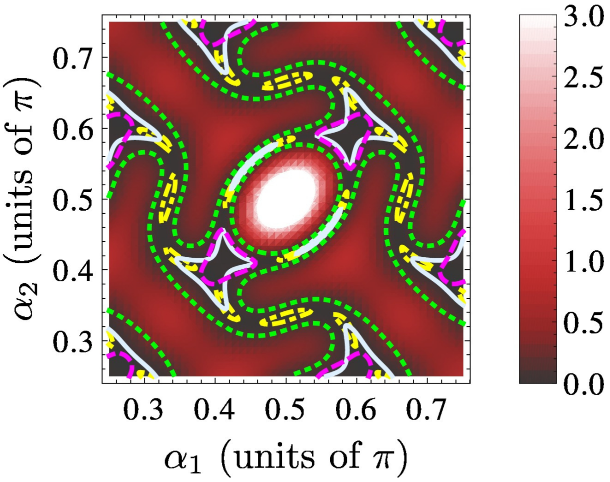

Figure 3.2: (Color online) Detection positions in which $n$-atom correlations can directly be measured for dipole-dipole interacting atoms. The dotted green contour indicates $\mathcal{C}_2 = 0$, and the dashed magenta contour $\mathcal{C}_4 = 0$. In these directions, $G^{(2)}$ is solely due to 2-atom or 4-atom correlations, respectively. The solid light blue contour shows $\mathcal{C}_3/G^{(2)} = 10$, and the dot-dashed yellow contour $\mathcal{C}_4/G^{(2)} = 10$. In these areas 3-atom or 4-atom correlations strongly reduce $G^{(2)}$, respectively. The background shows $G^{(2)}$. The results are plotted scaled by $10^6$ and against the positions of the two detectors $\alpha_1$ and $\alpha_2$ for $N = 4$, $\Omega_p = 0.01\gamma_p$ and $r_{i,i+1} = \lambda_p$. (Figure taken from [69])

#### 3.3.2.2 Rydberg-Rydberg interaction

Next, we focus on RRI atoms. The results are qualitatively comparable to DDI, and the interpretations are the same. However, Fig. 3.3 shows that $G^{(2)}$ has a very different structure as for the DDI case. From Fig. 3.3, detection regions can be identified in which $C_i = 0$ for $i \in \{2, 4\}$, such that 2- and 4-particle correlations can be measured directly and individually. Also, regions of large $C_3/G^{(2)} \gg 5$ exist, providing access to the 3-particle correlations.

## 3.4 Estimation of coincidence rates

We have evaluated the coincidence count rates of the fluorescence signal given by the linear chain of equidistant atoms for $n$-atom correlations. Basically, the fraction of relevant solid angle should provide with the count rate of photons falling upon a detector. However, this is true only if the intensity is distributed uniformly over the entire detection plane. This is, however, not the case since there is orders of magnitude difference between the minimum and the maximum values of the intensity over the whole detection range. This spatial variation of intensity is much more prominent in the dipole-dipole interaction (DDI) case compared to the Rydberg-Rydberg interaction (RRI) case. Therefore, in order to compute the intensity of light from the interesting contours one has to look exactly along the contour lines for the $n$-atom correlations.

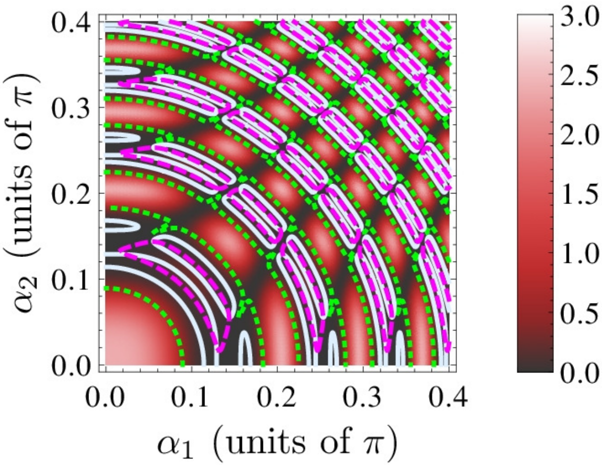

Figure 3.3: (Color online) Detection positions in which $n$-atom correlations can directly be measured for Rydberg-Rydberg interacting atoms. The dotted green contour indicates $\mathcal{C}_2 = 0$, and the dashed magenta contour $\mathcal{C}_4 = 0$. In these directions, $G^{(2)}$ is solely due to 2-atom or 4-atom correlations, respectively. The solid light blue contour shows $\mathcal{C}_3/G^{(2)} = 5$, such that 3-atom correlations dominate. The background shows $G^{(2)}$. Parameters are $\Omega_p = 0.01\gamma_p$, $\Omega_c = \gamma_p$, $\gamma_c = 0.05\gamma_p$, $C_6 = 2\pi \times 50\text{GHz}\ \mu\text{m}^6$, and $r_{i,i+1} = 5\lambda_p$. (Figure taken from [69])

Before doing that, we need to define the detection plane. Eq. (3.8) fixes our atoms to the $z$ axis if the detection vector $\vec{k}_i$ is written as

$$\vec{k}_i = k_i\{\sin(\alpha_i)\cos(\beta_i), \sin(\alpha_i)\sin(\beta_i), \cos(\alpha_i)\}, \tag{3.12}$$

where $\beta_i$ is the azimuthal angle perpendicular to the plane containing the atoms for the $i$th detector. Let us assume the propagation vector of the laser to be directed along the $x$ direction, perpendicular to the line of atoms. The detection is carried out in the $x$-$z$ plane, that is, $\alpha_i \in \{0, \pi\}, i \in \{1, 2\}$.

Now we outline the contours for the $n$-atom correlations by identifying the angular regions around them. We divide the complete detection plane into a fine grid. Each element of the two-dimensional square grid has a width of $\pi/1000$. In total we have $10^3 \times 10^3$ grid elements. We apply several checks in order to make sure that the size of our grid element is small enough to recover the interesting contours completely. For example, we approximate the total intensity in the plane using the grid.

For an anisotropic source, as is the case of mutually interacting atoms, the total intensity in the plane at one of the detectors positioned at an angle $\alpha$ is given by

$$\int_0^\pi I(\alpha)d\alpha. \tag{3.13}$$

For two detectors, we have the total intensity

$$\prod_{i=1}^{2}\int_0^\pi I(\alpha_i)d\alpha_i = \sum_{i,j} I(\alpha_i)\Delta_{ij}, \tag{3.14}$$

where $\Delta_{ij}$ is the area of a grid element. We make sure that the percentage error in the results obtained from each side of Eq. (3.14) is negligible.

As one can see from Figs. (3.2) and (3.3), in both DDI and RRI cases, apart from $\mathcal{C}_2 = 0$, at many points lines of contour of $n$-atom correlation cross the contour lines corresponding to of $m$-atom correlation, where $n \neq m$, $n > 2$, $m > 2$. These points correspond to the detection directions that are special in the sense that they provide more information than the ones where no overlap is present. If at a point the contour lines of $\mathcal{C}_n = 0$ as well as $\mathcal{C}_m = 0, n \neq m$ are present, this means that at this very point $G^{(2)} = G_n - U_n = G_m - U_m$, which enables the direct detection of $n$ as well as $m$-atom correlations. If contour lines of $\mathcal{C}_n = 0$ are overlapped by $\mathcal{C}_m >> G^{(2)}$, one still detects only scattered light containing $n$-atom correlations, however, in addition, there is an information that at that point $-G_m + U_m >> 0$.

As mentioned earlier, two types of criteria for the identification of atomic correlations can be deduced from Eq. (3.11). The stronger one is given by $\mathcal{C}_n = 0$. For the numerical computation, we have approximated it by $|\mathcal{C}_n/G^{(2)}| < \epsilon$, where $\epsilon$ is a small number which is chosen very carefully such that essentially only the entire contour can be mapped. In many cases, if $\epsilon$ is slightly increased, some undesired points appear that are not present on the actual contour.

The other criterion, which is an indication of the presence of atomic correlations and is somewhat lighter demands that $\mathcal{C}_n/G^{(2)} >> 1$. In [69], $\mathcal{C}_n/G^{(2)} = P$, where $P \in \{5, 10\}$ for the RRI and the DDI cases, respectively has been used in order to make a clear presentation. We approached it numerically by utilizing the condition $\mathcal{C}_n/G^{(2)} \geq P$. This numerical approach results in the filling of the relevant contours in such a way that the overlap with other contours increases. This way we are able to distinguish the interesting grid elements where the atomic correlation exists from the uninteresting ones and cover the relevant contour completely. Now, in principle, one can integrate the intensities at the two detectors over every such small grid element and sum up the result to get the total intensity coming from the interesting contours. We checked again via the numerical integration using Boole command in Mathematica and found that the two results were consistent. This again confirms that the grid element size is well-chosen.

The next step is to deduce the count rate from the total intensity. For that, we proceed from the two dimensional case. A point source (scattering atom) is positioned along the $z$-axis and the detection is restricted to be carried out only along the polar angle which ranges from 0 to $\pi$. The total planar angle is given by $\int_0^\pi d\alpha = \pi$. Suppose $\mathcal{R}_{1,tot}$ denotes the total number of photons per second emitted by the atom in the plane. If the source emits photons isotropically, then in a single detector collecting photons from an angular range $d\alpha$, the number of photons (count rate) that will be received in a second is given by $\mathcal{R}_{1,tot} * d\alpha/\pi$.

$\mathcal{R}_{1,tot}$ can be written in terms of total intensity, $I_{1,tot}$ due to a single scattering atom in the complete planar angle as

$$\mathcal{R}_{1,tot} = \xi I_{1,tot}, \tag{3.15}$$

where $\xi$ is a proportionality constant. Now the number of photons per second striking a detector of size $d\alpha$ placed in the direction $\alpha$ is given by

$$\mathcal{R}_1(\alpha)d\alpha = \xi I_1(\alpha)d\alpha, \tag{3.16}$$

where $\mathcal{R}_1(\alpha)$ is a fractional photon count rate of $\mathcal{R}_{1,tot}$ that impinges on the detector. Dividing Eq. (3.16) by Eq. (3.15), one obtains

$$\mathcal{R}_1(\alpha)d\alpha = \mathcal{R}_{1,tot}\frac{I_1(\alpha)}{I_{1,tot}}d\alpha. \tag{3.17}$$

If instead of a single atom there are $N$ atoms having parallel dipoles, interference effects arise. The scattered intensity is an interference pattern having maxima and minima. The total intensity and the total scattering rate from all $N$ atoms are denoted by $I_{N,tot}$ and $\mathcal{R}_{N,tot}$, respectively. We have

$$I_{N,tot} = \int_0^\pi G^{(1)}(\alpha)d\alpha, \tag{3.18}$$

here $G^{(1)}(\alpha)$ is given by Eq. (3.5a). Again, we can write

$$\mathcal{R}_N(\alpha)d\alpha = \mathcal{R}_{N,tot}\frac{G^{(1)}(\alpha)}{I_{N,tot}}d\alpha, \tag{3.19}$$

where $\mathcal{R}_N(\alpha)$ is the count rate produced by $N$ scatterers corresponding to a photo detector placed at an angle $\alpha$, respectively.

Finally, if instead of a single detector, one has two detectors situated at polar angles $\alpha_1$ and $\alpha_2$ having sizes $d\alpha_1$ and $d\alpha_2$, respectively, the differential form of the product of count rates is given by

$$\mathsf{C}_{prod}(\alpha_1,\alpha_2)d\alpha_1 d\alpha_2 = \mathcal{R}_N(\alpha_1)\mathcal{R}_N(\alpha_2)d\alpha_1 d\alpha_2, \tag{3.20}$$

The corresponding total product of count rates registered at the two detectors is thus given by integrating the above equation over the total spread of the two detectors. To be explicit,

$$\mathbf{C}_{prod} = \frac{\mathcal{R}^2_{N,tot}\sigma^2}{I^2_{N,tot}}\int_{\det_1}\int_{\det_2} G^{(1)}(\alpha_1)G^{(1)}(\alpha_2)d\alpha_1 d\alpha_2, \tag{3.21}$$

where $\mathbf{C}_{prod} = \int_{\det_1}\int_{\det_2}\mathsf{C}_{prod}(\alpha_1,\alpha_2)d\alpha_1 d\alpha_2$ is the product of the count rates at the two photon sensors. $\sigma$ is the efficiency of the detectors which is less than unity. $\det_i$ is an abbreviation for $i$th detector.

In order to compute not the product of two independent count rates at the two detectors but the coincidence signal, the product intensities $G^{(1)}(\alpha_1)G^{(1)}(\alpha_2)$ in Eq. (3.21) must be replaced by $G^{(2)}(\alpha_1,\alpha_2)\tau_{coh}$, where $\tau_{coh}$ is the coherence time of light and is given by the inverse of the spontaneous decay rate of the atoms. The reason is that the product of the intensities can be non-zero even if one of the detectors has made a click but the other one has not been hit by a photon within a small interval of time given by $\tau_{coh}$. On the other hand, $G^{(2)}(\alpha_1,\alpha_2)$ takes into account the correlations among the scattered light and is non-zero only for nearly simultaneously detected photons.

Thus Eq. (3.21) can be utilized to yield the coincidence count rate **C** in the following way.

$$\mathbf{C} = \frac{\mathcal{R}^2_{N,tot}\sigma^2}{I^2_{N,tot}} \int_{\mathrm{det}_1} \int_{\mathrm{det}_2} G^{(2)}(\alpha_1, \alpha_2) d\alpha_1 d\alpha_2 \tau_{coh}. \tag{3.22}$$

So far, all the focus had been on the plane containing the atoms. However, the photo detection is performed with a two-dimensional chip of a photo detector. So now, we have to take into account also the angle perpendicular to the plane containing the atoms, which is the angle $\beta_i$. Again, for an isotropic source, the count rate registered at a detector of size $d\Omega$ is given by total emission rate of the source times $d\Omega/(4\pi)$. However, we know that the sources that we consider, i.e., interacting atomic dipoles which are assumed to be orthogonal to the inter atomic axis do not radiate identically in all directions even if they are placed symmetrically along the $z$ axis around the origin. Therefore, it is important to check how the results that we have presented so far will change if the detection is carried out in space. The first place where the effect of the angle $\beta_i$ comes is Eqs. (3.5). For this purpose, one should start with the total electric field operator evaluated at the position of the detector(s) and derive the first and second order correlation functions taking care of all the multiplicative prefactors and without confining the detection process to any plane. This calculation has already been done in [20] so here we write down the end result for the first and the second order correlation functions.

$$G^{(1)}(\vec{R}_1) = v(\vec{R}_1) \sum_{i,j} \sqrt{\gamma^{(ii)}\gamma^{(jj)}} \langle A^{(i)}_{eg} A^{(j)}_{ge} \rangle e^{i\vec{k}_1.\vec{r}_{ij}}, \tag{3.23a}$$

$$G^{(2)}(\vec{R}_1, \vec{R}_2) = v(\vec{R}_1) v(\vec{R}_2) \sum_{i,j,k,l} \sqrt{\gamma^{(ii)}\gamma^{(jj)}\gamma^{(kk)}\gamma^{(ll)}} \langle A^{(i)}_{eg} A^{(j)}_{eg} A^{(k)}_{ge} A^{(l)}_{ge} \rangle e^{i\vec{k}_1.\vec{r}_{il} + i\vec{k}_2.\vec{r}_{jk}}, \tag{3.23b}$$

where $v(\vec{R}_i)$ is the radiation pattern of a linear dipole moment given by

$$v(\vec{R}_i) = \frac{3\hbar\omega_0}{16\pi\epsilon_0 c R_i^2} \sin^2\psi_i, \tag{3.24}$$

if one assumes all the dipole moments to be parallel such that all of them make the same angle $\psi_i$ with the observation vector $\vec{R}_i$. $R_i$ is the distance of the $i$th detector from the atomic array.

$$\gamma^{(ii)} = \frac{\omega_i^3 |\vec{d}_i|^2}{3\pi\epsilon_0 \hbar c^3}. \tag{3.25}$$

Using the typical values of optical frequencies, that is, $\omega_i \approx 3 * 10^{15}/s$, usual dipole moment $|\vec{d}_i| = 3.3 * 10^{-30} Cm$, $\epsilon_0 = 8.85 * 10^{-12} C^2/(Nm^2)$, $\hbar = 6.63 * 10^{-34} Nms/(2\pi)$ and $c = 3 * 10^8 m/s$, Eq. (3.25) yields $\gamma^{(ii)}$ ~MHz.

Since the dipole moments are assumed to be orthogonal to the inter atomic distance vector, we assume that they are aligned along the $y$ direction. Fig. (3.4) explains the coordinate system pictorially.

Now we have to relate the angle $\psi_i$ to the spherical polar angles $\alpha_i$ and $\beta_i$. By definition $\vec{d}.\vec{k}_n = |\vec{d}||\vec{k}_n| \cos(\psi_n)$. Using Eq. (3.12), one finds $\vec{d}.\vec{k}_n = |\vec{d}||\vec{k}_n| \sin(\alpha_n)\sin(\beta_n)$. This

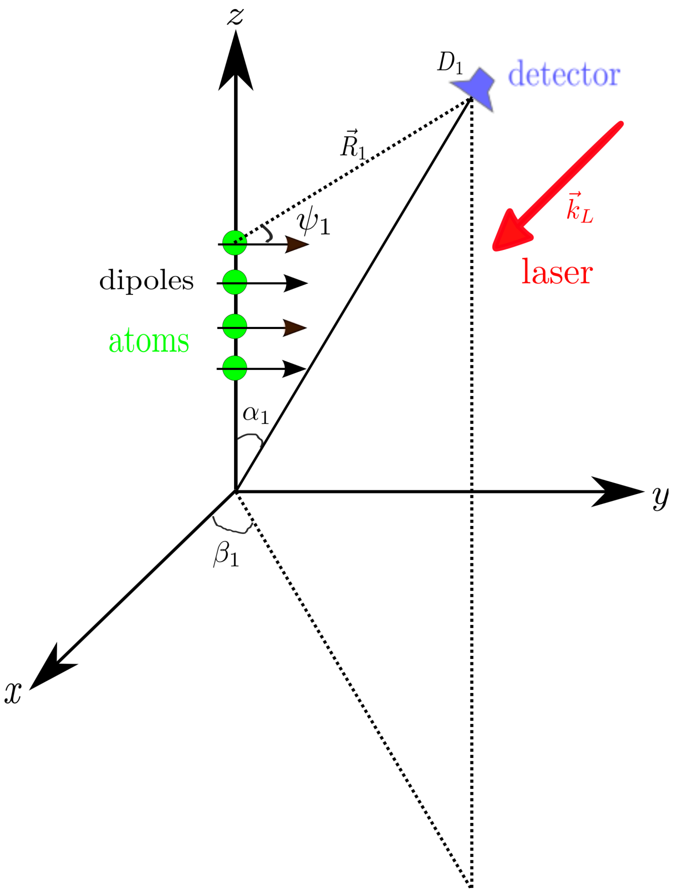

Figure 3.4: (Color online) coordinate system specifying $z, y, x$ axes as the alignment directions of atomic array (green blobs), dipole moments (parallel black arrows) and the incident resonant laser field (thick red arrow), respectively. Angles $\psi_1, \alpha_1, \beta_1$ are the angles between the orientation of the dipole moments and the detector $D_1$, the inter atomic distance vector and the detector $D_1$, the $x$-axis and the projection of detector $D_1$, respectively.

means that the angle $\psi_i = \cos^{-1}(\sin(\alpha_i)\sin(\beta_i))$. It is evident now that apart from the constant factors, the variation in the correlation functions comes from the prefactor $\sin^2(\cos^{-1}(\sin(\alpha_i)\sin(\beta_i)))$.

Let us make a few checks in order to understand the relationship among $\psi_i, \alpha_i$ and $\beta_i$.

- For $\psi_i = 0$, the dipole radiation pattern vanishes. This is to be expected since in this case the detection apparatus is placed parallel to the dipoles and the dipoles do not radiate along their optical axes. In this case $\alpha_i = \beta_i = \pi/2$.
- For $\psi_i = \pi$, the detector is placed anti parallel to the dipoles. Again this is a detection position where no radiation enters the detector. This direction is given by $\alpha_i = \pi/2$ and $\beta_i = 3\pi/2$.
- $\psi_i = \pi/4$ gives $\sin(\alpha_i)\sin(\beta_i) = 1/\sqrt{2}$. This choice of $\psi_i$ renders either the $xy$ plane for which $\alpha_i = \pi/2, \beta_i = \pi/4$ or the $yz$ plane for which $\alpha_i = \pi/4, \beta_i = \pi/2$.

- $\psi_i = \pi/2$ implies $\sin(\alpha_i)\sin(\beta_i) = 0$ and gives $xz$ plane. This is the value of $\psi_i$ that has been considered initially such that $\sin^2(\psi_i)$ evaluated to unity, which means that at the $xz$ plane, the radiation from the dipoles is maximum.

The exponential factors in Eqs. (3.23) are still given by Eq. (3.8).

Having settled that the only change in our results will be given by a constant prefactor multiplied by $\sin^2(\psi_i)$, we can proceed toward calculating the coincidence rate employing realistic detection in the 3 dimensions.

The total intensity in the whole solid angle of $4\pi$ due to all atoms is given by

$$\begin{aligned} I'_{N,tot} =& \int_0^{2\pi}\int_0^{\pi} G^{(1)}(\vec{R}_1)\sin(\alpha_1)d\alpha_1 d\beta_1 \\ =& 2\pi v(\vec{R}_1)\sum_{i,j}\sqrt{\gamma_i\gamma_j}\langle A^{(i)}_{eg}A^{(j)}_{ge}\rangle \int_0^{\pi} e^{i(2\pi/\lambda)|\vec{r}_{ij}|\cos(\alpha_1)}\sin(\alpha_1)d\alpha_1 d\beta_1 \\ =& 4\pi v(\vec{R}_1)\sum_{i,j}\sqrt{\gamma_i\gamma_j}\langle A^{(i)}_{eg}A^{(j)}_{ge}\rangle \frac{\sin((2\pi/\lambda)|\vec{r}_{ij}|)}{(2\pi/\lambda)|\vec{r}_{ij}|}, \end{aligned} \tag{3.26}$$

where $G^{(1)}(\vec{R}_1)$ is given by Eq. (3.23a). The total count rate emitted by a source in the solid angle $4\pi$ is

$$\mathcal{R'}_{N,tot} = \chi I'_{N,tot}, \tag{3.27}$$

where again $\chi$ is a constant of proportionality.

Now the differential count rate in a detector of dimensions $d\Omega$ located at the polar angle $\alpha$ and the azimuthal angle $\beta$ can be written as

$$\begin{aligned} \mathcal{R'}_N(\alpha,\beta)d\Omega =& \chi\, G^{(1)}(\vec{R})d\Omega \\ =& \chi\, G^{(1)}(\vec{R})\sin(\alpha)d\alpha\, d\beta \\ =& \frac{\mathcal{R'}_{N,tot}}{I'_{N,tot}}\, G^{(1)}(\vec{R})\sin(\alpha)d\alpha\, d\beta. \end{aligned} \tag{3.28}$$

As before, the product of the two independent count rates for two detectors positioned at $\{\alpha_1,\beta_1\}$ and $\{\alpha_2,\beta_2\}$ is given by

$$\mathbf{C}'_{prod} = \frac{\mathcal{R'}^2_{N,tot}\,\sigma^2}{I'^2_{N,tot}}\int_{\det_1}\int_{\det_2} G^{(1)}(\vec{R}_1)G^{(1)}(\vec{R}_2)\sin(\alpha_1)\sin(\alpha_2)d\alpha_1 d\alpha_2 d\beta_1 d\beta_2. \tag{3.29}$$

In order to ensure a coincidence detection, the product $G^{(1)}(\vec{R}_1)G^{(1)}(\vec{R}_2)$ in Eq. (3.29) will be replaced by $G^{(2)}(\vec{R}_1,\vec{R}_2)\tau_{coh}$.

where

$$\begin{aligned} G^{(2)}(\vec{R}_1,\vec{R}_2) &= G^{(2)}(\alpha_1,\alpha_2,\beta_1,\beta_2) \\ &\equiv G^{(2)}(\alpha_1,\alpha_2)\ \sin^2(\psi_1)\ \sin^2(\psi_2) \\ &= G^{(2)}(\alpha_1,\alpha_2)\ (1-\sin^2(\alpha_1)\sin^2(\beta_1))\ (1-\sin^2(\alpha_2)\sin^2(\beta_2)). \end{aligned} \tag{3.30}$$

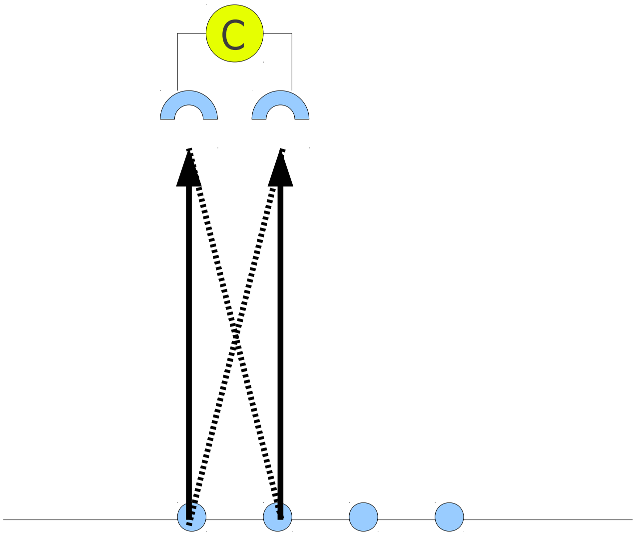

Figure 3.5: (Color online) set up for experimental coincidence photo detection in the near field to measure spatial correlations. There are two possible interfering pathways shown by solid and dotted lines for a joint detection of the scattered light coming from any pair of atoms.

An experimental scheme to measure same-time second order spatial correlation functions in the near field is shown in Fig. (3.5). We, however, utilize detection in the far-field, which is also based on the same principle.

Finally, Eq. (3.29) takes the following form

$$\mathbf{C}' = \frac{\mathcal{R}'^{2}_{N,tot}\,\sigma^2\,\tau_{coh}}{I'^{2}_{N,tot}} \int d\alpha_1 \int d\alpha_2\, G^{(2)}(\alpha_1,\alpha_2)\ \sin(\alpha_1)\ \sin(\alpha_2) \times \int d\beta_1(1-\sin^2(\alpha_1)\sin^2(\beta_1)) \int d\beta_2(1-\sin^2(\alpha_2)\sin^2(\beta_2)). \tag{3.31}$$

We propose to collect the scattered signal from the atoms with the help of two Electron Multiplying Charged-Coupled Device (EMCCD) cameras. We use the specifications of **EMCCD iXon 3 888** for our numerical computations. These single photon detectors have a square sensor chip of side length 13.3mm and 1024 × 1024 active pixels. One can calculate that the side length of a pixel is 13.3mm/1024 = 13$\mu$m, see Fig (3.6). The angle $\phi$ provides with the numerical aperture whereas the resolution (or the magnification) is determined by the angle $\theta$.

$$\theta = \tan^{-1}\left(\frac{13\mu\text{m}/2}{R_1}\right). \tag{3.32}$$

We want the light from every grid element to be encoded on a single cell or unit magnifi-

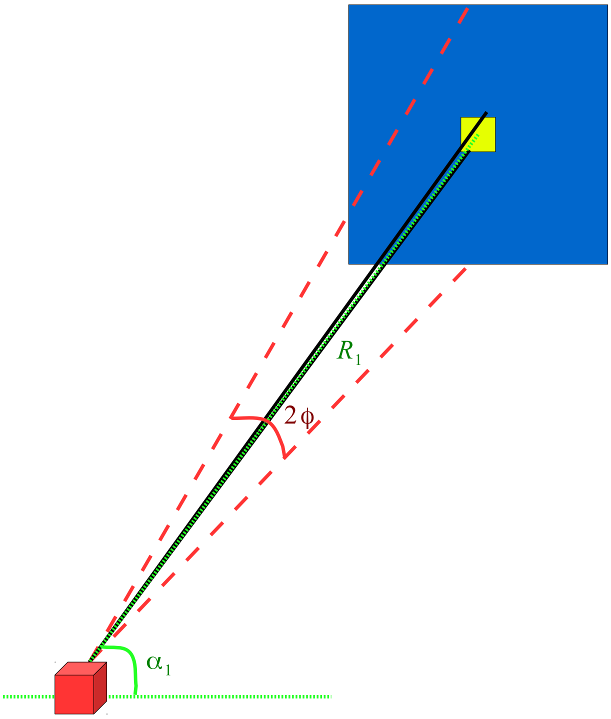

Figure 3.6: (Color online) set up for photo detection. The red box represents the vacuum chamber containing the scattering atoms and the blue square represents the 2-dimensional front of a camera. One yellow pixel at the center is shown. The red dashed lines, green dotted lines and the black solid lines show the angle $2\phi$ covered by the detector sensor, the angle $\alpha_1$ that the detector makes with the atomic chain and the small angle $2\theta$ covered by one pixel at the sensor surface.

cation. Therefore, we must set

$$\begin{aligned} 2\theta &= \text{width of a grid element} \\ \Rightarrow 2\tan^{-1}\left(\frac{13\mu\text{m}/2}{R_1}\right) &= \frac{\pi}{1000} \end{aligned} \tag{3.33}$$

From the above equation, $R_1$ comes out to be 4.14mm. Using this value of $R_1$, one can determine the image area covered by the detector as

$$\phi = \tan^{-1}\left(\frac{13.3\text{mm}/2}{R_1}\right) = 0.323\pi. \tag{3.34}$$

Since the chip of the detector collects light from the angle $2\phi$, the range of the polar angle in the equator covered by the detector chip is $0.646\pi$. Since the sensor chip is a square, the same range of planar angle is covered along the azimuthal angle.

The interesting contours are most narrowly spaced around $\alpha_i = \pi/2$, therefore, we place the detector at this point and thus cover a range of $\alpha_i$ from $\pi/2 - 0.646\pi/2$ to $\pi/2 + 0.646\pi/2$. For $\beta_i$, the radiation pattern is maximum at $\beta_i = 0$, so the detector is placed to cover a range of $\beta_i$ from $0.646\pi/2$ to $0.646\pi/2$.

**DDI case**

| | $N=3$ | $N=4$ | $N=5$ | $N=6$ |
|---|---|---|---|---|
| $I'_{N,tot}$ | $8.7*10^{-3}$ | $9.2*10^{-3}$ | $9.6*10^{-3}$ | $1*10^{-2}$ |
| criterion | coincidence count rate $\mathbf{C}'$ | | | |
| $\lvert\mathcal{C}_2/G^{(2)}\rvert < 1/10$ | 1158 | 1462.64 | 1823.2 | 2078.6 |
| $\lvert\mathcal{C}_3/G^{(2)}\rvert < 1/10$ | | | 151.86 | 198.2 |
| $\lvert\mathcal{C}_4/G^{(2)}\rvert < 15/100$ | | 192.142 | 1704.4 | 2005.84 |
| $\mathcal{C}_3/G^{(2)} \geq 10$ | 1809 | 3043.82 | 4254.66 | 8467.81 |
| $\mathcal{C}_4/G^{(2)} \geq 10$ | | 969.94 | 734.617 | 831.21 |

Table 3.1: Total intensity, criteria for the distinguishing the contour lines and coincidence count rate for 3, 4, 5 and 6 DDI atoms

The total solid angle covered by the detector is calculated as

$$\int_{-0.646\pi/2}^{0.646\pi/2} d\beta \int_{\pi/2-0.646\pi/2}^{\pi/2+0.646\pi/2} \sin(\alpha)d\alpha = 1.097\pi \tag{3.35}$$

This means that about 27% of the fluorescent light coming from the solid angle of $4\pi$ can be collected by the EMCCD if it is placed about 4mm away from the atomic chain.

We integrate Eq. (3.31) over every grid element in the $\alpha$ range using the same $\beta$ range and sum up the result.

We have checked via numerical calculations using the same detection apparatus that the interesting structures related to the $n$-atom correlations survive for $N \in \{3,5,6\}$ (for DDI case) and $N=3$ (in the RRI case). It is expected that one will still find them if $N$ is changed to other values. The computation of steady sate density matrix for larger number of atoms becomes difficult due to the memory shortage.

We have used the ideal count rate of a million photons per second as $\mathcal{R}'_{N,tot}$, $1\mu$s as $\tau_{coh}$, $\sigma$ as 60%.

The values for the coincidence count rate for DDI case are tabulated in table (3.1). Expectedly, the total intensity $I'_{N,tot}$ given by Eq. (3.26) increases by increasing the number of scatterers in the chain. For $N=3$ the contour lines do not overlap or cross each other. For 5 and 6 DDI atoms. However, contrary to the case of 4 atoms discussed so far, the contours corresponding to $\mathcal{C}_3 = 0$ are also obtained, which means that for 5 and 6 DDI atoms, there exist detection directions where 3-atom correlation can also be directly accessed. Moreover, these contour lines overlap at many directions with $\mathcal{C}_2 = 0$ contour lines. This is another contradiction compared to the 4 atom situation where the contour lines corresponding to $\mathcal{C}_2 = 0$ are never interrupted by any other contour lines. Fig. (3.7) plots the DDI atoms data on a logarithmic scale. One can see that the total intensity as well as the signal size for various $n$-atom correlations go on increasing almost linearly as the number of atoms increases. For contours related to $\mathcal{C}_4$, however, the behavior is not decisive.

The data for RRI case has been shown in table (3.2). The values for coincidence count

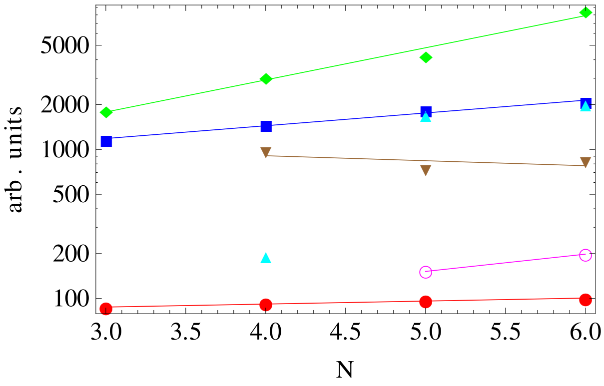

Figure 3.7: (Color online) Logarithmic plot of total intensity (multiplied by a factor of $10^4$) and coincidence count rate for DDI plotted versus the number of atoms. The red blobs show the total intensity at the two detectors. The blue squares, magenta circles, cyan triangles facing upwards represent $\mathcal{C}_n = 0, n \in \{2, 3, 4\}$, respectively. The green rhombuses and brown triangles pointing downwards manifest the signal corresponding to $\mathcal{C}_n/G^{(2)} >> 1, n \in \{3, 4\}$, respectively.

rates at the right column in tables (3.1-3.2) in case of RRI are much better than in the DDI case because the interesting contour lines are very dense in the RRI case compared to the case of DDI. Opposed to the DDI case, here, signal size decreases from contours corresponding to $\mathcal{C}_2$ with an increment in the value of $N$, whereas, it increases, as for DDI atoms for contours related to $\mathcal{C}_3$.

It is interesting that if the system is reduced to two atoms, neither in case of DDI nor for RRI atoms, one finds contour lines corresponding to $\mathcal{C}_2 = 0$. It is clear that the coincidence count rate can be increased by using more efficient detectors. A decrease in the distances of the detectors from the atoms will increase the solid angle for the collection of the photons and resultantly increase the count rate of joint photo detection. Relaxing the criteria for outlining the interesting contours for $n$-atom correlations is going to increase the signal very significantly.

## 3.5 Summary

We have presented the mathematical foundations to estimate the coincidence count rate using the scheme proposed in [69]. We found that the coincidence count rate cannot simply be assessed from the solid angles because the scattered radiation is highly anisotropic. In [69], the results have been presented for detection in an equatorial plane. However, practical detectors work in three dimensional geometries, therefore, it is important to take into account the complete radiation pattren of the dipole moments in the first and second order spatial correlation functions. The numerical results show that any experiment to implement the scheme can be performed as the relevant directions for $n$-atom correlations provide with a sufficient count rate for the coincidence detection. Furthermore, we showed the results for different number of atoms in the chain configuration.

**RRI case**

| | $N = 3$ | $N = 4$ |
|---|---|---|
| $I'_{N,tot}$ | $1.87 * 10^{-4}$ | $2.5 * 10^{-4}$ |
| criterion | coincidence count rate $\mathbf{C}'$ | |
| $\|\mathcal{C}_2/G^{(2)}\| < 1/10$ | 167749 | 74394 |
| $\|\mathcal{C}_4/G^{(2)}\| < 15/100$ | | 58659 |
| $\mathcal{C}_3/G^{(2)} \geq 5$ | 332126 | 454856 |

Table 3.2: Total intensity, criteria for the distinguishing the contour lines and coincidence count rate for 3 and 4 RRI atoms

## 3.6 Outlook

- A direct extension of this work will be to exploit high values of $N$, the number of atoms in the linear chain. This will not only provide with a higher scattered intensity but can also lead to the determination of scaling of the results with $N$ in a decisive way. One may then use higher order correlation functions too to observe the properties of the system.

  Since the numerical calculations become difficult because of the large dimensions of the system, in particular, for the RRI atoms, one can make use of the blockade effect. By computing the blockade radius, one can truncate the Hilbert space such that only one excitation can be contained within a blockade sphere.

- Instead of a regular arrangement of atoms, for several experimental set ups, arbitrary geometries for the atomic positions as well as for detector arrangements are required. One can optimize the detection directions or the position configurations of the atoms which make the experimental procedures simpler. Since completely arbitrary positions for the atoms and the detectors are difficult to simulate, one can try to fix $N-1$ of the atoms, allowing one atom to have arbitrary spatial degrees of freedom and then fix this atom to the position which provides, for example, with the maximum coincidence count rate.

- Whether the proposed method works with other mechanisms (other than DDI or RRI) to create correlations among particles can be verified.

# Chapter 4

# Detection of $n$-atom correlations via scattering in arbitrary geometries

The main results of this chapter will be written up in:
**Q. Gulfam** and J. Evers
*Detection of $n$-atom correlations via scattering in arbitrary geometries*

*An ensemble of four Rydberg atoms interacting with each other and driven resonantly by laser fields in arbitrary position geometries is considered. The scattered signal containing the information about the atomic correlations is detected. It is found that due to detection arrangements in certain directions, as the ensemble expands spatially, 3-particle correlations vanish even before 4-particle does. Two different ways have been used to understand the counter-intuitive result. It is found that for a large number of random atomic positions, the average results of $n$-atom correlations are not distinguishable. A complete understanding of the system, however, is yet to be developed.*

## 4.1 Introduction

Ensembles of three-level atoms having a ground state, an intermediate state and an excited state $|r\rangle$ of a high principal quantum number, called a Rydberg state have been studied widely in the recent past because of the exaggerated properties of such atoms. The most famous property associated with closely lying Rydberg atoms is that of the dipole blockade which is based on the shift of the resonance due to the dipole-dipole interaction between the atoms [67]. The blockade effect leads to an elimination of absorption of energy for all other atoms within the blockade radius, thus creating an optically controlled switch [160]. It can be used to study entanglement of neutral atoms that are at micrometers distances apart. The strong long-ranged interaction enables the development of quantum logic gates [161]. Due to the collective effects caused by the Rydberg Rydberg interaction, many body physics can be studied [66].

Usually the experiments rely on cooling, trapping, manipulating and detecting single Rydberg atoms [162] in various spatial geometries, for example, regular optical lattices or cylinderical geometries etc. In order to simulate a true real behavior of a gas of frozen Rydberg atoms, it is necessary to consider the atoms in relative arbitrary orientations and distances. Laser cooling techniques decelerate the atoms of a gas inside vacuum such that the atomic motion can be neglected on an experimental time scale [163].

Throughout this chapter, we have only changed the atomic position coordinates. The other parameters such as the Rabi frequencies of the lasers etc are chosen exactly in the same way as in the last chapter.

## 4.2 Linear configuration

Until Ch. (3), we have mainly discussed the case of equidistant atoms. Interesting results are obtained if one allows the inter atomic separation between the atom chain to be different from each other.

As a first example, in the DDI case for non-equidistant atoms, one can find contour regions satisfying $\mathcal{C}_3 = 0$, which were so far not there. The atomic positions can be chosen as $\lambda\{1.6, 2.3, 3.25, 3.9\}$, for example. The presence of $\mathcal{C}_3 = 0$ contours is, however, not a trait restricted to non-equidistant, asymmetric positions of atoms. Such contours are also found if the atoms are placed regularly, for example, at positions like this, $\lambda\{0.5, 1.25, 2, 2.75\}$.

In the same position configuration, another interesting consequence of the changing the inter atomic separation from a full wave length can be observed. There are contours corresponding to $\mathcal{C}_3 = 0$ and $\mathcal{C}_4 = 0$, which means that there are detection directions in which 3 and 4-atom correlations can be achieved. However, contrary to the expectation, no contours for $\mathcal{C}_2 = 0$ are found. For regularly placed atoms, the probability of detecting 2-atom correlations out of all $n$-atom correlations is the maximum from $\mathcal{C}_2 = 0$ contour lines. One sees, however, various contours for $\mathcal{C}_2/G^{(2)} = 10$, which means that 2-atom correlations exist but there are no directions where they can be directly observed. Another example configuration for this effect is the position vector $\lambda\{0.01, 1.54, 2.63, 3.29\}$ of DDI atoms. In these and many other example configurations no $\mathcal{C}_2 = 0$ contours and $\mathcal{C}_3 \gg G^{(2)}$ contours are found. $\mathcal{C}_3/G^{(2)}$ usually ranges from very small positive (around 3) to very large negative values (less than $-30$). On the other hand, $\mathcal{C}_2/G^{(2)}$ usually ranges from slightly above zero to very large positive values ($\sim 10^2$). In short, for many atomic positions where one finds contours for $\mathcal{C}_2 = 0$, there are no contours for $\mathcal{C}_2 \gg G^{(2)}$. On the contrary, position arrangements of atoms that possess $\mathcal{C}_3 = 0$ contours contain no $\mathcal{C}_3 \gg G^{(2)}$ contours.

In case of RRI, contrary to DDI atoms, even for non-equidistant atoms again there are no $\mathcal{C}_3 = 0$ contours. Quite interesting is the position ket given by $\lambda\{5.8, 8.25, 17.95, 21.34\}$, where one only finds the green contour lines for $\mathcal{C}_2 = 0$. Contour lines corresponding to $\mathcal{C}_3 = 0, \mathcal{C}_3/G^{(2)} = 5, \mathcal{C}_4 = 0$ are totally absent. The reason for the absence of higher $n$-atom correlation can be understood from the magnitude of the RRI between different atoms. From table (4.1), one finds that the RRI between two pairs of different atoms is much

| $\{i,j\}$ | $V_{RR}(r_{i,j})$ |
|---|---|
| 1,2 | 168.337 |
| 3,4 | 23.98 |
| 1,3 | 0.011 |
| 2,4 | 0.007 |
| 2,3 | 0.044 |
| 1,4 | 0.002 |

Table 4.1: $V_{RR}$ between different atom pairs $\{i,j\}$ for position $\lambda\{5.8, 8.25, 17.95, 21.34\}$

larger than the interaction between any other pair. This is why there exist only 2-atom correlations between independent pairs of atoms and no higher $n$-atom correlation. This fact can be discovered by just looking at the positions of the atoms and considering that the $V_{RR}(r_{i,j}) \sim |r_{i,j}|^{-6}$. The distance between the 1st and the 2nd atom and that between the 3rd and the 4th atom is much smaller than the distance between the 2nd and the 3rd and that between 1st and the 4th atom. In this position setting, $U_3/G^{(2)} \approx U_4/G^{(2)} \approx 0$.

There are some position configurations, for example, $\lambda\{4.39, 14.79, 17.99, 21.85\}$ for which one finds many contour lines for $\mathcal{C}_2 = 0$ and $\mathcal{C}_3/G^{(2)} = 5$, negligibly small contours for $\mathcal{C}_4 = 0$ but no contours for $\mathcal{C}_3 = 0$. Once again, the explanation comes from the magnitude of RRI between different atoms, table (4.2). Now one can see that the inter atomic distance between atoms 2, 3 and 3, 4 is small compared to that between atoms 1 and 2 and therefore the RRI between the former pairs is much larger compared to the latter. This allows 3 atoms to interact contrary to the case mentioned previously. 4-atom correlation, however, is rare because of the negligible magnitude of RRI between atoms 1 and 2. In this position setting, again $U_3/G^{(2)} \approx U_4/G^{(2)} \approx 0$.

## 4.3 Arbitrary positions: RRI case

If DDI atoms are allowed to be in arbitrary geometries, in addition to the already discussed parallel dipole dipole couplings, also couplings between other orthogonal magnetic sublevels occur. This means that even if we choose the laser polarization in such a way that $m = 0$ atomic transition is driven, the population may be transferred to $m = \pm 1$ Zeeman levels due to the non-zero orthogonal dipole dipole couplings among these levels. The result is instead of a two-level atom, a four-level atom with one ground and three excited states has to be taken into account [164–166]. This implies that for four atoms, we have to consider 16 atomic levels and thus the system becomes 256 dimensional. This a too large to be handled numerically. Hence, we can only study arbitrary position configurations for the RRI case. In RRI case too, an $s$-state couples to all magnetic sublevels of the $p$-state. However, it turns out that the interaction energy is independent of the orientation of the atoms. Therefore, RRI atoms in $s$-state, despite having electrons in large $n$ shell, can be approximated by two-level atoms independent of their relative orientation. In general, for different angular momentum quantum numbers, this is not true [167].

| $\{i,j\}$ | $V_{RR}(r_{i,j})$ |
|---|---|
| 1,2 | 0.028 |
| 3,4 | 11.00 |
| 1,3 | 0.005 |
| 2,4 | 0.007 |
| 2,3 | 33.9 |
| 1,4 | 0.001 |

Table 4.2: $V_{RR}$ between different atom pairs $\{i,j\}$ for position $\lambda\{4.39, 14.79, 17.99, 21.85\}$

Let us consider the case of four Rydberg atoms in completely arbitrary position setups in the following. Obviously, the position vectors of the atoms given so far by $\vec{r_i} = |\vec{r_i}|\hat{z}$ need to be redefined. For arbitrarily located atoms, we define

$$\vec{r_i} = |\vec{r_i}|\{\sin\theta_i\cos\phi_i, \sin\theta_i\sin\phi_i, \cos\theta_i\}, \tag{4.1}$$

where $\theta_i$ and $\phi_i$ represent the spherical polar coordinates for the position of $i$th atom in the four particle ensemble.

As before, the atoms are driven by a laser fields polarized in the $\hat{x}$ direction whereas the dipole moments assumed to be parallel to each other are placed perpendicular to the laser in the $\hat{y}$ direction.

The exponential factors in the atom-laser interaction $V_L$ may no more evaluate to unity, hence, they have to be included explicitly.

$$V_L = \hbar\sum_i(\Omega_p A_{eg}^{(i)} e^{i\vec{k}_p.\vec{r}_i} + \Omega_c A_{re}^{(i)} e^{i\vec{k}_c.\vec{r}_i} + \text{H.c.})\,. \tag{4.2}$$

In the 3-dimensional analysis, we must take into account the dipole radiation pattern as we did in the last chapter. So, the first and second order correlation functions are given by Eqs. (3.23).

Eq. (3.8) modifies as written below.

$$\begin{aligned}\vec{k}_n\cdot\vec{r}_{ij} =& (2\pi/\lambda)\,.\vec{r}_{ij}\,\{\sin\alpha_n\cos\beta_n, \sin\alpha_n\sin\beta_n, \cos\alpha_n\}\\ =&(2\pi/\lambda)\big\{\sin\alpha_n\cos\beta_n(|\vec{r_j}|\sin\theta_j\cos\phi_j - |\vec{r_i}|\sin\theta_i\cos\phi_i) + \sin\alpha_n\sin\beta_n\\ &\times(|\vec{r_j}|\sin\theta_j\sin\phi_j - |\vec{r_i}|\sin\theta_i\sin\phi_i) + \cos\alpha_n(|\vec{r_j}|\cos\phi_j - |\vec{r_i}|\cos\phi_i)\big\}.\end{aligned} \tag{4.3}$$

### 4.3.1 Observables

The observables again are the first and second order correlation functions of the scattered light in three dimensions. They are given by Eqs. (3.23). As before, $G^{(2)}$ can be written as a sum of various $n$-particle contributions $G^{(2)} = \sum_{n=2}^{4} G_n$. $G_2$ is given by $G^{(2)}$ in such a way that out of all the atoms in the atomic ensemble only two are distinguishable. Therefore, out of the four summation indices in $G^{(2)}$, only two are different. Similarly, for

3-particle part $G_3$ of $G^{(2)}$, two out of the four indices in $G^{(2)}$ must be identical. Clearly, in $G_4$, all indices have to be distinct.

After a bit of simplification and rearrangement of the summation indices, these $n$-particle decompositions are explicitly given by

$$G_2 \propto \sum_{i,j} \langle A_{ee}^{(i)} A_{ee}^{(j)} \rangle [1 + e^{i(\vec{k}_1 - \vec{k}_2)\cdot \vec{r}_{ij}}]\,, \tag{4.4a}$$

$$G_3 \propto \sum_{i,j,k} \langle A_{ee}^{(i)} A_{eg}^{(j)} A_{ge}^{(k)} \rangle [e^{i(\vec{k}_1 + \vec{k}_2)\cdot \vec{r}_{jk}} + \sum_{n \neq m} e^{i\vec{k}_n \cdot \vec{r}_{ik} + i\vec{k}_m \cdot \vec{r}_{ji}}]\,, \tag{4.4b}$$

$$G_4 \propto \sum_{i,j,k,l} \langle A_{eg}^{(i)} A_{eg}^{(j)} A_{ge}^{(k)} A_{ge}^{(l)} \rangle e^{i\cdot \vec{k}_1 \vec{r}_{il} + i\vec{k}_2 \cdot \vec{r}_{jk}}\,. \tag{4.4c}$$

In the above set of equations, every summation is different from all others. This implies that $G_4$ does not contain $G_3$ or $G_2$.

With the replacement $\langle \cdot \rangle \to \langle \cdot \rangle_U$, all constituents of $U^{(2)} = U_2 + U_3 + U_4$ can also be written explicitly as in the following.

$$U_2 \propto NI^2 \sum_{i,j} [1 + e^{i(\vec{k}_1 - \vec{k}_2)\cdot \vec{r}_{ij}}]\,, \tag{4.5a}$$

$$U_3 \propto NIC \sum_{i,j,k} [e^{i(\vec{k}_1 + \vec{k}_2)\cdot \vec{r}_{jk}} + \sum_{n \neq m} e^{i\vec{k}_n \cdot \vec{r}_{ik} + i\vec{k}_m \cdot \vec{r}_{ji}}]\,, \tag{4.5b}$$

$$U_4 \propto NC^2 \sum_{i,j,k,l} e^{i\cdot \vec{k}_1 \vec{r}_{il} + i\vec{k}_2 \cdot \vec{r}_{jk}}\,, \tag{4.5c}$$

where $I = \langle A_{ee}^{(i)} \rangle$ and $C = |\langle A_{eg}^{(i)} \rangle|^2$. These equations are extremely helpful because they readily enable one to write the $n$-particle correlations $\mathcal{C}_n$ in a convenient way.

## 4.4 Planar configuration

Having performed these theoretical changes, we specialize for the case of the position configuration of the atoms such that $\phi_i, i \in \{1, 2, 3, 4\}$ is equal to zero. This confines the atoms to the $y - z$ plane. Next we choose $\theta_1 = 0, \theta_2 = \pi/2, \theta_3 = \pi, \theta_4 = -\pi/2$. Also, we assume all the atoms to have the same distance $r$ from the origin. Explicitly, the position vectors are written like this.

$$\begin{aligned} \vec{r}_1 &= \{0, 0, r\}, \\ \vec{r}_2 &= \{0, r, 0\}, \\ \vec{r}_3 &= \{0, 0, -r\}, \\ \vec{r}_4 &= \{0, -r, 0\}. \end{aligned} \tag{4.6}$$

To make the analysis simpler, for the detection purposes we arbitrarily fix $\beta_n$ to zero. This implies that we only detect the scattered light in the $x - z$ plane, where the dipole radiation pattern enumerates to unity.

We start the numerical investigations by setting $r$ to a small value and go on increasing it. For small distances from the origin, for example, At $r = \lambda$ or $5\lambda/2$, contours corresponding to the presence of all $n$-atom correlations, that is, $\mathcal{C}_2 = 0$, $\mathcal{C}_3/G^{(2)} = 5$, $\mathcal{C}_4 = 0$ and $\mathcal{C}_4/G^{(2)} = 5$ are found. Increasing $r$ to the value $5\lambda$ results in elimination of two out of four of these contours. Here, interesting contours corresponding to $\mathcal{C}_2 = 0$ and $\mathcal{C}_4/G^{(2)} = 5$ still exist, which means that in this spatially expanded system, 2- and 4-atom correlations persist, however, there are no 3-atom correlations. Intuitively, one would expect that as the inter particle separation is increased, 4-atom correlations should be the first to vanish. Further increase in $r$ should result in the extinction of 3-particle correlations and finally at very large $r$, 2-atom correlations are supposed to be eliminated, too. Separating the atoms even beyond, at $r = 15\lambda/2$, the atoms are uncorrelated such that no $n$-atom correlation contours are to be seen.

The counter-intuitive consequences found at $r = 5\lambda$ led to a deeper analysis. We have used two different ways to comprehend the systems' response.

### 4.4.1 $G_n$ analysis of the reduced system

We reduced the actual system of 4 atoms to 2 by taking into account the interactions between any two of the atoms and neglecting the other two atoms completely. This results in ${}^4P_2 = 4!/(4-2)! = 6$ permutations. In this case, $G^{(2)} = G_2$ and thus $\mathcal{C}_2 = G^{(2)} - G_2 + U_2 = U_2$. So $\mathcal{C}_2$ is always given by the uncorrelated part $U_2$. This means that a negligible Rydberg Rydberg interaction results in a large $\mathcal{C}_2/G^{(2)}$ for a system consisting of a pair of atoms.

The study of the system reduced to three particles is done in a similar way by considering the interactions between any three of the atoms. There are 24 possible different atomic arrangements given by the permutations ${}^4P_3 = 4!/(4-3)!$. From Eqs. (4.4), we notice that all components of the second order correlation function consist of a product of two parts: the first part is an expectation value of atomic operators, which is calculated from the steady state of the density matrix. The second part consists of various phase factors. We found with our numerical techniques that for these 24 arrangements of 3 atoms, the steady state can have only three different values. Exactly 8 arrangements correspond to one such value of the steady state. Therefore, within a set of 8 different permutations corresponding to the same steady state of the density matrix if there is a difference, that difference is attributed solely to the phase factors part. We further discovered that within such a set of 8 same steady state configurations, some contained $\mathcal{C}_3/G^{(2)} = 5$ contours while other did not. In fact, out of the 24 permutations, exactly 12 had 3-atom correlations while the remaining 12 had none, independent of the value of the steady state. This directed us to a more elaborated study of the phase factors rather than the steady state part. We found that those combinations that had an inter atomic distance vector along or perpendicular to the $z$ axis possessed 3-atom correlations, while those that had no such inter atomic distance vector had also no $\mathcal{C}_3 \gg G^{(2)}$. The picture can be understood by noting that for 3-atom correlations to occur, all three inter atomic distance vectors (which lie in $y-z$ plane) must have a non-zero projection on the detection vectors (which is carried out in $x-z$ plane). If two out of the three inter atomic distance vectors have non-zero scalar products with the detection vectors, this means that only two pairs of two atoms are correlated but 3 atoms, as a whole, are not. So, 2-atom correlations exist but 3-atom correlations do not. All 24 combinations have at least one separation vector proportional either to the $z$ axis or to the $y$ axis. Those having a vector in $y$ direction have $\vec{k}_n \cdot |\vec{r}_{ij}|\hat{y} = 0$, and therefore possess no correlated 3 atoms. This highlights the vital role played by the choice of the detection vectors in the determination of the behavior of the system. Had the detection vectors been chosen differently, there would be different results.

The true recognition of the system properties can, however, be done only from the full system of 4 atoms. We also analyzed all permutations for $G_4$. Again the total number of permutations is given by ${}^4P_4 = 24$. Nevertheless, now all 24 arrangements possess the same steady state as well as the same phase factors as in every permutation the same 4 atomic positions enter the summation. Therefore, all arrangements of $G_4$ lead to the same conclusion, that is, contours for $\mathcal{C}_2 = 0$ and $\mathcal{C}_4/G^{(2)} = 5$ are present but no contours relevant for 3-atom correlation are detected.

### 4.4.2 $\mathcal{C}_n$ analysis of the full system

We have also performed our analysis in a completely different way as follows, Using Eq. (3.11), $\mathcal{C}_n = (G^{(2)} - G_n) + U_n$. Also we have, $G^{(2)} - G_n = \sum_{m\neq n} G_m$. Using these two equations, one can write

$$\mathcal{C}_2 = G_3 + G_4 + U_2, \tag{4.7a}$$

$$\mathcal{C}_3 = G_2 + G_4 + U_3, \tag{4.7b}$$

$$\mathcal{C}_4 = G_2 + G_3 + U_4. \tag{4.7c}$$

Comparison of Eqs. (4.7b) and (4.7c) shows that the term $G_2$ is common in both of them. Via our numerical computations, we verified that $U_3/G^{(2)} \approx 0$ and also $U_4/G^{(2)} \approx 0$. Therefore, the main difference is accounted for by the terms $G_4$ and $G_3$. As the distance between the atoms is increased, first the four-atom part of $G^{(2)}$, i.e., $G_4$ decreases, which resultantly reduces the quantity $\mathcal{C}_3/G^{(2)}$. Therefore, $\mathcal{C}_3 \gg G^{(2)}$ contours are extinguished at $r = 5\lambda$. However, still at this $r$, $G_3$ is large enough to render $\mathcal{C}_4 \gg G^{(2)}$. Only if the distance is even further increased, e.g., $r = 15\lambda/2$, $G_3$ decreases too and makes $\mathcal{C}_4/G^{(2)}$ small.

$U_2$ which is the largest of all $U_n$ in Eq. (4.7a) is balanced by the sum of $G_3$ and $G_4$ in such a way that contours corresponding to $\mathcal{C}_2 = 0$ exist at $r = 5\lambda$.

This result that with increasing the inter atomic separation, $G_4$ decreases more than $G_3$ and $G_3$ decreases more than $G_2$ seems to be a general one. Hence, we checked it for other atomic geometries too.

A known example now is the case of linear chain of atoms, which is achieved by setting $\theta_i = 0$ in Eq. (4.1) such that all atoms are aligned along the $z$ axis, that is, $\vec{r}_i = |\vec{r}_i|\hat{z}$. For realizing an atomic chain, we set $|\vec{r}_i| = r$. At $r = 5\lambda$, $\mathcal{C}_2 = 0$, $\mathcal{C}_3/G^{(2)} = 5$, $\mathcal{C}_4 = 0$ contour lines are seen. As $r$ is increased to $8.95\lambda$, $9\lambda$ or $9.25\lambda$, again only contours related to $\mathcal{C}_2 = 0$ and $\mathcal{C}_4 = 0$ survive and no contours for the presence of $\mathcal{C}_3$ are found. Finally, at $r = 10\lambda$, contours associated with $\mathcal{C}_4$ also vanish and only $\mathcal{C}_2 = 0$ contours are located.

In order to check whether the result holds also for an irregular position configuration, we fix the atomic position coordinates as $\vec{r}_1 = \{0, 0, 0\}$, $\vec{r}_2 = \{0, 5/\sqrt{2}, 5/\sqrt{2}\}\lambda$, $\vec{r}_3 = \{0, 10, 0\}\lambda$ and $\vec{r}_4 = \{0, 15/2, 15\sqrt{3}/2\}\lambda$. Once again, contours related to $\mathcal{C}_2 = 0$ and $\mathcal{C}_4 = 0$ are found while no contours belonging to $\mathcal{C}_3$ are obtained.

## 4.5 Average dynamics

With our numerical calculations, we have calculated the values of different observables for various random spatial structures of four atoms and then calculated the expectation values of these observables. This corresponds to a simulation of a gas of 4 interacting atoms in which the atomic positions are not fixed. We found that when averaged over a large number of configurations, $\langle G^{(2)} \rangle \sim \langle \mathcal{C}_2 \rangle \sim \langle \mathcal{C}_3 \rangle \sim \langle \mathcal{C}_4 \rangle$. According to Eq. (3.11), this implies that $\langle U_n \rangle = \langle G_n \rangle$, which is also confirmed by the result of the numerical computation.

## 4.6 Summary

We have studied RRI atoms in various position setups. While a complete analysis employing completely arbitrary atomic geometries is yet to be performed, we discovered some interesting results regarding the orientation of the photo detectors. If a large number of random position arrangements of the atoms are considered, the interesting $n$-atom correlations cannot be distinguished.

## 4.7 Outlook

- One can employ detectors at arbitrary orientations and see how the results that we presented are affected. Specifically, instead of setting $\beta_n$ to zero, a range around zero should be included. A three dimensional detection is required which can also be achieved in an experiment.
- More atoms in the ensemble or higher $N$ as suggested in the outlook of the chapter (3) should be used.

# Summary

This research work is a study of quantum entanglement. Despite being a phenomenon that has been investigated for years but alludes physicists even today, entanglement can be used as a 'resource' in many important practical applications of the quantum theory. Tasks that are impossible to be carried out using classical resources, can be performed using entangled systems. Entanglement can be created, manipulated, distributed, detected and can also be destroyed. It does not carry the information itself, however, still can be used to establish communication between parties that are macroscopic distances apart. It has played a key role in the development of quantum computing and is of fundamental importance for quantum cryptography and many other applications. In this work, we have analyzed quantum entanglement in non-Markovian environments, resolution enhancement utilizing entangled sources of light and developed procedures to detect entanglement through scattered light using various model systems.

In the first part, entanglement has been studied in systems that possess retardation effects. We have considered a system of identical two-level atoms inside an ideal multi mode unidimensional ring-cavity. Entanglement can be created between the atoms via interaction with the cavity field. Retardation effects become pronounced when the atomic states are coupled simultaneously to many modes of the field. The parameters are selected in such a way that atomic decay as well as the cavity losses can be ignored. Using time-dependent Schrödinger's equation, the probability amplitudes have been calculated for both cases, that is, when the system contains a single excitation and when two photons are allowed to reside inside the cavity. Not only the populations of the two atoms are affected due to the presence of retardation effects but also the entanglement between them. The atomic entanglement has been measured using concurrence. Clear signatures of retardation are visible in the time evolution of concurrence. At short intervals of time given by a few iterations of the photon between the atoms and the cavity walls, an obvious periodic evidence of retardation is found. The retardation effects change the system dynamics not only at large inter atomic distances but also at sub-wavelength separations. We have taken into account short-time as well as long-time dynamics of concurrence. The presence of retardation does not only affect the dynamics quantitatively but also quantitatively. For example, there are conditions for which there is no entanglement without retardation and the presence of retardation induces entanglement and vice versa. Moreover, interesting effects like sudden death, sudden birth and revival of entanglement that can be observed in the double excitation case can also be modified by retardation. In particular, for some inter atomic separations, an initially entangled system never experiences sudden death but for other distances entanglement dies even if all other parameters remain unchanged. As an outlook, we propose that instead of assuming fixed atoms at definite positions, one should treat them to be confined in a trap such that a little movement of the atom inside the trapping well can be taken into account in the numerical simulations.

In the next part, resolution enhancement based on entanglement is considered. Non-classical sources of light (with entangled photons) having an effective wavelength which is much smaller than the wavelength of a single photon can be exploited to surpass the Rayleigh diffraction limit. Quantum lithography relies on the absorption of multi photons. Reliable multi photon detection is quite challenging in an experiment. Optical centroid measurements use arrays of single photon detectors. The detectors are so small that there is a very low probability of multi photon detection. The scheme works by noting the position of the detector that absorbed a photon and enumerating the centroid. The measurements are repeated several times since a distribution of the centroid is required. We have employed 'numerical experiments' to analyze the proposal. We have developed techniques to randomly generate events as positions of the photons from the incident non-classical wave function. Using a large number of such random numbers, we could reconstruct the centroid probability distribution. We have characterized the error in the measurement by root mean square(rms) deviation. The resolution enhancement with an increase in the number of entangled photons in the impinging state is verified. For different non-classical states, we have studied the rms deviation as a function of the detector size. As expected, only small detectors are suited better for the detection purpose, however, these detectors also correspond to numerical fluctuations in the measurement. We have exploited two different methods in order to simulate the detection in an experiment and have explained the results with both methods. Using our numerical data, we could develop methods to study multi photon absorption, required for quantum lithographic techniques, for various states and parameters in dependence of the size of the detector. For future research, we suggest the development of a method by which more than two photons can be detected from the correlated cat states such that the results with different number of photons can be compared.

The third part is a study of an atomic system in which correlations are created by either dipole-dipole interaction or Rydberg-Rydberg interaction. The system which is an atomic linear chain is driven resonantly by light fields and the scattered intensity is recorded as a function of detection directions. It is found that the higher order correlation functions can be decomposed such that the correlations among various number of atoms can be identified. Moreover, the scattered light contains the information about the different individual $n$-atom correlations imprinted on it. However, the fluorescent signal is highly anisotropic because of the interactions among the atoms. We have developed the necessary mathematical formalism to estimate the coincidence count rate from the relevant directions that highlight these individual atomic correlations. We found that a count rate large enough for an experimental implementation is obtained. We also estimated the total intensity and the count rate for various atomic correlations as a function of the number of atoms with a realistically modeled detection system. A direct extension of the work can be to use an even larger number of atoms in the array. To fix the increased simulation time and memory problem, one can utilize the blockade effect to truncate the Hilbert space in case of RRI such that only one excitation is possible within a blockade radius.

Later, we have allowed the atoms to acquire more generalized spatial geometries. We found out that the detection scheme developed in the previous part also works for generalized geometries. We discovered the strong effect of detection in certain directions. We still want to consider even more general position configurations not only for the atoms but also for the photo detectors.

# Bibliography

[1] A. Einstein, B. Podolsky, and N. Rosen, Phys. Rev. **47**, 777 (1935).

[2] E. Schrödinger, Math. Proc. Cambridge Philos. Soc. **31**, 555 (1935).

[3] E. Schrödinger, Math. Proc. Cambridge Philos. Soc. **32**, 446 (1936).

[4] J. S. Bell, Physics **1**, 195 (1964).

[5] S. J. Freedman and J. F. Clauser, Phys. Rev. Lett. **28**, 938 (1972).

[6] Z. Y. Ou and L. Mandel, Phys. Rev. Lett. **61**, 50 (1988).

[7] P. G. Kwiat, K. Mattle, H. Weinfurter, A. Zeilinger, A. V. Sergienko, and Y. Shih, Phys. Rev. Lett. **75**, 4337 (1995).

[8] M. A. Rowe, D. Kielpinski, V. Meyer, C. A. Sackett, W. M. Itano, C. Monroe, and D. J. Wineland, Nature **409**, 791 (2001).

[9] W. Tittel, J. Brendel, H. Zbinden, and N. Gisin, Phys. Rev. Lett. **81**, 3563 (1998).

[10] W. Tittel, J. Brendel, N. Gisin, and H. Zbinden, Phys. Rev. A **59**, 4150 (1999).

[11] A. Aspect, P. Grangier, and G. Roger, Phys. Rev. Lett. **49**, 91 (1982).

[12] A. Aspect, J. Dalibard, and G. Roger, Phys. Rev. Lett. **49**, 1804 (1982).

[13] C. H. Bennett, G. Brassard, C. Crépeau, R. Jozsa, A. Peres, and W. K. Wootters, Phys. Rev. Lett. **70**, 1895 (1993).

[14] D. Boschi, S. Branca, F. De Martini, L. Hardy, and S. Popescu, Phys. Rev. Lett. **80**, 1121 (1998).

[15] M. A. Nielsen and I. L. Chuang, *Quantum Computation and Quantum Information (Cambridge Series on Information and the Natural Sciences)*, 1 ed. (Cambridge University Press, Cambridge, 2004).

[16] A. K. Ekert, Phys. Rev. Lett. **67**, 661 (1991).

[17] N. Gisin, G. Ribordy, W. Tittel, and H. Zbinden, Rev. Mod. Phys. **74**, 145 (2002).

[18] A. Einstein and O. Stern, Ann. Phys. **345**, 551 (1913).

[19] G. S. Agarwal, *Quantum optics. Quantum statistical theories of spontaneous emission and their relation to other approaches* (Springer, Berlin, New York, 1974).

[20] Z. Ficek and S. Swain, *Quantum Interference and Coherence: Theory and Experiments* (Springer, New York, 2005), Vol. 100.

[21] E. V. Goldstein and P. Meystre, Phys. Rev. A **56**, 5135 (1997).

[22] J. I. Cirac and P. Zoller, Phys. Rev. A **50**, R2799 (1994).

[23] S. J. Phoenix and S. M. Barnett, J. Mod. Opt. **40**, 979 (1993).

[24] A. Beige, W. J. Munro, and P. L. Knight, Phys. Rev. A **62**, 052102 (2000).

[25] E. Hagley, X. Maître, G. Nogues, C. Wunderlich, M. Brune, J. M. Raimond, and S. Haroche, Phys. Rev. Lett. **79**, 1 (1997).

[26] P. R. Berman, *Cavity Quantum Electrodynamics (Advances in Atomic, Molecular and Optical Physics)* (Academic Press, New York, 1994).

[27] E. T. Jaynes and F. W. Cummings, Proc. IEEE **51**, 89 (1963).

[28] M. O. Scully and M. S. Zubairy, *Quantum Optics* (Cambridge University Press, Cambridge, 1997).

[29] C. C. Gerry and P. Knight, *Introductory Quantum Optics* (Cambridge University Press, Cambridge, 2005).

[30] G. Rempe, H. Walther, and N. Klein, Phys. Rev. Lett. **58**, 353 (1987).

[31] M. Brune, F. Schmidt-Kaler, A. Maali, J. Dreyer, E. Hagley, J. M. Raimond, and S. Haroche, Phys. Rev. Lett. **76**, 1800 (1996).

[32] I. Georgescu, Nat. Phys. **8**, 777 (2012).

[33] C. J. Hood, M. S. Chapman, T. W. Lynn, and H. J. Kimble, Phys. Rev. Lett. **80**, 4157 (1998).

[34] S. Haroche, M. Brune, and J. M. Raimond, Philos. Trans. **355**, pp. 2367 (1997).

[35] P. Meystre and M. Sargent III, *Elements of quantum optics*, 4 ed. (Springer, Berlin, Heidelberg, New York, 2007).

[36] D. Bouwmeester, J.-W. Pan, K. Mattle, M. Eibl, H. Weinfurter, and A. Zeilinger, Nature **390**, 575 (1997).

[37] S. Bose, Contemporary Physics **48**, 13 (2007).

[38] T. J. Osborne and M. A. Nielsen, Phys. Rev. A **66**, 032110 (2002).

[39] B.-Q. Jin and V. E. Korepin, Phys. Rev. A **69**, 062314 (2004).

[40] D. C. Burnham and D. L. Weinberg, Phys. Rev. Lett. **25**, 84 (1970).

[41] R. Rangarajan, M. Goggin, and P. Kwiat, Opt. Express **17**, 18920 (2009).

[42] M. Oberparleiter and H. Weinfurter, Opt. Commun. **183**, 133 (2000).

[43] J. C. Howell, R. S. Bennink, S. J. Bentley, and R. W. Boyd, Phys. Rev. Lett. **92**, 210403 (2004).

[44] I. Ali Khan and J. C. Howell, Phys. Rev. A **73**, 031801 (2006).

[45] A. N. Boto, P. Kok, D. S. Abrams, S. L. Braunstein, C. P. Williams, and J. P. Dowling, Phys. Rev. Lett. **85**, 2733 (2000).

[46] P. Kok, H. Lee, and J. P. Dowling, Phys. Rev. A **65**, 052104 (2002).

[47] G. J. Pryde and A. G. White, Phys. Rev. A **68**, 052315 (2003).

[48] C. K. Hong, Z. Y. Ou, and L. Mandel, Phys. Rev. Lett. **59**, 2044 (1987).

[49] A. J. Leggett, Prog. Theor. Phys. Suppl. **69**, 80 (1980).

[50] A. J. Leggett, J. Phys. Condens. Matter **14**, R415 (2002).

[51] J. J. Bollinger, W. M. Itano, D. J. Wineland, and D. J. Heinzen, Phys. Rev. A **54**, R4649 (1996).

[52] R. A. Campos, C. C. Gerry, and A. Benmoussa, Phys. Rev. A **68**, 023810 (2003).

[53] H. Cable, R. Vyas, S. Singh, and J. P. Dowling, New J. Phys. **11**, 113055 (2009).

[54] M. Tsang, Phys. Rev. Lett. **102**, 253601 (2009).

[55] G. Otfried and T. Géza, Phys. Rep. **474**, 1 (2009).

[56] W. K. Wootters, Phys. Rev. Lett. **80**, 2245 (1998).

[57] S. Hill and W. K. Wootters, Phys. Rev. Lett. **78**, 5022 (1997).

[58] S. P. Walborn, P. H. Souto Ribeiro, L. Davidovich, F. Mintert, and A. Buchleitner, Nature **440**, 1022 (2006).

[59] C. Schmid, N. Kiesel, W. Wieczorek, H. Weinfurter, F. Mintert, and A. Buchleitner, Phys. Rev. Lett. **101**, 260505 (2008).

[60] Q. Gulfam, Z. Ficek, and J. Evers, Phys. Rev. A **86**, 022325 (2012).

[61] H. Shin, K. W. C. Chan, H. J. Chang, and R. W. Boyd, Phys. Rev. Lett. **107**, 083603 (2011).

[62] M. Tsang, Phys. Rev. A **75**, 043813 (2007).

[63] S. Haroche, Phil. Trans. R. Soc. Lond. A **361**, 1339 (2003).

[64] D. Leibfried, E. Knill, S. Seidelin, J. Britton, R. B. Blakestad, J. Chiaverini, D. B. Hume, W. M. Itano, J. D. Jost, C. Langer, R. Ozeri, R. Reichle, and D. J. Wineland, Nature **438**, 639 (2005).

[65] M. Saffman, T. G. Walker, and K. Mølmer, Rev. Mod. Phys. **82**, 2313 (2010).

[66] I. Mourachko, D. Comparat, F. de Tomasi, A. Fioretti, P. Nosbaum, V. M. Akulin, and P. Pillet, Phys. Rev. Lett. **80**, 253 (1998).

[67] M. D. Lukin, M. Fleischhauer, R. Cote, L. M. Duan, D. Jaksch, J. I. Cirac, and P. Zoller, Phys. Rev. Lett. **87**, 037901 (2001).

[68] D. Comparat and P. Pillet, J. Opt. Soc. Am. B **27**, A208 (2010).

[69] L. Jin, M. Macovei and J. Evers, arXiv:1202.0699.

[70] M. A. Nielsen and I. L. Chuang, *Quantum Computation and Quantum Information* (Cambridge University Press, Cambridge, 2000).

[71] Z. Ficek, Front. Phys. China **5**, 26 (2010).

[72] C. Marr, A. Beige, and G. Rempe, Phys. Rev. A **68**, 033817 (2003).

[73] C. Xun-Ming, G. Guo-Qin, Y. Miao, and H. Qing, Communs. Theo. Phys. **49**, 1017 (2008).

[74] S. Haroche and J. M. Raimond, Sci. Am. **268**, 54 (1993).

[75] Y. H. Shih, A. V. Sergienko, M. H. Rubin, T. E. Kiess, and C. O. Alley, Phys. Rev. A **50**, 23 (1994).

[76] G. Di Giuseppe, M. Atatüre, M. D. Shaw, A. V. Sergienko, B. E. A. Saleh, and M. C. Teich, Phys. Rev. A **66**, 013801 (2002).

[77] K. Edamatsu, G. Oohata, R. Shimizu, and T. Itoh, Nature **431**, 167 (2004).

[78] Z. Yang and J. E. Sipe, Opt. Lett. **32**, 3296 (2007).

[79] W. Ueno, F. Kaneda, H. Suzuki, S. Nagano, A. Syouji, R. Shimizu, K. Suizu, and K. Edamatsu, Opt. Express **20**, 5508 (2012).

[80] M. Barbieri, F. De Martini, G. Di Nepi, P. Mataloni, G. M. D'Ariano, and C. Macchiavello, Phys. Rev. Lett. **91**, 227901 (2003).

[81] J. M. Raimond, M. Brune, and S. Haroche, Rev. Mod. Phys. **73**, 565 (2001).

[82] S. Olmschenk, D. N. Matsukevich, P. Maunz, D. Hayes, L.-M. Duan, and C. Monroe, Science **323**, 486 (2009).

[83] M. Feng and X. Wang, J. Opt. B: Quantum and Semiclassical Opt. **4**, 283 (2002).

[84] T. Yu and J. H. Eberly, Science **323**, 598 (2009).

[85] K. Ann and G. Jaeger, Found. Phys. **39**, 790 (2009).

[86] K. Życzkowski, P. Horodecki, M. Horodecki, and R. Horodecki, Phys. Rev. A **65**, 012101 (2001).

[87] P. J. Dodd and J. J. Halliwell, Phys. Rev. A **69**, 052105 (2004).

[88] T. Yu and J. H. Eberly, Phys. Rev. Lett. **93**, 140404 (2004).

[89] M. P. Almeida, F. de Melo, M. Hor-Meyll, A. Salles, S. P. Walborn, P. H. S. Ribeiro, and L. Davidovich, Science **316**, 579 (2007).

[90] A. Salles, F. de Melo, M. P. Almeida, M. Hor-Meyll, S. P. Walborn, P. H. Souto Ribeiro, and L. Davidovich, Phys. Rev. A **78**, 022322 (2008).

[91] J. Laurat, K. S. Choi, H. Deng, C. W. Chou, and H. J. Kimble, Phys. Rev. Lett. **99**, 180504 (2007).

[92] Z. Ficek and R. Tanaś, J. Mod. Opt. **50**, 2765 (2003).

[93] Z. Ficek and R. Tanaś, Phys. Rev. A **74**, 024304 (2006).

[94] Z. Ficek and R. Tanaś, Phys. Rev. A **77**, 054301 (2008).

[95] C. E. López, G. Romero, F. Lastra, E. Solano, and J. C. Retamal, Phys. Rev. Lett. **101**, 080503 (2008).

[96] L. Mazzola, S. Maniscalco, J. Piilo, K.-A. Suominen, and B. M. Garraway, Phys. Rev. A **79**, 042302 (2009).

[97] B.-G. Englert, M. Loffler, O. Benson, B. Varcoe, M. Weidinger, and H. Walther, Fortschr. Phys. **46**, 897 (1998).

[98] S. Ritter, C. Nölleke, C. Hahn, A. Reiserer, A. Neuzner, M. Uphoff, M. Mücke, E. Figueroa, J. Bochmann, and G. Rempe, Nature (London) **484**, 195 (202).

[99] M. Ikram, F.-l. Li, and M. S. Zubairy, Phys. Rev. A **75**, 062336 (2007).

[100] B. Bellomo, R. Lo Franco, and G. Compagno, Phys. Rev. Lett. **99**, 160502 (2007).

[101] B. Bellomo, R. Lo Franco, and G. Compagno, Phys. Rev. A **77**, 032342 (2008).

[102] B. Bellomo, R. L. Franco, S. Maniscalco, and G. Compagno, Phys. Scr. **T140**, 014014 (2010).

[103] M. Yönaç, T. Yu, and J. H. Eberly, J. Phys. B **40**, S45 (2007).

[104] F. F. Fanchini, T. Werlang, C. A. Brasil, L. G. E. Arruda, and A. O. Caldeira, Phys. Rev. A **81**, 052107 (2010).

[105] A. G. Dijkstra and Y. Tanimura, Phys. Rev. Lett. **104**, 250401 (2010).

[106] P. W. Milonni and P. L. Knight, Phys. Rev. A **10**, 1096 (1974).

[107] F. T. Arecchi and E. Courtens, Phys. Rev. A **2**, 1730 (1970).

[108] H. Gießen, J. D. Berger, G. Mohs, P. Meystre, and S. F. Yelin, Phys. Rev. A **53**, 2816 (1996).

[109] W. Shu and T. Yu, J. Phys. B **44**, 225501 (2011).

[110] C. Anastopoulos, S. Shresta, and B. L. Hu, Quant. Info. Proc. **8**, 549 (2009).

[111] C. Anastopoulos, S. Shresta and B. L. Hu, arXiv:quant-ph/0610007.

[112] C. H. Fleming, N. I. Cummings, C. Anastopoulos, and B. L. Hu, J. Phys. A **45**, 065301 (2012).

[113] S. Maniscalco, F. Francica, R. L. Zaffino, N. Lo Gullo, and F. Plastina, Phys. Rev. Lett. **100**, 090503 (2008).

[114] M. Khudaverdyan, W. Alt, T. Kampschulte, S. Reick, A. Thobe, A. Widera, and D. Meschede, Phys. Rev. Lett. **103**, 123006 (2009).

[115] J. Eschner, C. Raab, A. Mundt, A. Kreuter, C. Becher, F. Schmidt-Kaler, and R. Blatt, Fortschr. Phys. **51**, 359 (2003).

[116] M. Yönaç, T. Yu, and J. H. Eberly, J. Phys. B **39**, S621 (2006).

[117] M. Yönaç, T. Yu, and J. H. Eberly, J. Phys. B **40**, S45 (2007).

[118] E. J. Post, Rev. Mod. Phys. **39**, 475 (1967).

[119] L. Rayleigh, Phil. Mag. **8**, 261 (1879).

[120] E. Abbe, Arch. Mikrosk. Anat **9**, 413 (1873).

[121] P. R. Hemmer, A. Muthukrishnan, M. O. Scully, and M. S. Zubairy, Phys. Rev. Lett. **96**, 163603 (2006).

[122] Q. Sun, P. R. Hemmer, and M. S. Zubairy, Phys. Rev. A **75**, 065803 (2007).

[123] S. J. Bentley and R. W. Boyd, Opt. Express **12**, 5735 (2004).

[124] R. W. Boyd and S. J. Bentley, J. Mod. Opt. **53**, 1529 (2006).

[125] E. Yablonovitch and R. B. Vrijin, Opt. Eng. **38**, 334 (1999).

[126] G. Björk, L. L. Sánchez-Soto, and J. Söderholm, Phys. Rev. Lett. **86**, 4516 (2001).

[127] M. D' Angelo, M. V. Chekova, and Y. Shih, Phys. Rev. Lett. **87**, 013602 (2001).

[128] V. Giovannetti, S. Lloyd, and L. Maccone, Phys. Rev. Lett. **96**, 010401 (2006).

[129] C. M. Caves, Phys. Rev. D **23**, 1693 (1981).

[130] B. Yurke, S. L. McCall, and J. R. Klauder, Phys. Rev. A **33**, 4033 (1986).

[131] V. Giovannetti, S. Lloyd, and L. Maccone, Science **306**, 1330 (2004).

[132] W. N. Plick, C. F. Wildfeuer, P. M. Anisimov, and J. P. Dowling, Phys. Rev. A **80**, 063825 (2009).

[133] M. Kiffner, J. Evers, and M. S. Zubairy, Phys. Rev. Lett. **100**, 073602 (2008).

[134] Z. Liao, M. Al-Amri, and M. S. Zubairy, Phys. Rev. Lett. **105**, 183601 (2010).

[135] H. Shin, K. W. C. Chan, H. J. Chang, and R. W. Boyd, in *Frontiers in Optics* (Opt. Soc. Am., ADDRESS, 2010), p. FMM2.

[136] Y. Kawabe, H. Fujiwara, R. Okamoto, K. Sasaki, and S. Takeuchi, Opt. Express **15**, 14244 (2007).

[137] T. Nagata, R. Okamoto, J. L. O'Brien, K. Sasaki, and S. Takeuchi, Science **316**, 726 (2007).

[138] M. W. Mitchell, J. S. Lundeen, and A. M. Steinberg, Nature (London) **429**, 161 (2004).

[139] M. Keller, B. Lange, K. Hayasaka, W. Lange, and H. Walther, Nature (London) **431**, 1075 (2004).

[140] I. Afek, O. Amber, and Y. Silberberg, Science **328**, 879 (2010).

[141] I. Afek, O. Amber, and Y. Silberberg, Phys. Rev. Lett **105**, 093603 (2010).

[142] C.-Y. Lu *et al.*, Nature **3**, 91 (2007).

[143] A. Auffeves, P. Maioli, T. Meunier, S. Gleyzes, G. Nogues, M. Brune, J. M. Raimond, and S. Haroche, Phys. Rev. Lett. **91**, 230405 (2003).

[144] C.-Y. Chen, S.-H. Li, and M. Feng, J. Phys. B **40**, 2961 (2007).

[145] V. V. Dodonov, I. A. Malkin, and V. I. Man'ko, Physica **72**, 597 (1974).

[146] R. J. Glauber, Phys. Rev. Lett. **10**, 84 (1963).

[147] R. J. Glauber, Phys. Rev. **130**, 2529 (1963).

[148] R. J. Glauber, Phys. Rev. **131**, 2766 (1963).

[149] C. C. Gerry, Phys. Rev. A **59**, 4095 (1999).

[150] A. Ourjoumtsev, R. Tualle-Brouri, J. Laurat, and P. Grangier, Science **312**, 83 (2006).

[151] J. S. Neergaard-Nielsen, B. M. Nielsen, C. Hettich, K. Mølmer, and E. S. Polzik, Phys. Rev. Lett. **97**, 083604 (2006).

[152] K. Wakui, H. Takahashi, A. Furusawa, and M. Sasaki, Opt. Express **15**, 3568 (2007).

[153] W. P. Schleich, *Quantum Optics in Phase Space* (WILEY-VCH, Berlin, 2001).

[154] H. Schempp, G. Günter, C. S. Hofmann, C. Giese, S. D. Saliba, B. D. DePaola, T. Amthor, M. Weidemüller, S. Sevinçli, and T. Pohl, Phys. Rev. Lett. **104**, 173602 (2010).

[155] G. Günter, M. Robert-de-Saint-Vincent, H. Schempp, C. S. Hofmann, S. Whitlock, M. Weidemüller, arXiv:1106.5443.

[156] J. D. Pritchard, D. Maxwell, A. Gauguet, K. J. Weatherill, M. P. A. Jones, and C. S. Adams, Phys. Rev. Lett. **105**, 193603 (2010).

[157] G. S. Agarwal, *Quantum Optics*, *Springer Tracts in modern physics* (Springer-Verlag, Berlin, 1974).

[158] M. Kiffner, M. Macovei, J. Evers, and C. H. Keitel, in *Progress in Optics*, edited by E. Wolf (Elsevier, Amsterdam, 2010), Vol. 55.

[159] R. J. Glauber, Phys. Rev. **130**, 2529 (1963).

[160] S. E. Harris and Y. Yamamoto, Phys. Rev. Lett. **81**, 3611 (1998).

[161] M. Saffman, T. G. Walker, and K. Mølmer, Rev. Mod. Phys. **82**, 2313 (2010).

[162] H. J. Metcalf and P. van der Straten, *Laser Cooling and Trapping* (Springer-Verlag, New York, 1999).

[163] C. N. Cohen Tannoudji and W. D. Phillips, Phys. Today **43**, 33 (1990).

[164] G. S. Agarwal and A. K. Patnaik, Phys. Rev. A **63**, 043805 (2001).

[165] M. Kiffner, J. Evers, and C. H. Keitel, Phys. Rev. A **76**, 013807 (2007).

[166] Q. Gulfam and J. Evers, J. Phys. B **43**, 045501 (2010).

[167] T. J. Carroll, K. Claringbould, A. Goodsell, M. J. Lim, and M. W. Noel, Phys. Rev. Lett. **93**, 153001 (2004).

# Acknowledgments

I sincerely thank

- Allah Almighty who enabled me to carry out this research work
- the spokesperson of International Max Planck Research School, Hon. Prof. Dr. C. H. Keitel for the support, for the DPG meetings every year and for the HGSFP graduate days every semester during the time of the Ph. D.
- PD Dr. J. Evers, who had been a source of guidence and useful advice during these years. I acknowledge his highly professional attitude, the fruitful discussions, the enthusiasm and passion with which he supervised me and the ever-readiness to offer help regarding physics despite his busy schedule
- my co-supervisors, Dr. S. Wimberger and Dr. T. Pfeifer
- other members of my thesis committee: Prof. Dr. T. Gasenzer, Prof. Dr. S. Joachim and Prof. Dr. K. Pfeilsticker
- the proof readers of the introductory part of the thesis, Sebastian, Martin and Kilian
- Sven and Sebastian, who helped translating the abstract to German
- my former and current office mates, Huayu, Atif, Oleg, Stefano, Nikolay, Sebastian, Norman,. . .
- former and current computer administrators: Peter, Dominik and Carsten
- former and present secretaries Brigitte, Sibel and Ludmila
- Higher Education Commission of Pakistan for the financial support during Ph. D., Heidelberg Graduate School For Fundamental Physics for the partial financial support during the last 14 months of the doctoral studies, Deutscher Akademischer Austauschdienst for administrative matters
- my helpful Pakistani friends in Germany and my dear German neighbors
- my parents and siblings for all their love and effort and also my family-in-law
- Gulfam, my everything, who stayed with me all the time and continues to make me feel like the happiest person on Earth. Words are just not enough to thank him. Ahmed and Fatemah, our beloved children, who fill our lives with their ever-new innocent affection.